Department of Precision and Microsystems Engineering

Design of 3 DoF and 6 DoF Force and Moment Balanced Manipulators Based on the Spatial Pantograph Linkage

Luuk Withagen

Report no : 2023.012
Coach : Dr.ir. V. van der Wijk
Professor : Prof.dr.ir. J.L. Herder
Specialisation : Engineering Dynamics
Type of report : Master Thesis
Date : 24 February 2023

Design of 3 DoF and 6 DoF Force and Moment Balanced Manipulators Based on the Spatial Pantograph Linkage

By

L.W.J. Withagen

in partial fulfilment of the requirements for the degree of

Master of Science
in Mechanical Engineering

at the Delft University of Technology,
to be defended publicly on Friday February 24, 2023 at 09.30 AM

Supervisor	Dr.ir. V. van der Wijk	PME, TU Delft
Thesis committee:	Prof.dr.ir. J.L. Herder	PME, TU Delft
	Dr. J.K. Moore	BMechE, TU Delft

Preface

This thesis represents a one-and-a-half-year-long journey of great challenges, which began with finding an appropriate research topic. In my ambition of working on a purely mechanical subject in which I could work a lot with dynamics, I did not find my research topic in the approximately 100 project proposals during the thesis market. After contacting the study advisor and a couple of researchers with interesting research directions, I came in touch with Volkert van der Wijk. In a short online meeting, he suggested me to work on dynamically balanced mechanisms to be used in aerial manipulation, which immediately took my interest.

After finishing my literature research, the aerial manipulation part of the topic went away slowly, and I started focussing solely on spatially dynamically balanced linkages, as this was already a great challenge. I tried calculating balance conditions for different concepts I had in mind, but unfortunately, without any success. Then Volkert showed me his, at that time not yet published, force balanced spatial pantograph linkage. I tried a couple of things with this linkage until I came up with the idea of constraining the linkage and using it as legs for a parallel robot, which ended up being the content of this thesis.

I would like to thank everyone who helped me with the research that led to this thesis. In particular, I would like to thank Lucas Giesen, Lars Hoogland, and Matto Leeuwis for proofreading this thesis, Joris Kuiper for helping me solve many small problems by taking the time to have small discussions, and Paula Goldebeld for taking pictures of the demonstrator.

I would also like to express my gratitude to my supervisor Volkert van der Wijk. Through our fruitful discussions, and his thorough understanding of mechanical engineering, he was able to bring my research to a much higher level.

Lastly, I would like to thank my family and friends for supporting me throughout my research and for providing a great amount (sometimes maybe too much) of distraction from my thesis.

Luuk Withagen
Delft, February 2023

Contents

Chapter 1

Introduction

Introduction

When robots move, they generally induce reaction forces and reaction moments on their base, which are generated by the inertia of the accelerating moving links. As the dynamic unbalance is induced by the acceleration of bodies, these reaction forces and moments become even more considerable when robots move at high speeds [1]. The dynamic unbalance could lead to numerous unwanted effects such as vibrations, noise, wear, and fatigue problems, which all limit the full potential of the robotic arm [1]. When the robot is attached to an unstable base, for example an aerial vehicle, dynamic unbalance could also lead to imprecision due to movements of the base [2].

There are numerous applications in which dynamic unbalance could be of great concern, for which multiple suitable solutions exist. For example, problems occur in large robotic arms. Due to its size and weight, the reaction forces and moments become very large. In order to prevent the base of the robot from moving due to this unbalance, a large concrete slab is built into the workspace floor [3]. Another method to reduce the influence of vibrations caused by dynamic unbalance is to program rest in the motion of manipulators to wait until vibrations have died out [4]. Other kinds of solutions focus on removing dynamic unbalance through the design of manipulators, called *dynamically balanced* manipulators.

Dynamic balance could be categorized into two parts: *force balance* and *moment balance*. A mechanism is said to be *force balanced* when it does not induce any resultant reaction forces on its base during motion. Similarly, a mechanism is said to be *moment balanced* when it does not induce any resultant reaction moments on its base during motion. When a linkage is both force and moment balanced, it is said to be *dynamically balanced*.

Dynamically balanced mechanisms could solve problems in different sectors. In the example of large robotic arms, dynamic balance could reduce the size of the reaction forces and moments on the base, and thereby the amount of reinforced concrete needed to keep the robot in place.

Dynamically balanced mechanisms could especially be of great interest for robots that are attached to an unstable base, for example a floating base such as in aerial manipulation. Due to the instability of the floating base of the aerial vehicle, any motion of an unbalanced arm attached to it leads to perturbations in the position of the base. Due to these induced perturbations, it is even harder to reach the desired end-effector position in aerial manipulation.

Another case in which manipulators are attached to an unstable base is in stage lighting. In theatres, moving lights are often hung on lightweight structures hanging from the roof by chains. When these lights move, they generate enough momentum to swing the entire structure from which it is hanging. This leads to a loss in precision of the lighted spot. Some solutions exist to balance these reaction forces and moments actively using driven counter-rotations and moving masses like [5] and [6]. An interesting aspect of these solutions is that not all degrees of freedom are balanced, but only the most important ones. Similar systems exist for cameras hanging from cables [7].

Although all examples above are spatial robots, the dynamic balance of multi-degree-of-freedom linkages that move spatially was only touched upon slightly [8]. To the best of the author's knowledge, only three examples exist for dynamically balanced spatial manipulators. These are the parallelepiped [9] (Figure 1.1a), the compound four-bar [10] (Figure 1.1b), and the PAMINSA [11] (Figure 1.1c) manipulators. Regarding force balanced linkages, the spatial pantograph linkage [12] (Figure 1.2) is promising, as its 6 DoF can be balanced using only 2 counter masses.

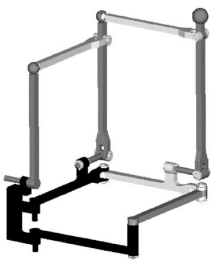

(a) 3 DoF Parallelepiped [9]

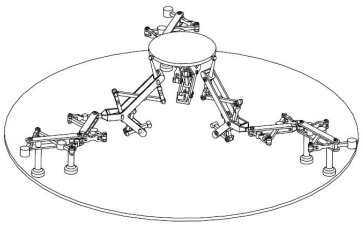

(b) 6 DoF compound four-bar [10]

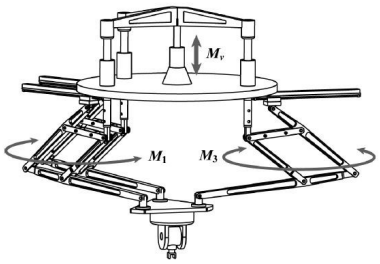

(c) 6 DoF PAMINSA [11]

Figure 1.1: Dynamically balanced linkages with a spatial workspace

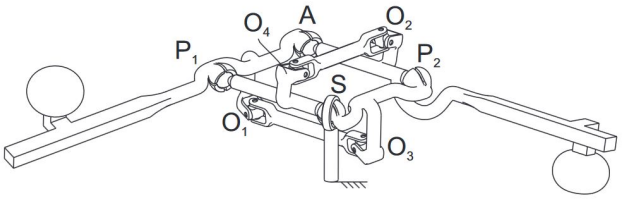

Figure 1.2: General spatial pantograph linkage [12]

Research goals

The focus of this thesis is on force and moment balanced manipulators with a spatial workspace. This is done using the following two research goals:

1. Present the state-of-the-art regarding spatial dynamically balanced manipulators and compare them for their use in aerial manipulation
2. Present novel designs of 3 DoF and 6 DoF manipulators based on the spatial pantograph linkage that use fewer counter masses and moving links

Thesis Outline

This thesis will start with a literature survey into the existing dynamically balanced 6 DoF spatial manipulators in chapter 2. In this paper, the requirements for aerial manipulators are set, and the existing manipulators are evaluated with regards to these requirements. Additionally, the methods by which the dynamic balance of the mechanisms is obtained are discussed.

In chapter 3 the designs of novel 3 DoF and 6 DoF force and moment balanced manipulators based on the spatial pantograph linkage [12] are shown. The workspace, inverse kinematics, and balance conditions are determined for the 3 DoF design. This knowledge is then used to synthesize a 6 DoF dynamically balanced parallel manipulator which could be balanced by only 9 counter-masses and 9 counter-rotations. A reduction of this manipulator, which is force balanced using only 6 counter masses, is also shown.

The results obtained in chapter 2 and 3 are discussed in chapter 4. Finally, the conclusions of this thesis are presented in chapter 5. At the end of this thesis, appendices could be found which show in-depth knowledge that could be useful in the design of dynamically balanced manipulators.

Chapter 2

Comparison of various dynamically balanced spatial mechanisms for their use in aerial manipulation

Comparison of various dynamically balanced spatial mechanisms for their use in aerial manipulation

Luuk Withagen
High-Tech Engineering
Delft University of Technology
Delft, the Netherlands
L.W.J.Withagen@student.tudelft.nl

***Abstract*—This literature survey aims to answer the research question *"Which reactionless spatial mechanisms exist and how do they compare for aerial manipulation?"*. Design constraints are set for aerial manipulators, out of which the mass of the manipulator is the main issue. The only three dynamically balanced spatial mechanisms that can be found in literature are presented and compared with regard to the design constraints that were set. This shows a huge potential for partially decoupling the kinematics of mechanisms which substantially simplifies the dynamics, possibly leading to less complex balanced architectures.**

***Index Terms*—dynamic balancing, spatial mechanism, aerial manipulation**

I. Introduction

The interest in aerial manipulation using unmanned aerial vehicles (UAVs) is growing very fast [1]. This is motivated by their possibility of performing certain tasks in hard-to-reach places like bridges, wind turbines, and many more [2]. When using a robotic arm on an UAV, reaction forces and moments are generated by the motion of the arm, which causes perturbations in the position and motion of the UAV [2]. These reaction forces and moments are called *shaking forces* and *shaking moments* respectively. These forces are especially considerable if mechanisms move at high speeds [3]. Next to perturbations in position, these forces also cause vibrations, noise, wear, and fatigue problems which limits the full potential of the robotic arm [3]. However, because of the unstable base of UAVs [4] perturbations in the position and motion are of most interest for aerial manipulation.

To solve these problems, dynamically balanced (reactionless) mechanisms were introduced. These are mechanisms in which inertial and geometric parameters are carefully chosen such that the total system does not induce any shaking forces and shaking moments on its base. For industrial applications involving high-speed manipulations, balanced manipulators would significantly improve the general performance and accuracy of the machine [5]. To the best of the author's knowledge, the only research that was performed on using dynamically balanced manipulators on UAVs was by Beacom in 2021 on a 2 DoF manipulator.

A major drawback of dynamically balanced mechanisms is that the balancing often leads to a large increase in mass [7] which increases the actuator torque [8] which induces the need for larger and thereby heavier actuators, increasing the mass even more. Additionally, a higher mass makes the manipulators less usable for aerial manipulators due to the payload limitation they impose [2].

A large amount of research on dynamic balancing has focussed on the synthesis and design of planar reactionless mechanisms, but the dynamic balancing of multi-degree-of-freedom mechanisms that move spatially was only touched upon slightly [5]. However, due to their instability, unmanned aerial vehicles (UAVs) show small oscillations in all degrees of freedom (DoFs) [9]. This suggests the need for spatial mechanisms for aerial manipulation to be able to compensate for these oscillations.

This leads to the research question for this literature survey: "*Which reactionless spatial mechanisms exist and how do they compare for aerial manipulation?*". In answering this question, only completely balanced mechanisms will be investigated. Although 6 DoF would be needed to compensate for all disturbances [9], there will be no strict requirement for the number of DoFs in order to include a larger number of dynamically balanced spatial mechanisms in this literature review.

This literature review will present a systematic comparison of different existing spatial reactionless mechanisms with a focus on their potential use in UAVs. First, the implied definition of UAVs will be established and it will be stated to which design constraints an aerial manipulator has to comply to. Then, some fundamental knowledge is provided about the balancing principles for spatial mechanisms. Afterwards, the three examples of spatial reactionless mechanisms that can be found in literature are presented. Finally, the examples will be compared regarding their potential use in aerial manipulation from which some conclusions are drawn.

II. Unmanned aerial manipulators

In order to perform manipulations using an UAV, a proper tool should be attached to it. Existing solutions can be roughly split up into two categories. The first option is to attach a gripper directly to a UAV, which is called a *flying hand* in literature [1]. Another option is to not directly attach the gripper to the UAV, but by means of a robotic arm instead. This type is called an *unmanned aerial manipulator* (UAM). An UAM mainly consists of the following elements [1]:

1) The floating base of the unmanned aerial vehicle (UAV);

2) The robotic arm;
3) A gripper or a multi-fingered hand attached as the end-effector of the arm;
4) Sensors such as cameras or laser scanners

This literature review will solely focus on the robotic arm of the UAM.

A. Design constraints

In order to compare mechanisms from literature for their use in aerial manipulation, the design constraints have to be specified. According to Danko et al. (2015), the manipulation task in unmanned aerial manipulators (UAVs) leads to the following design constraints for the manipulator:

1) It must be able to compensate for the imprecision of the UAV;
2) It must be dynamically faster than the UAV;
3) It must not interfere with the UAV during take-off, landing, or flight.

The first two constraints concern the compensation of the UAVs imprecision caused by perturbations from for example air currents. Constraint 1 states that the workspace of the manipulator should be large enough to compensate for the perturbations in the UAV. Because UAVs show perturbations in all DoFs [9], the manipulator's workspace should also be spatial in to compensate for all perturbations. It is insufficient to have a large enough workspace to compensate for the perturbations. The manipulator should also be able to compensate for these perturbations in the correct timescale. Therefore, the manipulator should be faster than the perturbations as stated in constraint 2.

The last constraint is of most interest for this literature review. Besides introducing a size limitation of the manipulator, it imposes that the manipulator should not deliver any reaction forces to the UAV during operation. This enhances the need for dynamically balanced manipulators. This constraint also implies that the mass of the manipulator should be minimal, due to the payload limitation of UAVs [2].

III. Fundamentals

In order have proper understanding of dynamic balancing, the fundamentals will be explained in this section. Firstly, some important definitions are explained and afterwards the relevant balancing principles for spatial mechanisms are briefly explained.

A mechanism is *statically balanced* if it has a constant potential energy for the complete range of motion. This means that no energy has to be delivered to the system to maintain its position.

When a mechanism delivers no reaction forces to its base during motion, it is said to be *force balanced*. Just like statically balanced mechanisms, the potential energy of the mechanism is constant. However, with force balance, it is not possible to store energy in springs as this would not prevent inertial forces from acting on the base of the mechanism.

The last type of balance is *moment balance*, which states that a mechanism does not deliver any reaction moments to the base of the mechanism.

When a mechanism does not deliver any reaction forces or moments to its base while in motion, it is said to be *dynamically balanced* or *reactionless*. This occurs if both the conditions for the force and moment balance are met.

The conditions for dynamic balance could be calculated in numerous ways. Each method will work, but some methods will be more efficient for certain mechanisms, therefore authors use different approaches. The methods used in the calculations for the mechanisms that will be discussed in this literature survey will be briefly presented below.

A. Conservation of momentum

A straightforward method for computing the dynamic balance conditions is by the conservation of linear and angular momentum. The linear momentum of a mechanism is defined by the product of the mass and the velocity of the CoM (1). Its derivative equals the reaction force on the CoM due to the change in velocity of this CoM (2), which should be zero. This implies that the CoM should have a constant velocity or should be stationary in order to have zero reaction forces on its base (force balanced). Although there are no reaction forces on the base, there could be constant forces like gravity acting on the base.

$$\mathbf{p} = m\mathbf{v} \tag{1}$$

$$\mathbf{F} = \dot{\mathbf{p}} = \frac{d}{dt}(m\mathbf{v}) = \mathbf{0} \tag{2}$$

For dynamic balance, the reaction moments on the base should also be zero. These moments are equal to the time derivative of the angular momentum as in (3). In order to have a moment balanced mechanism, the angular momentum should also be zero or constant.

$$\mathbf{M} = \dot{\mathbf{H}} = \mathbf{0} \tag{3}$$

Only these equations (2, 3) have to be satisfied in order to obtain a dynamically balanced mechanism [11].

B. Constant inertia tensor

Another method for obtaining dynamic balance conditions for a mechanism is by observing that a balanced mechanism globally behaves as a rigid body [12]: it has a constant CoM, and it produces no shaking forces and shaking moments to its base. When this condition is met a mechanism is said to be *dynamically decoupled* e.g. motion of the mechanism does not cause any reaction forces and moments on the base, and forces and moments on the base of the mechanism also do not induce any internal motion of the mechanism. A couple of steps should be taken to calculate the balance conditions using this method.

Firstly, the moment of inertia of each link should be calculated around its CoM. Then the generalized parallel axis

theorem [13] can be used to find the moment of inertia of each link around the base. This generalization can be seen in (4) in which $\mathbf{I}$ and $\mathbf{I}'$ are the moment of inertia around the CoM of the link and the base respectively. R represents the vector from the CoM of the link to the base of the mechanism.

$$I'_{ij} = I_{ij} + m(|\mathbf{R}|^2\delta_{ij} - R_i R_j) \tag{4}$$

With these moments of inertia of the links around the base and the rotation matrices of these links with respect to the inertial frame, the total inertia tensor of the mechanism can be calculated as in (5). In this tensor, the diagonal terms are the *moments of inertia*, and the off-diagonal terms are the *products of inertia*.

$$\mathbf{I} = \sum_{i=1}^{n} \mathbf{Q}_i I_{bi} \mathbf{Q}_i^T = \begin{bmatrix} I_{xx} & -I_{xy} & -I_{xz} \\ -I_{xy} & I_{yy} & -I_{zz} \\ -I_{xz} & -I_{yz} & I_{zz} \end{bmatrix} \tag{5}$$

For a rigid body, the products of inertia around its CoM are always zero, and the moments of inertia are invariant of time. So, the conditions for a mechanism to be dynamically decoupled, and thereby dynamically balanced, are that its products of inertia are zero and its moments of inertia are invariant of time and the configuration of the mechanism.

IV. Dynamically balanced spatial mechanisms

A. Parallelepiped mechanism

The first dynamically balanced spatial mechanism that will be discussed is the parallelepiped mechanism presented in [14]. A screenshot of the CAD model of a leg of this mechanism can be seen in Fig. 1.

The synthesis of this mechanism started off with balancing a planar five-bar linkage with a parallelogram architecture. This architecture could be balanced with only three counterweights and two counter-rotations [14]. Then this structure was expanded with another segment out of the plane of the planar five-bar architecture to obtain a parallelepiped mechanism. This mechanism needs six counter masses and three counter-rotations for dynamic balance.

The balance conditions for this mechanism were derived *conservation of momentum* method as described in Section III-A.

In order to keep the necessary links parallel to have a parallelepiped, a proper choice of joints is needed. Many configurations are possible, but only two cases are investigated in [14]. From this, it was observed that the balancing conditions are identical for both configurations. Thereby, this paper confirms that dynamic balancing conditions are only dependent on geometric and inertial parameters and not on the joints that determine the motion of the mechanism.

By using three of the mechanisms from Fig. 1 as legs of a parallel manipulator, a 6 DoF dynamically balanced spatial mechanism can be synthesized. However, as often in balancing, this comes at the price of a large increase in the mass and inertia of the mechanism.

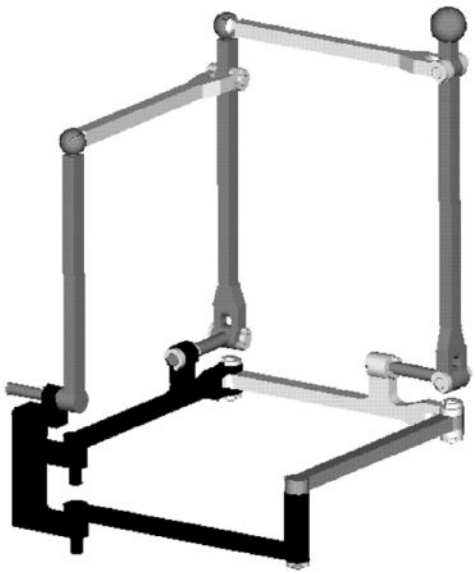

Fig. 1: CAD model of a spatial reactionless 3-DoF mechanism based on a parallelepiped [14]

The parallelepiped in Fig. 1 has 3 translational DoF. In the practical example from [14], balancing of this mechanism resulted in an increase of mass of about 12.5 times compared to the unbalanced mechanism. However, the increase of the mass depends heavily on the length of the counter mass arms. The shorter the lengths of these arms, the greater the mass increase of the system. Due to the use of active counter-rotations, additional actuators are required, which will also increase the mass of the manipulator.

B. Combination of four-bar linkages

The parallelepiped mechanism uses counter-rotations in order to moment balance the spatial mechanism. For such linkages, complex mechanical transmissions or additional actuators are needed for this design to work. To overcome this, Wu and Gosselin (2004) have come up with a spatially balanced mechanism that does not involve any counter-rotations.

The concept for this reactionless mechanism was initially based on the research of Ricard and Gosselin (2000), in which balancing conditions were developed for different kinds of four-bar mechanisms. These balancing conditions were then calculated again, but now with the *constant inertia tensor method* from section III-B. It was found that the moment of inertia I_{zz} could be constant under the balancing conditions, but I_{xx} and I_{yy} could not. However, it was observed that the sum of these moments of inertia could be constant, which led to the idea of a composite mechanism from Fig. 2.

For this composite mechanism, the authors found conditions for which the inertia matrix of the total mechanism was independent of the input angles. This resulted in a dynamically decoupled building block for multi-DoF manipulators.

With this knowledge, a spatial 3 DoF mechanism was synthesized. The first two DoFs were generated by attaching

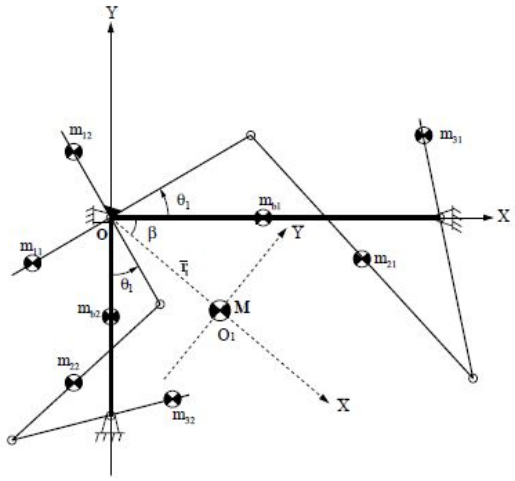

Fig. 2: Composite mechanism with a constant inertia tensor [12]

two single four-bars to each other in the same plane. This could be done because their moment of inertia I_{zz} is constant, and therefore it behaves as a rigid body for in-plane motion. Then a composite mechanism as in Fig. 2, which is balanced for spatial motion, was attached to these single four-bars. This stacked mechanism (the leg from Fig. 3) has 3 DoF that are not in the same plane, and therefore it is a spatial mechanism.

In order to synthesize a 6 DoF dynamically balanced spatial mechanism, three stacked mechanisms as described above, are used as legs in a parallel manipulator. A CAD drawing of the synthesized mechanism can be seen in Fig. 3.

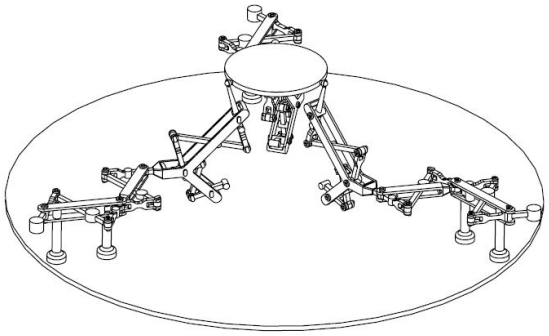

Fig. 3: CAD model of a reactionless spatial 6-DoF mechanism based on a combination of four-bar linkages [12]

C. PAMINSA manipulator

In [15] a new family of partially kinematically decoupled parallel manipulators was introduced, called PAMINSA. In this research, it was tried to develop a fully decoupled parallel manipulator. However, it was found that it was not possible to develop a fully decoupled manipulator that retains the property of parallel manipulators to be stiff while having a low mass [15]. Therefore, the proposed manipulator is only partially decoupled.

It was chosen to decouple the vertical movement of the manipulator from the other DoFs. This came from the notion that the work of gravity is zero for horizontal motion, but is non-zero for vertical motion [16]. Because not all the directions are subjected to an equal amount of gravitational work, less powerful actuators can be used for horizontal movements and thereby reducing the total mass of the mechanism.

In order to decouple both motions, pantograph linkages as shown in Fig. 4 were used. In this linkage, point B_i is positioned vertically for the vertical motion of point C_i, and point A_i is positioned horizontally for the horizontal motion of point C_i. Then, three such legs were combined and attached to a platform to obtain a 3 DoF spatial mechanism in which the vertical motion is decoupled from the horizontal motion.

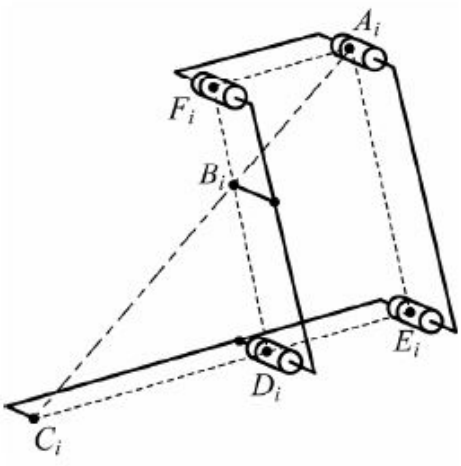

Fig. 4: Pantograph linkage [16]

Briot and Arakelian (2009) extended this research to synthesize a dynamically balanced version of the PAMINSA. The basis of this balanced mechanism was the PAMINSA-3D3L (as described in [15]) of which drawings are shown in Fig. 5. The parallel structure of this mechanism has 3 translational DoFs, and the serial wrist has 3 rotational DoFs, resulting in a 6 DoF mechanism. Force balance of this mechanism was achieved using counter masses and moment balance by optimal control of the end-effector. It should be noted that the end-effector operates as a counter-rotation for moment balance in this manipulator; therefore, this manipulator only has 3 DoF when balanced.

V. Discussion

Like all other balanced manipulators in literature, the balancing of the spatial mechanisms described above came at the cost of a substantial increase in mass, which makes them less usable for aerial manipulation due to the payload limitation of aerial vehicles [2]. High masses of the moving links and counter-masses increase motor torques [8], and thereby stronger and heavier motors are required, which leads to an even larger increase in mass [10] of the mechanism.

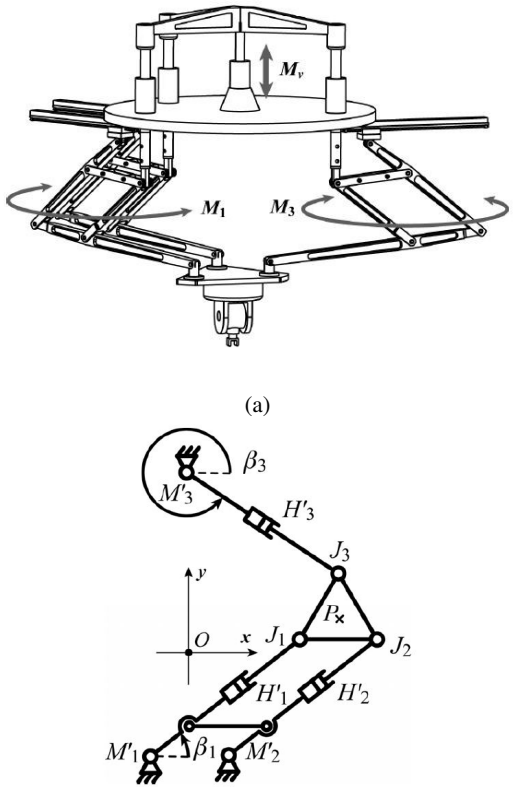

Fig. 5: Drawings of the PAMINSA manipulator that will be balanced. (a) PAMINSA-3D3L with a 3 DoF serial wrist [17] (b) Equivalent model for planar translation [17]

For balanced mechanisms, the total mass of the mechanism depends heavily on geometric choices and especially the length of moment arms. When longer moment arms are used, the masses of the counter-masses could be lower. However, this also leads to a decrease in rigidity, worsening the balancing quality due to internal vibrations. The manipulators presented in this paper were not optimized for low mass and proper rigidity and were made for different workspaces. Therefore, it is not possible to quantitatively compare these manipulators.

To the best of the author's knowledge, the four-bar mechanism (Fig. 3) is the only dynamically balanced manipulator in literature in which both force and moment balance are achieved without separate counter-rotations. Therefore no additional actuators or gears are needed for moment balance, and the 6 DoF mechanism is controlled using 6 actuators. However, the complexity increased substantially next to a large increase of the mass and footprint of the mechanism.

Comparing the parallelepiped with the four-bar mechanism, the most visible difference is that the 6 DoF four-bar mechanism consists of 6 more moving links than the 6 DoF parallelepiped mechanism. However, the parallelepiped mechanism uses a total of 15 counter masses, and 9 counter-rotations for moment balance that are driven by gears attached to the links. Thereby only 6 actuators are needed to control the linkage.

The parallelepiped has a very large footprint, just like the four-bar mechanism. According to Wu (2003), the mass and the footprint of both mechanisms could be reduced by optimizing geometric parameters, which could make them more usable for aerial manipulation. Another downside for both manipulators is that, according to the *equivalent mass method*, the design of the platform is restricted to a thin symmetric platform when using three legs [8].

With the PAMINSA manipulator, it was tried to simplify the kinematics of a spatial mechanism, and thereby its dynamics and control, by kinematically decoupling the horizontal and vertical motion of the manipulator. One of the benefits for this decoupling was that there is no gravitational work for the horizontal motion. However, when the manipulator is force balanced, there is also no gravitational work in the vertical direction due to the constant CoM of the manipulator.

Force balance of the PAMINSA was achieved using counter-masses just like the parallelepiped and the four-bar mechanisms. The total mechanism was also balanced in the same way as the other mechanisms by combining three balanced legs and including the platform with the *equivalent mass method*. Because the platform of the PAMINSA is only subjected to translational motion, a spatial platform can be included using only three legs in the *equivalent mass method* instead of 4 as in [12, 14]. Moment balance of this linkage was achieved by means of a serial wrist with three actuated rotations. Because the motion of the wrist is needed to balance the momentum of the system, the wrist does not add any DoFs, and the PAMINSA is only balanced for translational motion. Therefore, the PAMINSA uses six actuators for a 3 DoF balanced mechanism, or six actuators for a 6 DoF unbalanced mechanism. Although the balanced PAMINSA has fewer free DoFs, its design is substantially less complex than the other balanced manipulators.

VI. Conclusion

This literature survey showed that only three examples exist for dynamically balanced spatial manipulators. These are the parallelepiped [14], the compound four-bar [12], and the PAMINSA [17] manipulators. These were evaluated with regard to their potential use in aerial manipulation, in which mass increase due to balancing was the most apparent issue.

All balanced mechanisms led to a huge increase in the mass of the mechanism, and thereby none of the presented mechanisms is usable for aerial manipulation. This is mainly because of the addition of counter masses and an increased complexity due to balancing.

Although the presented manipulators are not yet usable for aerial manipulation, dynamically balanced spatial manipulators could be very useful for aerial manipulation, because they do not induce any perturbations to the base of the aerial vehicle, which enables fast movements.

REFERENCES

[1] F. Ruggiero, V. Lippiello, and A. Ollero, "Aerial Manipulation: A Literature Review," in *IEEE Robotics and Automation Letters*, vol. 3, Jul. 2018, pp. 1957–1964.

[2] A. Suarez, A. E. Jimenez-Cano, V. M. Vega, G. Heredia, A. Rodriguez-Castaño, and A. Ollero, "Lightweight and human-size dual arm aerial manipulator," in *2017 International Conference on Unmanned Aircraft Systems (ICUAS)*, Jun. 2017, pp. 1778–1784.

[3] G. G. Lowen and R. S. Berkof, "Survey of investigations into the balancing of linkages," *Journal of Mechanisms*, vol. 3, no. 4, pp. 221–231, Dec. 1968.

[4] H. Bonyan Khamseh, F. Janabi-Sharifi, and A. Abdessameud, "Aerial manipulation—A literature survey," *Robotics and Autonomous Systems*, vol. 107, pp. 221–235, Sep. 2018.

[5] Y. Wu and C. M. Gosselin, "Dynamic Balancing of Multi-Degree-of-Freedom Parallel Mechanisms With Multiple Legs," in *Volume 2: 28th Biennial Mechanisms and Robotics Conference, Parts A and B*. Salt Lake City, Utah, USA: ASMEDC, Jan. 2004, pp. 1293–1301.

[6] M. B. Beacom, "Synthesis and Control of a 3 Degrees of Freedom Inherently Dynamically Balanced Manipulator for an Unmanned Aerial Vehicle," Master's thesis, Delft University of Technology, Delft, Jan. 2021.

[7] V. van der Wijk and J. L. Herder, "Guidelines for Low Mass and Low Inertia Dynamic Balancing of Mechanisms and Robotics," in *Advances in Robotics Research: Theory, Implementation, Application*, T. Kröger and F. M. Wahl, Eds. Berlin, Heidelberg: Springer, 2009, pp. 21–30.

[8] Y. Wu, "SYNTHESIS AND ANALYSIS OF REACTIONLESS SPATIAL PARALLEL MECHANISMS," Ph.D. dissertation, Université Laval, Québec, 2003.

[9] R. Cano, C. Pérez, F. Pruaño, A. Ollero, and G. Heredia, "Mechanical Design of a 6-DOF Aerial Manipulator for assembling bar structures using UAVs," in *2nd RED-UAS 2013 Workshop on Research, Education and Development of Unmanned Aerial Systems*, Compiegne, France, 2013, p. 7.

[10] T. W. Danko, K. P. Chaney, and P. Y. Oh, "A parallel manipulator for mobile manipulating UAVs," in *2015 IEEE International Conference on Technologies for Practical Robot Applications (TePRA)*, May 2015, pp. 1–6.

[11] R. Ricard and C. M. Gosselin, "On the Development of Reactionless Parallel Manipulators," in *Volume 7A: 26th Biennial Mechanisms and Robotics Conference*. Baltimore, Maryland, USA: American Society of Mechanical Engineers, Sep. 2000, pp. 493–502.

[12] Y. Wu and C. M. Gosselin, "Synthesis of Reactionless Spatial 3-DoF and 6-DoF Mechanisms without Separate Counter-Rotations," *The International Journal of Robotics Research*, vol. 23, no. 6, pp. 625–642, Jun. 2004.

[13] A. R. Abdulghany, "Generalization of parallel axis theorem for rotational inertia," *American Journal of Physics*, vol. 85, no. 10, pp. 791–795, Oct. 2017.

[14] Y. Wu and C. M. Gosselin, "Design of reactionless 3-DOF and 6-DOF parallel manipulators using parallelepiped mechanisms," *IEEE Transactions on Robotics*, vol. 21, no. 5, pp. 821–833, Oct. 2005.

[15] S. Briot, V. Arakelian, and S. Guegan, "PAMINSA: A new family of partially decoupled parallel manipulators," *Mechanism and Machine Theory*, vol. 44, pp. 425–444, Feb. 2009.

[16] S. Briot, S. Guégan, E. Courteille, and V. Arakelian, "On the Design of PAMINSA: A New Class of Parallel Manipulators With High-Load Carrying Capacity," in *Volume 8: 31st Mechanisms and Robotics Conference, Parts A and B*. Las Vegas, Nevada, USA: ASMEDC, Jan. 2007, pp. 763–772.

[17] S. Briot and V. Arakelian, "Complete Shaking Force and Shaking Moment Balancing of the Position-Orientation Decoupled PAMINSA Manipulator," in *IEEE/ASME International Conference on Advanced Intelligent Mechatronics (AIM2009)*, Singapour, Singapore, Jul. 2009, pp. 1521–1526.

Chapter 3

Design of 3 DoF and 6 DoF Force and Moment Balanced Manipulators Based on the Spatial Pantograph Linkage

Design of 3 DoF and 6 DoF Force and Moment Balanced Manipulators Based on the Spatial Pantograph Linkage

Luuk Withagen
High-Tech Engineering
Delft University of Technology
Delft, the Netherlands
L.W.J.Withagen@student.tudelft.nl

***Abstract*—This article presents the design of novel 3 DoF and 6 DoF force and moment balanced spatial manipulators based on the spatial pantograph linkage. It is shown how the general spatial pantograph linkage can be constrained to a dynamically balanced 3 DoF manipulator, which can also be applied as a leg in a parallel 6 DoF manipulator. Three different designs for the 3 DoF linkage are presented: a force balanced manipulator using 2 counter masses, a dynamically balanced manipulators using 4 counter masses and 3 counter-rotations, and a dynamically balanced manipulator using 3 counter masses and 3 counter-rotations. The forward and inverse kinematics for the proposed 3 DoF manipulators are presented together with the workspace boundaries. The dynamic balance conditions for this linkage are derived using the conservation of linear and angular momentum, and verified using the dynamic simulation software ADAMS. The knowledge of the 3 DoF manipulators is used to synthesize three 6 DoF manipulators: a force balanced manipulator using 6 counter masses, a dynamically balanced manipulator using 12 counter masses and 9 counter-rotations, and a dynamically balanced manipulator using 9 counter masses and 9 counter-rotations. A physical demonstrator was built for the first dynamically balanced 6 DoF manipulator, which shows the feasibility of the proposed design.**

***Index Terms*—Dynamic balancing, parallel linkage, spatial linkage, reactionless, spatial pantograph**

I. Introduction

When a robot moves, it generates reaction forces and reaction moments on its base. These forces are especially considerable if the robots move at high speeds [1]. The existence of these forces in the base of a manipulator could lead to unwanted effects such as vibrations, noise, wear and fatigue problems, which all limit the full potential of the robotic arm [1]. These problems will become even more evident when the robotic arm is attached to an unstable base, like in aerial manipulation [2].

There are multiple ways to overcome the effects of reaction forces and moments. One way could be to heavily increase the rigidity of the base to which the robotic arm is attached [3]. Other methods tend to remove reaction forces and moments through the design of the linkage. These kinds of linkages could be categorized into three categories: *Force-Balanced*, *Moment-Balanced*, and *Dynamically Balanced*. A linkage is said to be force-balanced when the sum of reaction forces on its base is zero throughout its motion. Similarly, a linkage is said to be moment-balanced when the sum of reaction moments on its base is zero. When a linkage is both force and moment balanced, it is said to be dynamically balanced.

A large amount of research concerning the dynamic balancing of linkage was performed on the synthesis and design of planar linkages. However, the dynamic balance of multi-degree-of-freedom linkages that move spatially has only been touched upon slightly [4] since it is extremely challenging to obtain practical results. To the best of the author's knowledge, only three examples of dynamically balanced spatial manipulators exist. These are the parallelepiped [5], the compound four-bar [6], and the PAMINSA [7] manipulators. Another interesting linkage that is only force balanced is the spatial pantograph linkage [8]. This linkage has 6 degrees of freedom (DoF) and is balanced using only two counter masses.

The goal of this paper is to present three novel 3 DoF spatial force and moment balanced linkages, which could be used as legs to synthesize three 6 DoF spatial force and moment balanced linkages. The proposed linkage is based on the general spatial pantograph linkage presented by Van der Wijk (2022).

First, the general spatial pantograph linkage will be constrained to a 3 DoF manipulator, so that it could be used as a leg for a 6 DoF manipulator. For this proposed linkage, the forward and backward kinematics are presented from which the singularities and thereby the workspace boundaries are calculated. Then, the dynamic balance conditions will be determined using the conservation of linear and angular momentum, of which the results are verified using the dynamic simulation software ADAMS. Lastly, the conditions for using the 3 DoF linkages as legs for parallel 6 DoF linkages will be discussed, after which a physical demonstrator for the 6 DoF dynamically balanced manipulator is presented.

II. Kinematic Analysis

The general spatial pantograph developed by Van der Wijk (2022) is a 6 DoF linkage in which all DoFs can be actuated at the base [8]. Although this linkage has 6 DoFs, it is not possible to independently control three rotational and three

translational DoFs at the end-effector point A. However, if constraints are applied to this linkage, it could be used as a leg for a 6 DoF parallel linkage with the minimal number of actuators. As can be verified using the *Chebychev-Grübler-Kutzbach criterion* (Equation 1), the addition of a platform adds 6 DoF, and the connection of this platform with the legs retracts 9 DoF. In order to synthesize a 6 DoF linkage, the legs should have 9 DoF in total, which results in 3 DoF per leg. Therefore the general spatial pantograph will be constrained to have 3 DoF instead of 6.

A schematic representation of the proposed linkage can be seen in Figure 1a. In this linkage, link 2 is attached to the base (point S) with a revolute joint which only allows for a rotation around the inertia X-axis (θ_3). Link 1 is a 2 DoF joint that first rotates around the inertia Z-axis (θ_1) and then rotates around its body-fixed Y-axis (θ_2). Links 1, 3, 5 and 7 have length a_1, links 2, 4, 6 and 8 have length a_1 and the distance between point A' and point A is a_3. Because of the equal lengths of opposing links and the addition of out-of-plane links, the parallelogram shape is maintained throughout the full motion of the linkage. Links 1 through 4 could have non-concentric centres of mass (CoM's) but these were left out for clarity in the Figure.

The mobility M of this linkage could be calculated using the *Chebychev-Grübler-Kutzbach criterion* for spatial mechanisms,

$$M = 6n - \sum_{i=1}^{j}(6 - f_i) \tag{1}$$

where n is the number of moving links, j is the number of joints and f_i is the degree of freedom of these joints. The constrained spatial pantograph linkage consists of 8 moving links ($n = 8$), 3 spherical joints ($f_s = 3$), 9 universal joints ($f_u = 2$), and one revolute joint ($f_r = 1$). This results in $M = -2$. However, since only two out-of-plane links are sufficient and already result in one overconstraint [8], the addition of 2 more out-of-plane links results in a linkage with 5 overconstraints. Thus the linkage has 3 DoF. These overconstraints could be eliminated by replacing some of the universal joints with spherical joints. However, the overconstraints also add rigidity to the linkage and therefore won't be removed in this design.

A. Forward Kinematics

The forward kinematics of a linkage describes which end-effector position is reached with a specified set of input angles. Using the rotational directions from Figure 1a, the forward kinematics solution for the end-effector equals:

$$\mathbf{p}_A = \begin{pmatrix} (a_1 + a_3)\,\cos(\theta_1)\,\cos(\theta_2) \\ (a_1 + a_3)\,\sin(\theta_1)\,\cos(\theta_2) + a_2\,\cos(\theta_3) \\ -\,(a_1 + a_3)\,\sin(\theta_2) + a_2\,\sin(\theta_3) \end{pmatrix} \tag{2}$$

These results were verified using quaternions (Appendix A) and by comparing numerical results to a SolidWorks model.

B. Inverse Kinematics

The inverse kinematics of a linkage describe which input angles are needed to reach a desired position with the end-effector. Although Equation 2 seems fairly simple, no analytical solution could be found by just setting Equation 2 equal to a numerical vector. This is the case because multiple inverse kinematic solutions (postures [9]) exist for the proposed linkage, and due to the non-linearity in the equation.

A geometric method was used to find solutions to the inverse kinematics of the constrained spatial pantograph linkage. This method uses the two known points in the inverse kinematic problem; the base (Point S) and the desired end-effector position (Point A). Next to that, it uses the fact that the link lengths do not change during the motion of the linkage. Link 2 constrains point P_1 such that it has to lie on a circle with radius a_2 in the yz-plane around point S. Also, link 3 constraints point P_1 such that is has to be on a sphere around point A with radius $a_1 + a_3$. So, point P_1 should be on one of the intersection points between the black circle and the sphere as shown with blue dots in Figure 2.

In order to find the intersection points between the black circle and the coloured sphere in Fig. 2, the circle that is formed by the intersection of the sphere with the yz-plane is first calculated (red circle in Figure 2). The first step in doing this is defining the goal position of point A as:

$$\mathbf{A}_{goal} = \begin{pmatrix} a_x & a_y & a_z \end{pmatrix}^\intercal \tag{3}$$

For the proposed linkage, this vector can be split up in respectively a component perpendicular to the yz-plane and a component along this plane:

$$\mathbf{A}^{\perp}_{goal} = \begin{pmatrix} a_x & 0 & 0 \end{pmatrix}^\intercal \tag{4}$$

$$\mathbf{A}^{\parallel}_{goal} = \begin{pmatrix} 0 & a_y & a_z \end{pmatrix}^\intercal \tag{5}$$

Vector $\mathbf{A}^{\parallel}_{goal}$ defines the distance between the origin at S and the centre of the circle slice (drawn in red in Fig. 2) of the sphere on the yz-plane. The radius of this circle can be calculated using *Pythagoras' Theorem* with the radius of the sphere and the perpendicular distance from the plane to the centre of the sphere:

$$r_{slice} = \sqrt{(a_1 + a_3)^2 - a_x^2} \tag{6}$$

The next step in solving the inverse kinematics is finding the intersection points of the circles. In order to simplify computations, the intersection points will first be calculated as if the circles lie on the y-axis, and afterwards the solutions are rotated back. The solution for when both circles would be on the y-axis (dashed lines in Fig. 3) could be calculated using

$$y_{intersection} = \frac{a_2^2 - r_{slice}^2 + d^2}{2d} \tag{7}$$

in which d equals the distance between both circle centres, $d^2 = a_y^2 + a_z^2$.

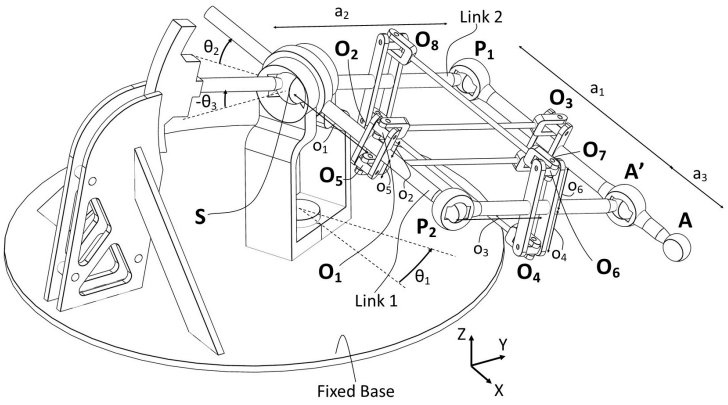

(a) Kinematic model of the 3 DoF constrained spatial pantograph in which point S as its base rotation point and point A as its end-effector point. Link 1 has two DoF motion capability (*Yaw* (θ_1) around the inertia Z-axis, *Pitch* (θ_2)) around the body-fixed Y-axis, and Link 2 has one DoF motion capability (*Pitch* (θ_3) around the inertia X-axis).

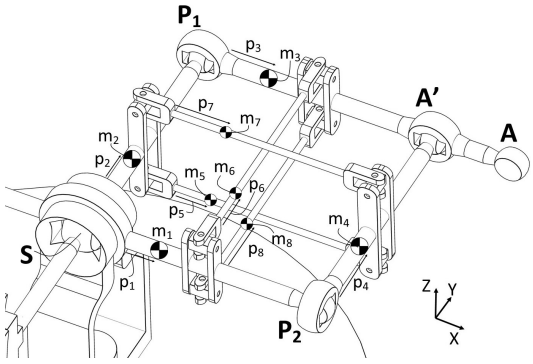

(b) Mass parameters for the 3 DoF constrained spatial pantograph linkage.

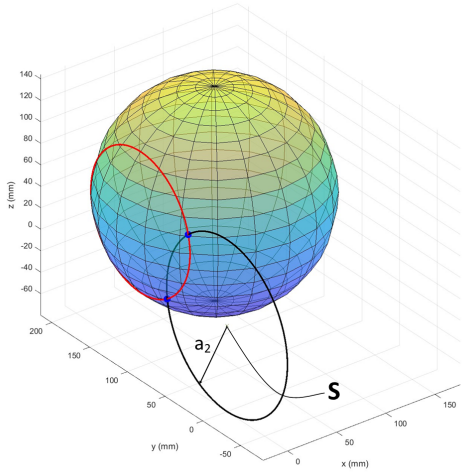

Fig. 2: Geometric approach for the inverse kinematics in which all possible positions for point P_1 from point A are depicted by a sphere, and the possible positions for P_1 from point S by the black circle. Inverse kinematics solutions can be found at the intersection points between the black circle and the sphere.

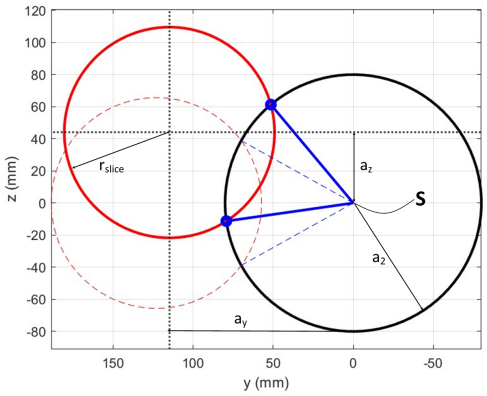

Fig. 3: Slice of the yz-plane which is used to calculate the solution for θ_3 using the geometric approach for the inverse kinematics. Point S is at $(0, 0)$ and the possible positions for point P_1 are shown with blue circles.

After rotating the circles back, the solutions for θ_3 become:

$$\theta_3 = \tan^{-1}(\frac{a_z}{a_y}) + \cos^{-1}(\frac{y_{intersection}}{a_2}) \quad (8)$$

$$\theta_3 = \tan^{-1}(\frac{a_z}{a_y}) - \cos^{-1}(\frac{y_{intersection}}{a_2}) \quad (9)$$

These solutions are depicted in Figure 3 using thick blue lines.

After finding the solution for θ_3, the solutions of the other two angles could be easily found using Equation 2. With this approach, it could be calculated that the linkage has four possible working modes, which refers to two solutions per intersection point between the circles. For the solutions of one intersection point (the same value for θ_3), the relation between the first and second solution could be written as $\theta_{1,2} = 180 + \theta_{1,1}$ and $\theta_{2,2} = 180 - \theta_{2,1}$.

The inverse kinematics were also solved using a *non-linear least squares optimization*, which can be found in Appendix B.

C. Singularities

Singularities of a linkage are configurations in which no cartesian velocity can be produced [9] or in which the linkage is locally moveable although the actuators are locked [10]. The first kind is called a *serial singularity* and mathematically means that the Jacobian of the linkage becomes rank deficient [11], i.e. the determinant of the jacobian becomes zero. The second kind is a *parallel singularity* and thus only occurs in parallel mechanisms. For the constrained spatial pantograph

linkage, this type of singularity will occur when the linkage is stretched-out over the y-axis.

The determinant of the jacobian for the constrained spatial pantograph linkage equals:

$$D = (a_1 + a_3)^2 a_2 \cos(\theta_2) \left[\sin(\theta_2)\cos(\theta_3) + \sin(\theta_1)\cos(\theta_2)\sin(\theta_3)\right] \tag{10}$$

Firstly, the configurations in which the determinant equals zero are found in joint space. This is done by discretization of the workspace for θ_1 and θ_2 between $-\pi/2$ and $\pi/2$ and calculating solutions for θ_3 by which the determinant becomes zero. The results for the singularity surface in joint space can be seen in Fig. 4. If this analysis were performed for a larger domain, the shown singularity surface would repeat, and planes can be seen when $\theta_2 = \pi/2 \pm n\,\pi$, but this is left out for clarity in this Figure.

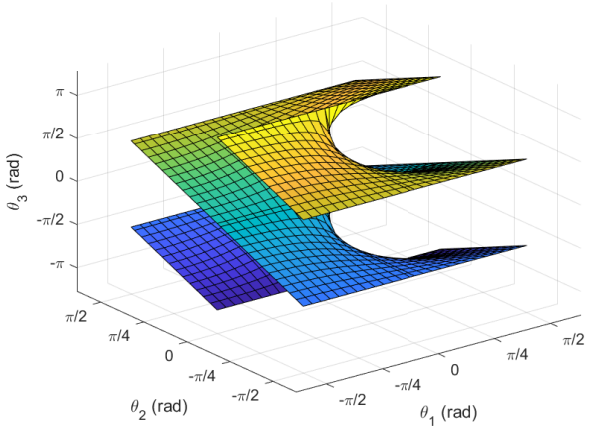

Fig. 4: Singularity surface in joint space for the constrained spatial pantograph mechanism for $-\pi/2 \leq \theta_1 \leq \pi/2$, $-\pi/2 \leq \theta_2 \leq \pi/2$ and $-\pi \leq \theta_3 \leq \pi$

After the singularity surface in joint space was calculated, the results were transformed into cartesian space by filling in the angles of the singularity configurations into Eq. 2. These results can be seen in Figure 5, which shows half of the singularity surface. The linkage is in a singular configuration for each configuration in which end-effector point A intersects the singularity surface.

D. Workspace Bounds

The last part of this kinematic analysis is the determination of the workspace of the constrained spatial pantograph linkage, which defines all points that can be reached with the manipulator. The singularity surface (as can be seen in Figure 5) represents the points at which there is a direction in which no cartesian velocity can be produced [9]. Because point A cannot move through this surface, the singularity surface equals the workspace boundary for the constrained spatial pantograph linkage. The small cone shape around the x-axis of Figure 5 is excluded from the workspace, i.e. points

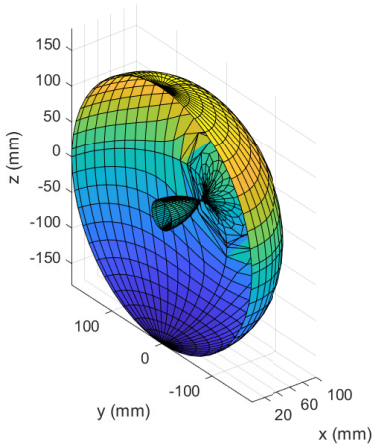

Fig. 5: Positive x side of the singularity surface in cartesian space for the constrained spatial pantograph mechanism

inside this region are not reachable with the constrained spatial pantograph linkage. In this region, the sphere and the circle as described in the geometric inverse kinematics method, do not intersect; therefore, no solutions can exist.

Two more methods were used to calculate the workspace boundaries, which can be found in Appendix D.

III. Force Balance

When the sum of the reaction forces on the base of a linkage is zero during motion, it is said to be force balanced. There are multiple ways to obtain conditions for force balance. One way could be to calculate the total linear momentum of the linkage and search for conditions for which this equation remains zero during motion. Another method could be to calculate the total CoM of the linkage and search for conditions in which this CoM remains constant during motion. The force-balance conditions for the general spatial pantograph linkage [8] could be rewritten for the constrained spatial pantograph linkage in Figures 1a and 1b as:

$$m_1 p_1 + m_4 a_1 + m_3 p_3 + m_5 p_5 + m_6 o_1 + m_7 p_7 + m_8 o_1 = 0 \tag{11}$$

$$m_2 p_2 + m_3 a_2 + m_4 p_4 + m_5 o_3 + m_6 p_6 + m_7 o_3 + m_8 p_8 = 0 \tag{12}$$

$$m_1 q_1 + m_3 q_3 = 0 \tag{13}$$

$$m_1 q_1' + m_3 q_3' + m_6 o_2 - m_8 o_5 = 0 \tag{14}$$

$$m_2 q_2' + m_4 q_4' - m_5 o_4 + m_7 o_6 = 0 \tag{15}$$

In which q_i' is the CoM offset in the positive z-direction and q_i is the CoM offset perpendicular to the z-direction and the longitudinal axis of the link. These were left out for clarity in Figure 1b because they will be set to in the moment balance conditions.

Next to that, there is one condition less than for the general spatial pantograph. Due to the constraint on link 2, by which it only allows for motion around the x-axis, the centre of mass does not have to lie on the x-axis in order to achieve a constant centre of mass.

A CAD model of the force balanced constrained spatial pantograph linkage is shown in Figure 6. This linkage has 3 DoF that are balanced using only 2 counter masses.

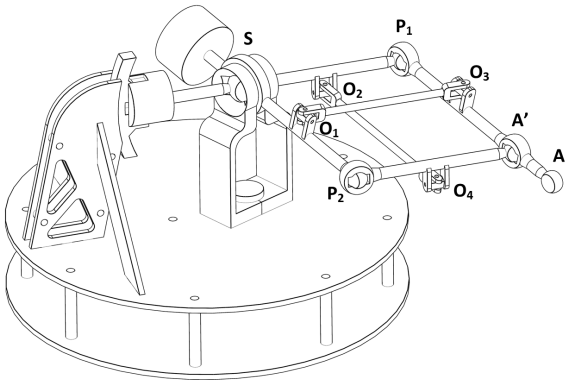

Fig. 6: CAD model of the 3 DoF dynamically balanced constrained spatial pantograph linkage

IV. Moment Balance

A linkage that does not induce any reaction moments on its base is said to be moment balanced. This section will first look at the moment balance for a 1 DoF link. Afterwards, the moment balance for a 2 DoF link will be investigated, and this knowledge will be combined to obtain moment balance conditions for the constrained spatial pantograph linkage.

A. Moment Balance of a 1 DoF Joint

At first, the moment balance conditions for a 1 DoF link are presented. Moment balance in such a link could be achieved by using a linkage such as the inverted four-bar [6] or by using counter-rotations [5]. The example 1 DoF link that will be discussed here rotates around the x-axis and is balanced using counter-rotations as it is the easiest method for moment balance.

In order to balance a 1 DoF linkage, an inertia wheel with exactly the same product of the angular velocity and the moment of inertia around the rotation axis as the link could be added with gears such that it rotates in the opposite direction. Due to the symmetry of a wheel, it has zero products of inertia. Therefore, all products of inertia, except for the one perpendicular to the rotation axis, should be zero.

There are no constraints on the other moments of inertia because the link does not rotate around these axes.

With the notion that the CoM of the link lies on the rotation point due to its force-balance conditions, and the inertia of the link also includes the inertia of the counter-mass, the moment-balance conditions for a 1 DoF link are:

$$I_{xx,CR} = I_{xx} \tag{16}$$
$$I_{xy,CR} = I_{xy} = 0 \tag{17}$$
$$I_{xz,CR} = I_{xz} = 0 \tag{18}$$

B. Moment Balance of a 2 DoF Joint

After balancing a 1 DoF joint, the balancing conditions for a 2 DoF rotational joint will be investigated. Link 1 of the constrained spatial pantograph linkage is such a link in which firstly, a *yaw* rotation is executed around the inertial z-axis (θ_1) and afterwards, a *pitch* rotation around the body-fixed y-axis (θ_2). The goal is to balance both rotations passively by just using counter-rotations.

1) Inertia Tensor Conditions: In order to moment-balance the *yaw* rotation with a counter-rotation, all inertia values concerning rotations around the inertial z-axis (the third column of the rotated inertia tensor) should be independent of the value of θ_2. Otherwise, a very complex variable transmission would be needed. In order to achieve a constant inertia tensor around the z-axis, all values in the third column of the rotated inertia tensor should be constant.

The rotation matrix for the pitch rotation could be written as:

$$\mathbf{R} = \begin{pmatrix} \cos(\theta) & 0 & \sin(\theta) \\ 0 & 1 & 0 \\ -\sin(\theta) & 0 & \cos(\theta) \end{pmatrix} \tag{19}$$

Then the third column of the rotated inertia ($\mathbf{R}\,\mathbf{I}\,\mathbf{R}^\intercal$) tensor is computed:

The value for the rotated inertia $I_{yz,1,rot}$ equals:

$$I_{yz,rot} = I_{yz}cos(\theta) - I_{xy}sin(\theta) \tag{20}$$

From this, it can be concluded that $I_{yz} = I_{xy} = 0$.

The value for the rotated inertia $I_{xz,rot}$ equals:

$$\begin{aligned} I_{xz,rot} = I_{xz}\left[\cos^2(\theta) - \sin^2(\theta)\right] \\ + \left(I_{zz} - I_{xx}\right)\sin(\theta)\cos(\theta) \end{aligned} \tag{21}$$

This results in the conditions $I_{xx} = I_{zz}$ and $I_{xz} = 0$. Lastly, there will be looked at the value for $I_{zz,rot}$:

$$\begin{aligned} I_{zz,rot} = I_{xx}\sin^2(\theta) + I_{zz}\cos^2(\theta) \\ -2\,I_{xz}\cos(\theta)\sin(\theta) \end{aligned} \tag{22}$$

With the conditions above, this value will be independent of θ_2. Therefore, the inertia conditions for a 2 DoF moment balanced link rotating around its CoM (Force Balance) are:

$$I_{xx} = I_{zz} \tag{23}$$
$$I_{xy} = 0 \tag{24}$$
$$I_{xz} = 0 \tag{25}$$
$$I_{yz} = 0 \tag{26}$$

2) Counter-Rotation Dimension: Because a 2 DoF link is balanced and a counter-rotation can only balance 1 DoF, two counter-rotations are required. They have inertia tensors $\mathbf{I}_{CR2}$ and $\mathbf{I}_{CR1}$ for the *Pitch* and *Yaw* counter-rotation respectively.

At first, the *pitch* rotation will be balanced. This will be done by adding a counter-rotation $\mathbf{I}_{CR2}$ to the link, which will also experience the *yaw* motion, but in opposite direction. This counter-rotation should compensate for the pitch motion of the link while also having a constant inertia around the inertial z-axis which results in the following conditions:

$$I_{yy,CR2} = I_{yy} \tag{27}$$
$$I_{xy,CR2} = I_{xy} = 0 \tag{28}$$
$$I_{xz,CR2} = I_{xz} = 0 \tag{29}$$
$$I_{yz,CR2} = I_{yz} = 0 \tag{30}$$
$$I_{xx,CR2} = I_{zz,CR2} \tag{31}$$

Next to these conditions, the CoM of the counter-rotation should be on the inertial z-axis to remain force-balanced. A displaced CoM would cause a nonzero linear momentum and thereby, reaction forces on the base. Therefore, another condition is that the x- and y-position of the CoM of the counter inertia are zero.

The other counter-rotation will be used to balance the *yaw* rotation of the link. This inertia also has to balance the motion of the other counter-rotation. Because the link and the other counter-rotation both do not have any products of inertia, the products of inertia of this counter-rotation should also be zero.

$$I_{zz,CR1} = I_{zz} + I_{zz,CR2} \tag{32}$$
$$I_{xy,CR1} = 0 \tag{33}$$
$$I_{xz,CR1} = 0 \tag{34}$$
$$I_{yz,CR1} = 0 \tag{35}$$

3) Equivalent Inertia Method: Conditions 23 and 31 both imply that the inertia around the body-fixed x-axis should equal the inertia around the body-fixed z-axis. For the counter-rotation, this is simple, because this is always true for a round wheel. For the link itself, this is harder. The easiest way is to place an exact copy of the link at a 90 degrees offset, but it will be hard to meet the balance conditions for the constrained spatial pantograph linkage later.

Another method could be to calculate shapes that could be added to the link that adjust the inertia so that the inertia conditions are met. This could be done with all kinds of shapes, but it is now chosen to use cylinders.

The inertia for with density ρ and the variables from Figure 7 placed on link 1 could be calculated as follows:

$$I_{xx,ei} = \frac{\pi \rho h r_{ei}^2}{6}(12d_{ei}^2 + 12d_{ei}h_{ei} + 4h_{ei}^2 + 3r_{ei}^2) \tag{36}$$
$$I_{yy,ei} = I_{xx,ei} \tag{37}$$
$$I_{zz,ei} = \pi \rho h_{ei} r_{ei}^4 \tag{38}$$

The conditions are met when:

$$I_{xx} + I_{zz,ei} = I_{zz} + I_{xx,ei} \tag{39}$$

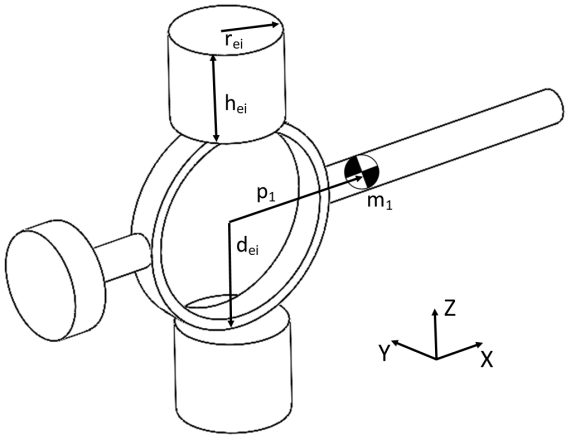

Fig. 7: Schematic representation of link 1 for the parameters concerning the equivalent inertia method

These conditions were verified by simulating 2 DoF joint that meets all the conditions using the dynamic simulation software ADAMS. Results from this simulation can be found in Appendix G.

C. Moment Balance of the Complete Linkage

In order to passively balance the constrained spatial pantograph linkage, all link rotations or translations should have linear relations with one of the input links (links 1 and 2). This is true for all links except the out-of-plane links (link 5 through 8). The rotation of these links around their length axis is dependent on all input angles, and shows non-linear relations with these input angles. Therefore, it is impossible to exactly balance the constrained spatial pantograph linkage, but approximate balance is possible. In order to achieve approximate balance, the inertia of the out-of-plane link around its length axis should be as low as possible (because this rotation cannot be compensated), and the inertia around its other two axis should be equal. The moment of inertia around the two axes perpendicular to the length axis will be described by I_i in which i is the number of the out-of-plane link. Appendix E elaborates further on the nonlinear relations of the out-of-plane links.

In the previous two examples for the 1 DoF link and the 2 DoF link, the CoM's had a constant distance to the base of the linkage. This could be achieved by setting both p_3 and p_4 to zero and thereby putting their CoMs in point P_1 and P_2 respectively, which would result in 4 countermasses. However, similar to Foucault and Gosselin (2005), it is possible to balance the linkage using only 3 counter-masses.

It was already stated in the example of a 1 DoF link that all products of inertia should be zero except for the one in the plane of rotation. For link 2 this means that $I_{yz,2}$ could be nonzero. Because link 4 rotates similarly to link 2, the same

also holds for link 4. Their other two products of inertia could compensate for each other:

$$I_{xy,2} + I_{xy,4} = 0 \tag{40}$$
$$I_{xz,2} + I_{xz,4} = 0 \tag{41}$$

The same holds for link 1, with the difference that in this link, no products of inertia sums could be nonzero due to its 2 DoF motion. The products of inertia in the xz-plane should also compensate for the masses of the out-of-plane links.

$$I_{xy,1} + I_{xy,3} = 0 \tag{42}$$
$$I_{xz,1} + I_{xz,3} + m_8 o_1 o_5 - m_6 o_1 o_2 = 0 \tag{43}$$
$$I_{yz,1} + I_{yz,3} = 0 \tag{44}$$

There are two more conditions that the out-of-plane links should fulfil regarding the mass properties:

$$m_6 p_6 o_2 = m_8 p_8 o_5 \tag{45}$$
$$m_5 p_5 o_4 = m_7 p_7 o_6 \tag{46}$$

From the conservation of angular momentum, the following conditions are obtained:

$$\begin{aligned} I_{xx,1} + I_{xx,3} = I_{zz,1} + m_1 p_1^2 + I_{zz,3} + m_3 p_3^2 \\ + m_4 a_1^2 + m_5 p_5^2 + I_5 + m_6 o_1^2 - m_6 o_2^2 + m_7 p_7^2 \\ + I_7 + m_8 o_1^2 - m_8 o_5^2 + I_{zz,\theta_2} - I_{xx,\theta_2} \end{aligned} \tag{47}$$

$$\begin{aligned} m_3 p_3 a_2 + m_4 p_4 a_1 + m_5 p_5 o_3 + m_6 p_6 o_1 \\ + m_7 p_7 o_3 + m_8 p_8 o_1 = 0 \end{aligned} \tag{48}$$

$$\begin{aligned} I_{yy,\theta_2} = I_{yy,1} + I_{yy,3} + m_1 p_1^2 + m_3 p_3^2 + m_4 a_1^2 \\ + m_5 p_5^2 + I_5 + m_6 o_1^2 + m_6 o_2^2 + m_7 p_7^2 \\ + I_7 + m_8 o_1^2 + m_8 o_5^2 \end{aligned} \tag{49}$$

$$I_{zz,\theta_1} = I_{xx,1} + I_{xx,3} + I_{zz,\theta_2} + I_{zz,base} \tag{50}$$

$$\begin{aligned} I_{xx,\theta_3} = I_{xx,2} + I_{xx,4} + I_6 + I_8 + m_2 p_2^2 \\ + m_3 a_2^2 + m_4 p_4^2 + m_5 o_3^2 + m_5 o_4^2 \\ + m_6 p_6^2 + m_7 o_3^2 + m_7 o_6^2 + m_8 p_8^2 \end{aligned} \tag{51}$$

With these conditions, it is possible to dynamically balance the constrained spatial pantograph linkage with 3 countermasses and 3 counter-rotations. A picture of the CAD model of the dynamically balanced constrained spatial pantograph linkage can be seen in Figure 8.

Different mechanisms are possible with the presented balance conditions. For example, Figure 9 shows a linkage that could be balanced using only 3 countermasses. Removing the countermass on link 4 reduces the size of the countermass and equivalent inertia's on link 1, but increase the size of the countermass for link 2 and link 3.

A more elaborate calculation for the moment balance conditions can be found in Appendix F.

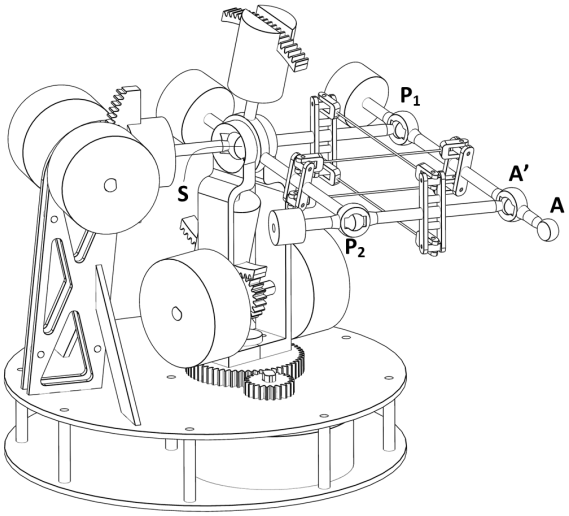

Fig. 8: CAD model of the 3 DoF dynamically balanced constrained spatial pantograph linkage

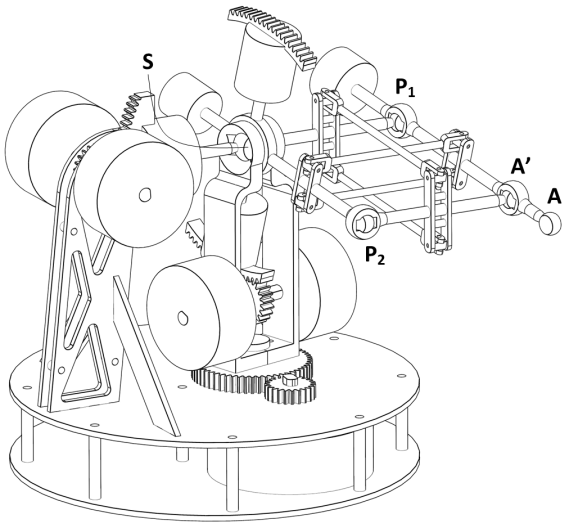

Fig. 9: CAD model of the alternative 3 DoF dynamically balanced constrained pantograph linkage using only 3 countermasses

V. Verification of the balance conditions

In order to verify the balancing conditions, a simulation was performed using the dynamic simulation software ADAMS. A screenshot of the simulation model for the constrained spatial pantograph can be seen in Figure 10 in which the counter-rotation for θ_1 is coloured cyan, the one for θ_2 green and the one for θ_3 blue. The equivalent inertia masses are coloured red. Because it is impossible to compensate for the roll rotation of the out-of-plane links, it is important to make these links as light and slim as possible to have a negligible moment of inertia around its length axis. This is also beneficial for the mass balance of the linkage, as with lower masses, smaller

counter masses and inertia are needed. Because the masses of the out-of-plane links will be low compared to the other masses of the linkage, and the ADAMS model did not allow for overconstraints, all the out-of-plane links were modelled as massless and with zero inertia. The link lengths a_1 and a_2 were set to 80 mm, and a_3 was set to 20 mm. The numerical mass and inertia values can be found in Table I.

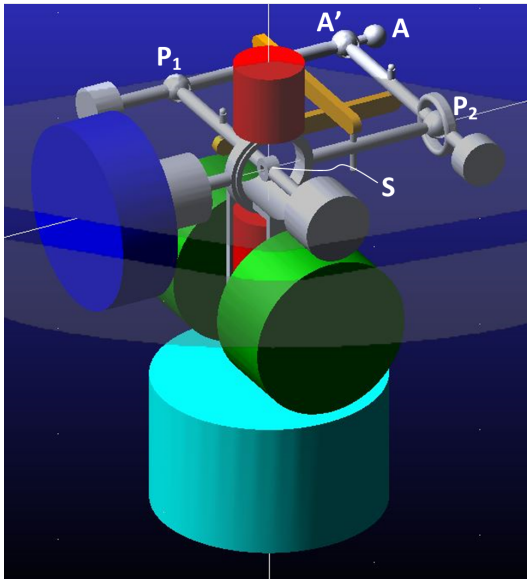

Fig. 10: Screenshot of the model used in the ADAMS simulation in which the equivalent inertia masses are coloured red, the counter-rotations for θ_1 cyan, the counter-rotation for θ_2 green and the counter-rotation for θ_3 blue

The mass and CoM values were obtained from the SolidWorks model with a density of 0.001 g/mm^3, and afterwards, values for the link masses and inertia's were slightly adjusted in order to satisfy the balance conditions with the maximum precision from ADAMS. Torques were applied to the input links with counter-torques of the same magnitude but opposite direction to the counter-rotations. For the tests presented in this article, the input torques in Nm were:

$$T_{\theta_1} = 15\cos(3\pi\, t) \tag{52}$$
$$T_{\theta_2} = 10\cos(4\pi\, t) \tag{53}$$
$$T_{\theta_3} = 5\cos(5\pi\, t) \tag{54}$$

Two tests were performed: one in which the counter-rotations do not move, and one in which the counter-rotations are moving in opposite direction of the links. For both tests, the reaction forces and reaction moments were measured at the base of the linkage. The results from these tests can be seen in Figures 12 and 13 respectively. For both graphs, the reaction forces at the base are equal because the presence of counter-rotation does not attribute to the force balance of the linkage. As a reference, the position of point A for the balanced case is shown in Figure 11.

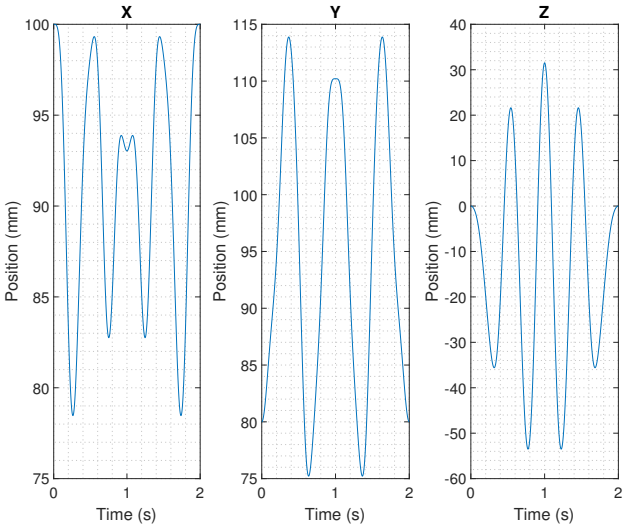

Fig. 11: Position of the end-effector point A in the simulator for the balanced case

The results demonstrate that the reaction moments in the balanced case are very small compared to the unbalanced case. The reaction moments do not exactly become zero, but this is attributed to numerical integration errors and the finite accuracy of the values that can be inputted into ADAMS. When the step size of the integrator is changed, the near-zero results change heavily while the other values remain identical, which could also be attributed to numerical errors. More on this can be found in Appendix H.

VI. Synthesis of a 6 DoF Moment Balanced Linkage

The 3 DoF dynamically balanced linkage as described in this article is used to synthesize a 6 DoF parallel spatial manipulator, which is dynamically balanced with 12 counter-masses and 9 counter-rotations. A CAD drawing of this manipulator is shown in Figure 14, in which three symmetrically placed dynamically balanced constrained spatial pantographs are connected to a platform using spherical joints.

It is also possible to synthesize a 6 DoF dynamically balanced linkage using the alternative design for the dynamically balanced constrained spatial pantograph linkage from Figure 9. With this linkage as legs, a 6 DoF manipulator was synthesized using 9 counter-masses and 9 counter-rotations.

For both designs, only two of the three input angles have to be actuated in each leg, so the full 6 DoF linkage could be actuated using 6 actuators.

A. Inclusion of Platform in the Balancing Conditions

The configuration of each leg contributes to the orientation of the platform. Therefore, it has no linear relation to one of the input links, and it is not possible to include the inertia of the platform in the balance conditions directly.

A solution to be able to include the platform into the balance conditions is by using the *equivalent mass method*

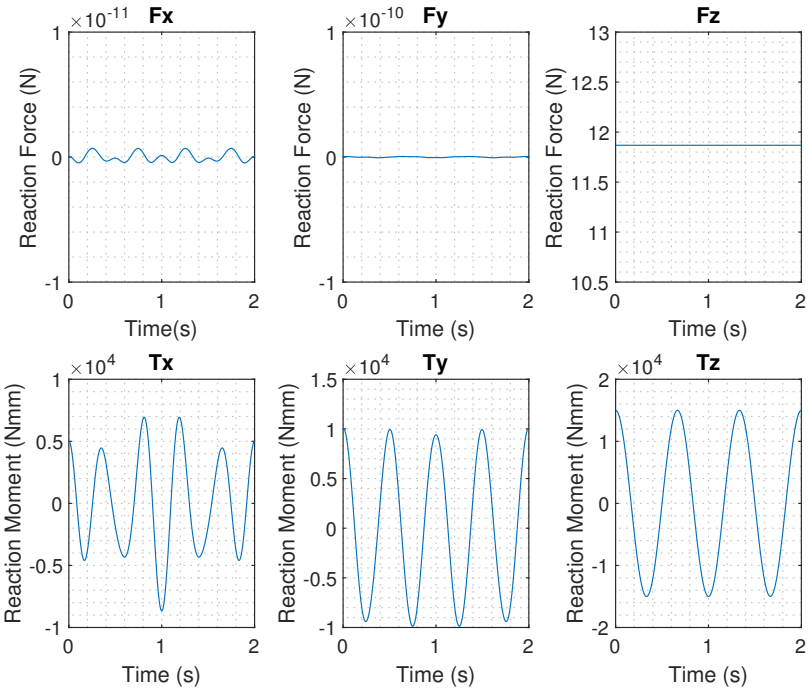

Fig. 12: Resultant reaction forces and moments at the base for the unbalanced case (no motion of the counter-rotations) of the 3 DoF constrained spatial pantograph linkage. These figures show very small resultant reaction forces due to the force balance, but high resultant reaction moments.

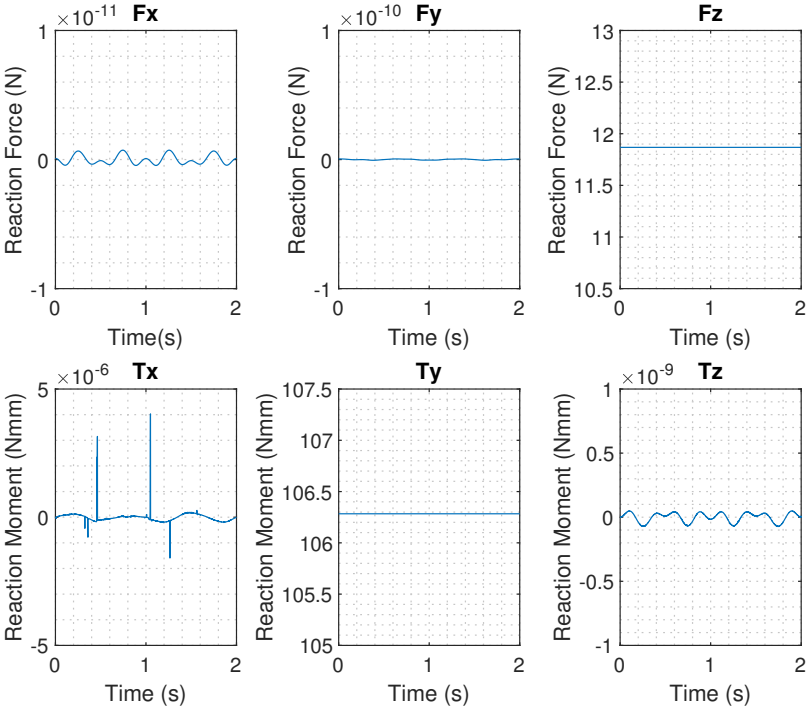

Fig. 13: Resultant reaction forces and moments at the base for the balanced case of the 3 DoF constrained spatial pantograph linkage. These figures show very small deviations in the resultant reaction forces and moments that are due to the finite precision that can be used in ADAMS.

Link i	m_i (g)	p_i (mm)	$I_{xx,i}$ (g mm^2)	$I_{yy,i}$ (g mm^2)	$I_{zz,i}$ (g mm^2)	$I_{xy,i}$ (g mm^2)	$I_{xz,i}$ (g mm^2)	$I_{yz,i}$ (g mm^2)
1	72.189210400	−7.96100000	109602.97490	144720.12045	41222.634010	0	0	100
2	18.034617473	−32.4543449	24455.789931	1601.9283804	24451.240450	0	0	0
3	7.0000000000	−3.61452800	221.69800000	15945.933000	15935.412000	0	0	0
4	7.5000000000	3.37355947	11764.840197	272.32959380	11676.603840	0	0	0
5	0	60	0	0	0	0	0	0
6	0	60	0	0	0	0	0	0
7	0	60	0	0	0	0	0	0
8	0	60	0	0	0	0	0	0
cr, θ_1	601.90000000	not applicable	656393.45000	656393.45000	899457.40056	0	0	0
cr, θ_2	352.11200000	not applicable	786633.25125	213332.68034	786633.25125	0	0	0
cr, θ_3	138.85000000	not applicable	100101.57003	59836.108884	59836.108840	0	0	0
$base$	11.914791200	0	9828.9217313	8048.7220165	2999.4764105	0	0	0

TABLE I: Numerical values for the constrained spatial pantograph linkage used in the ADAMS simulation, the masses of links 5 through 8 were set to zero in order to neglect them

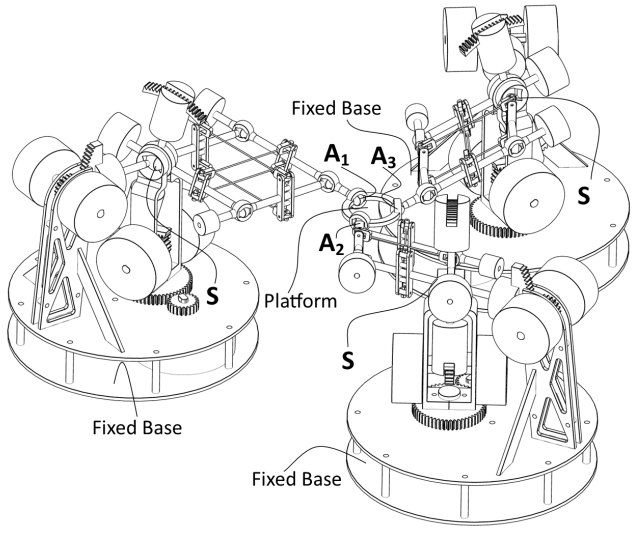

Fig. 14: CAD model of the 6 DoF dynamically balanced manipulator using 3 DoF dynamically balanced constrained spatial pantograph linkages as its legs. This manipulator uses 12 counter-masses and 6 counter-rotations to satisfy the balance conditions.

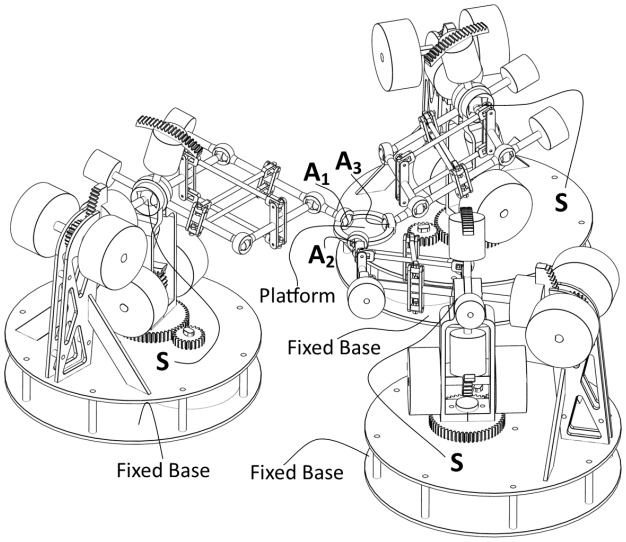

Fig. 15: CAD model of the alternative 6 DoF dynamically balanced manipulator using dynamically balanced constrained spatial pantographs with only 3 counter masses as its legs. This manipulator uses 9 counter-masses and 9 counter-rotations to satisfy the balance conditions.

as described by Gosselin et al. (2004) to replace the platform with three point masses. To ensure that the three point masses are dynamically equivalent to the platform, three conditions must be satisfied with the variables from Figure 16:

$$m_p = m_{A,1} + m_{A,2} + m_{A,3} \tag{55}$$

$$m_p \mathbf{P} = m_{A,1}\mathbf{A}_1 + m_{A,2}\mathbf{A}_2 + m_{A,3}\mathbf{A}_3 \tag{56}$$

$$\mathbf{I}_p = \sum_{1}^{3} m_{A,i}[(\mathbf{A}_i \cdot \mathbf{A}_i)\mathbf{E}_3 - \mathbf{A}_i \otimes \mathbf{A}_i] \tag{57}$$

Condition 55 states that the total mass of the point masses should equal the total mass of the platform. In condition 56, the bold symbols are vectors defining the point in Figure 16, and the conditions imply that the CoM of the three point masses should be equal to the CoM of the platform. Condition 57 states that the inertia of the three point masses should equal the inertia of the platform, which is in practice the hardest condition to fulfil.

One way to satisfy the conditions is to model the platform to be infinitely thin such as in [6] and [5], but this is not a feasible solution if the manipulator has to be built. Another simple body that satisfies the inertia condition is a thin hoop, but the solution will not be perfect when joints are attached to this hoop. Because a perfect solution for the dynamic equivalence of a platform replaced with 3 point masses does not exist, it will be tried to approximate the inertia condition, thereby making the parallel manipulator approximately balanced instead of perfectly balanced. An example of a platform that approximates the balance conditions can be seen in Figure 16. The point masses could be included in point A of link 3 for each leg by $m'_3 = m_3 + m_{A,i}$ and $p'_3 = (m_3 p_3 + m_p(a_1 + a_3)/3)/m'_3$, and by using the parallel

axis theorem to obtain the new inertia tensor for link 3.

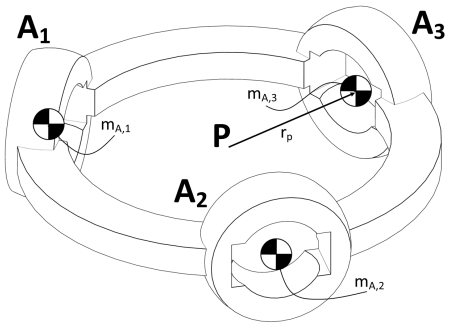

Fig. 16: CAD model of the platform for the 6 DoF parallel manipulator that approximates the conditions for point mass substitution

When the approximate balance by representing the platform with 3 point masses is insufficient, the platform should be represented by four point masses from which one is out-of-plane with the other masses [4]. This would also mean that a fourth arm is needed, which would increase the mass of the manipulator even more.

B. Reduction to a 6 DoF Force Balanced Manipulator

It is also possible to use the 3 DoF Force Balanced linkage (Figure 6) as legs for the 6 DoF mechanism. For this mechanism, the third condition for point mass substitution (regarding the inertia) does not apply. The approximate balance for the out-of-plane links does also not apply for a force-balanced linkage. Thereby, this mechanism is force balanced with only 6 counter-masses for a 6 DoF parallel manipulator. A CAD drawing of this linkage can be seen in Figure 17.

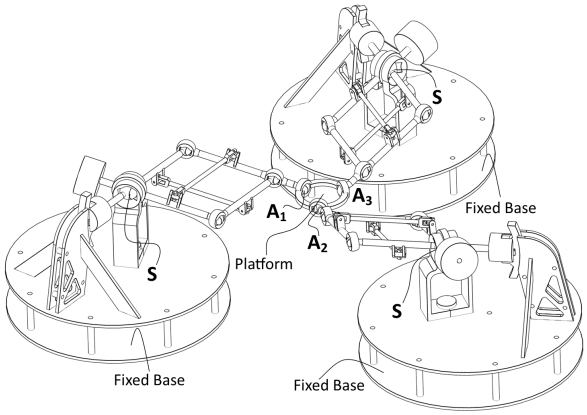

Fig. 17: CAD model of the 6 DoF force balanced manipulator using 3 DoF force balanced constrained spatial pantograph linkages as its legs

C. Workspace analysis

The workspace of the parallel linkage was described using the well-known constant-orientation workspace. In order to determine this workspace, the already known workspace for a single leg was used.

For each point of the workspace of a single leg, it was checked if, with the prescribed orientation of the platform, the other two attachment points of the platform are inside the workspaces of the other two legs. By repeating this procedure, a point cloud was obtained that shows the constant-orientation workspace for the 6 DoF dynamically balanced manipulator. This result can be seen in Figure 18. A contour of this workspace at $z = 0.24$ can be seen in Figure 19.

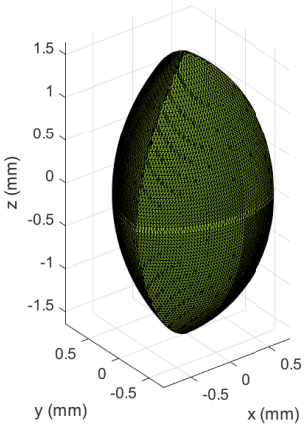

Fig. 18: Constant-Orientation workspace for the 6 DoF parallel constrained spatial pantograph linkage with link lengths of 80 mm

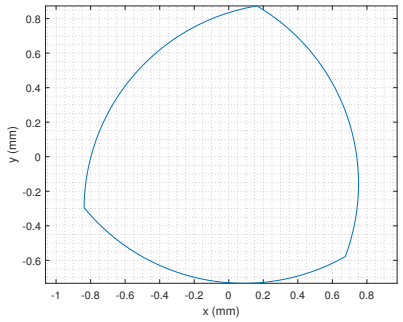

Fig. 19: Contour at $z = 0.24$ mm for the constant-orientation workspace for the 6 DoF parallel constrained spatial pantograph linkage with link lengths of 80 mm

D. Physical Demonstrator

A physical demonstrator for the dynamically balanced constrained spatial pantograph linkage, which can be seen in Figure 20, was built to show the kinematics and the feasibility of the proposed design. Because the goal of this demonstrator is to show the kinematics and not to have a fully operating robot, no actuators were attached. The demonstrator was built using 3D printing techniques, and the dimensions of the

countermasses, counter rotations, and the gears were chosen so that the manipulator would be balanced if it was fabricated with higher precision and solid materials.

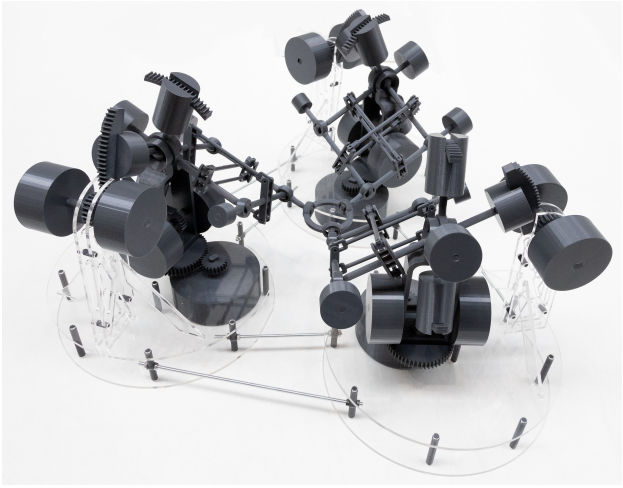

Fig. 20: The physical demonstrator for the 6 DoF force and moment balanced constrained spatial pantograph linkage that was built which shows that the proposed designs are feasible

VII. Discussion

As with other balanced manipulators in literature, force and moment balance of the spatial pantograph linkage came at the cost of substantial increases in mass and complexity due to the addition of counter masses and counter rotations. However, no optimization was executed in this article, so the total mass of the linkage could probably be reduced.

One possible way to reduce the mass addition is by wisely choosing the transmission ratios between the links and their counter-rotations. By choosing a higher gear ratio, the counter-rotation's inertia, and thereby its mass, could be reduced. However, this would lead to higher forces in the transmission, which could lead to a loss in precision and an increase in the backlash error.

Another way to optimize the mass addition of the linkage is by the use of counter-rotating-counter-masses (CRCM) as described in [14]. By doing this, the counter-rotation both takes the function of the counter-mass and counter-rotation. Another benefit is that the counter-rotation could be smaller because it does not have to compensate for the spin angular momentum of the counter-mass.

It should also be noted that although the linkage is said to be dynamically balanced, internal forces may exist in the base between the three legs. When some flexibility exists in the base, this could lead to inaccuracies and problems with the control of the manipulator. However, for this manipulator, the base is assumed to be rigid.

In the simulation, the out-of-plane links were assumed to be massless and with zero inertia. Because these links can be made lightweight compared to the other links, adding mass and inertia to these links would not heavily increase the dimensions of the countermasses and counter-rotations. Dimensioning of these links could be part of an optimization as described before in this discussion.

As mentioned in the previous section, the platform of the manipulator should fulfil certain conditions for the manipulator to be dynamically balanced. Therefore, it is not possible with the current design to have a variable payload. This was beyond the scope of this work but could be an exciting topic for future research.

VIII. Conclusion

This article presented force and moment balanced 3 DoF and 6 DoF manipulators based on the spatial pantograph linkage by Van der Wijk (2022). Three 3 DoF manipulators were presented: a force balanced 3 DoF manipulator using 2 counter masses, a dynamically balanced 3 DoF manipulator using 4 counter masses and 3 counter-rotations, and a dynamically balanced 3 DoF manipulator using 3 counter masses and 3 counter-rotations. For these 3 DoF manipulators, the singularities were determined, resulting in the manipulator's torus shaped workspace. The balance conditions were obtained using the conservation of linear and angular momentum, and these conditions were verified by a simulation using the dynamic simulation software ADAMS.

After calculation and verification of the balance conditions for the 3 DoF constrained spatial pantograph linkage, this knowledge was expanded to synthesize three spatial 6 DoF force and moment balanced manipulators. The force balanced 6 DoF manipulator is balanced using only 6 counter masses, the first dynamically balanced manipulator using 12 counter masses and 9 counter-rotations, and the second dynamically balanced manipulator using 9 counter masses and 9 counter-rotations. A physical demonstrator was built for the first DoF dynamically balanced manipulator to show the kinematics of this linkage. To the best of the author's knowledge, this was the first demonstrator for a 6 DoF dynamically balanced manipulator, which showed the feasibility of the proposed design.

References

[1] G. G. Lowen and R. S. Berkof, "Survey of investigations into the balancing of linkages," *Journal of Mechanisms*, vol. 3, no. 4, pp. 221–231, Dec. 1968.

[2] A. Suarez, A. E. Jimenez-Cano, V. M. Vega, G. Heredia, A. Rodriguez-Castaño, and A. Ollero, "Lightweight and human-size dual arm aerial manipulator," in *2017 International Conference on Unmanned Aircraft Systems (ICUAS)*, Jun. 2017, pp. 1778–1784.

[3] J. Fielding, "The Challenges of Making Giant Robots: Yaskawa MH900 - Jeremy Fielding Episode 108," Dec. 2022. [Online]. Available: https://www.youtube.com/watch?v=hMAvbu9OzwI

[4] Y. Wu and C. M. Gosselin, "Dynamic Balancing of Multi-Degree-of-Freedom Parallel Mechanisms With Multiple Legs," in *Volume 2: 28th Biennial Mechanisms*

and Robotics Conference, Parts A and B, Salt Lake City, Utah, USA, Sep. 2004, pp. 1293–1301.

[5] ——, "Design of reactionless 3-DOF and 6-DOF parallel manipulators using parallelepiped mechanisms," *IEEE Transactions on Robotics*, vol. 21, no. 5, pp. 821–833, Oct. 2005.

[6] ——, "Synthesis of Reactionless Spatial 3-DoF and 6-DoF Mechanisms without Separate Counter-Rotations," *The International Journal of Robotics Research*, vol. 23, no. 6, pp. 625–642, Jun. 2004.

[7] S. Briot and V. Arakelian, "Complete Shaking Force and Shaking Moment Balancing of the Position-Orientation Decoupled PAMINSA Manipulator," in *2009 IEEE/ASME International Conference on Advanced Intelligent Mechatronics*, Singapore, Jul. 2009, pp. 1521–1526.

[8] V. van der Wijk, "The Spatial Pantograph and its Mass Balance," in *Springer Proceedings in Advanced Robotics*, ser. Springer Proceedings in Advanced Robotics, O. Altuzarra and A. Kecskeméthy, Eds., vol. 24. Springer Science+Business Media", 2022, pp. 426–433.

[9] D. Chablat and P. Wenger, "Working Modes and Aspects in Fully-Parallel Manipulators," in *IEEE International Conference on Robotics and Automation*, vol. 3, Leuven, Belgium, 1998, pp. 1964–1969.

[10] C. Gosselin and J. Angeles, "Singularity analysis of closed-loop kinematic chains," *IEEE Transactions on Robotics and Automation*, vol. 6, no. 3, pp. 281–290, Jun. 1990.

[11] A. Hijazi, J.-F. Brethe, and D. Lefebvre, "Singularity Loci and Kinematic Induced Constraints for an XY-Theta Platform Designed for High Precision Positioning:," in *Proceedings of the 15th International Conference on Informatics in Control, Automation and Robotics*. Porto, Portugal: SCITEPRESS - Science and Technology Publications, 2018, pp. 39–48.

[12] S. Foucault and C. M. Gosselin, "Synthesis, Design, and Prototyping of a Planar Three Degree-of-Freedom Reactionless Parallel Mechanism," *ASME Journal of Mechanical Design*, vol. 126, no. 6, pp. 992–999, Feb. 2005.

[13] C. Gosselin, F. Vollmer, G. Cote, and Y. Wu, "Synthesis and design of reactionless three-degree-of-freedom parallel mechanisms," *IEEE Transactions on Robotics and Automation*, vol. 20, no. 2, pp. 191–199, Apr. 2004.

[14] J. L. Herder and C. M. Gosselin, "A Counter-Rotary Counterweight (CRCW) for Light-Weight Dynamic Balancing," in *DETC2004: proceedings of the ASME 2004 design engineering technical conferences and computers and information in engineering conference*, vol. 2. Salt Lake City, Utah, USA: ASME, 2004, pp. 1–9.

Chapter 4

Discussion

Discussion

In chapter 2 of this thesis, a literature research was performed on the state-of-the-art for 6 DoF spatially dynamically balanced manipulators, focussing on their potential use in aerial manipulation. The methods for determining force and moment balance conditions were discussed, and design constraints were set for aerial manipulators. It followed that only three designs of 6 DoF spatially dynamically balanced manipulators existed: the compound four-bar [10], the parallelepiped [9], and the PAMINSA manipulator [11].

The compound four-bar manipulator consists of multiple inverted four-bar linkages stacked in series. These individual four-bar linkages are moment balanced without counter-rotations and have a constant inertia for in-plane rotation. Therefore, they act as a rigid body for planar translation and rotation. When placing a copy of this linkage at a 90 degrees offset from the original linkage, a linkage is obtained which has a constant inertia tensor and therefore acts as a rigid body for spatial motion. Two planar linkages are stacked to one spatial linkage, resulting in a 3 DoF spatially dynamically balanced linkage. Three of these 3 DoF arms are then used to obtain a 6 DoF spatially dynamically balanced manipulator without any counter-rotations.

The parallelepiped linkage was also designed by Wu and Gosselin. This linkage uses a planar pantograph as its base, which is balanced using 3 counter masses and 2 counter-rotations. Perpendicular to this pantograph, another parallelogram structure was added, resulting in a 3 DoF linkage. This linkage is balanced using 5 counter masses and 3 counter-rotations. When using three of these 3 DoF linkages as legs, similar to the compound four-bar linkage described above, a 6 DoF spatially dynamically balanced manipulator was synthesized which is balanced using 15 counter masses and 9 counter-rotations.

The last existing spatially balanced manipulator was the PAMINSA manipulator by Briot and Arakelian (2009). In this manipulator, the horizontal and vertical motions were decoupled with the idea of decoupling the direction in which gravitational work is done. However, when this manipulator is force balanced, this does not hold, as the CoM of the manipulator is constant and thus does not do any work. The manipulator is force balanced using counter masses, and moment balance is achieved using a 3 DoF serial wrist attached as the end-effector. Because this serial wrist is used for active moment balancing of the linkage, it is effectively just a 3 DoF spatial linkage. Therefore this linkage will not be taken into account further in this discussion.

In chapter 3 of this thesis, novel 3 DoF and 6 DoF spatially force and moment balanced linkages, based on the spatial pantograph linkage, were introduced. The general spatial pantograph linkage, as presented by Van der Wijk (2022), was firstly constrained such that it reduces from 6 DoF to a 3 DoF linkage. For the 3 DoF linkage, the forward and inverse kinematics were solved, and the manipulator's workspace was obtained by calculating its singularities. Afterwards, the force and moment balance conditions for this linkage were calculated and verified using ADAMS. This knowledge was extended to synthesize 6 DoF force and moment balanced linkages. Compared to the state-of-the-art, these linkages use fewer moving links, fewer counter masses, and the used counter masses are closer to the base of the linkage.

This discussion will elaborate further on some important points concerning spatial dynamic balance, and recommendations for future research.

Leg-to-leg approach

The method of using balanced 3 DoF linkages as legs to synthesize 6 DoF dynamically balanced manipulators is often referred to as the leg-by-leg approach. This method was used in synthesizing all the 6 DoF balanced linkages described above.

One downside of this method is the complexity of including the platform, which is done using the *equivalent mass method*. This method substitutes the platform with three point-masses which have: 1. the same total mass as the platform, 2. the same CoM as the platform, and 3. the same inertia as the platform. When the platform meets these conditions, the point-masses could be added to the end-effector points of the legs. However, it has yet to be possible to have a non-planar platform that fulfils all these conditions. As stated by Wu (2003), a solution might be to use four point-masses instead of three, but this would require an additional leg and thereby additional mass.

A benefit of this method is that the balancing problem is divided into smaller problems, being the separate 3 DoF leg linkages. Using the *Chebychev-Grübler-Kutbach criterion* for spatial mechanisms, it could be calculated that the addition of a platform (6 DoF) which is connected using 3 spherical joints (3 DoF each), leads to an addition of -3 DoF to the manipulator. In order to obtain a 6 DoF manipulator, the legs should together have 9 DoF. Therefore, manipulators that are synthesized using a leg-by-leg approach will always have more internal DoFs than DoFs at the end-effector.

Having more internal DoFs than DoFs at the end-effector might not seem to be a problem at first sight, but the balancing of each DoF generally leads to an addition mass to the manipulator. Therefore, having more internal DoFs will generally increase the total mass of the linkage. Finding solutions that do not need a leg-by-leg approach might, if even possible, lead to more lightweight balanced manipulators.

Minimization of the number of counter masses

There are two important factors regarding the manipulator's performance when adding counter masses: 1. the number of counter masses should be minimized, and 2. the counter masses should be as close to the base as possible. It is evident that a lower number of counter masses reduces the total weight of the manipulator. Having counter masses at distal links leads to a significant increase in the moment of inertia of the link, and this mass generally has to be balanced by other counter masses at the base. For balanced linkages stacked in series, such as the compound four-bar linkage, balancing of counter masses also occurs, which further increases the mass of the linkage. Therefore, it is preferable to balance parallel linkages such as the parallelepiped or the constrained spatial pantograph.

Comparing the dynamically balanced constrained spatial pantograph linkage with the parallelepiped linkage regarding the addition of counter masses, it can be seen that the first one uses 3 counter masses of which 2 are located at the base, and the other one uses 5 counter masses of which 3 are located at the base. This difference could be attributed to two factors regarding the kinematics of the linkage.

In the parallelepiped linkage, all links are connected using revolute joints; therefore, all links have 1 DoF motion. In the 3 DoF constrained spatial pantograph linkage, there is also one link that has 2 DoF motion capability. By having one link that moves with 2 DoF, both DoFs could be balanced by just 1 counter mass, explaining one counter mass difference.

The special kinematics of the constrained spatial pantograph linkage could explain to other difference in number of counter masses. During its motion, all links (except for the out-of-plane links) stay in a single plane. Therefore, it is possible to use only 3 counter-masses for moment balance, as also explained in [13] for the planar pantograph linkage. This simplification is impossible for the parallelepiped linkage as its links move in different planes.

Minimization of the number of counter-rotations

As it is possible to use one counter mass for 2 DoF motion, one might also think to reduce the number of counter-rotations is a similar fashion. However, there is one big difference between force and moment balance. For force balance, the CoM of the total linkage has to remain constant during motion, which only concerns a point in space. This allows one counter mass to balance 2 DoF motion; it can rotate with the link in all directions while keeping the CoM of the link with the counter mass constant. As in the general spatial pantograph [12], this is also possible for a 3 DoF link.

Moment balance does not only concern a point but also a rotation axis. The rotation axes of the link and the counter-rotation always have to be parallel to balance the link. When these axes are not parallel, angular momentum will arise around other axes, or additional counter-rotations have to be used to cancel this momentum. Due to the, in general, different inertia values around the principal axes of a link, the order of rotations is also of importance.

One special case in which it is possible to moment balance a 3 DoF link with one counter rotation is when the link has equal inertia in all its principal axes. When this is the case, the counter rotation could be a sphere, and the order of rotations would not matter, as the inertia around all principal axes is equal. However, for the general case, it is assumed that it is not possible have a lower number of counter-rotations than rotational DoFs.

The compound four-bar linkage is an example of a linkage that is dynamically balanced without any counter-rotations. However, the four-bar linkage has only 1 DoF motion capability, but three moving links. This linkage could therefore also be seen as a 1 DoF link with a counter linkage attached to it to compensate for the generated angular moment, essentially taking the function of a counter-rotation.

Practical implementation

Although the manipulators presented in chapter 3 of this thesis improve the state-of-the-art in terms of their number of counter-masses, the position of the counter masses, and the number of moving links, the practical applications of such manipulators are still questionable. For high-demanding tasks in which reaction forces and moments should be as low as possible, 6 DoF balanced manipulators could come into use. However, for most tasks, balancing will probably add too much mass and complexity to the system.

In aerial manipulation, the reduction of the mass of the manipulator is crucial due to the payload limitation of the aerial vehicle. Therefore, the constrained spatial pantograph linkage is a step forward, as it uses fewer counter-masses than the state-of-the-art and could thereby be lighter. However, a lot of mass was still added to satisfy the balance conditions. Therefore, the proposed manipulator will also not be well suited for aerial manipulation.

Although the 6 DoF dynamically balanced manipulator is very complex, reduced versions of this manipulator could find their way to practical applications. For some of the examples presented in the introduction of this thesis, like the balancing of stage lights [6] or cameras attached to cable robots [7], the manipulators only move with 2 DoF. This motion is similar to the 2 DoF link of the constrained spatial pantograph linkage. Thus, knowledge from this thesis could be used to synthesize balanced solutions for these applications.

There may also be cases for which only force balance is sufficient. For such tasks, the 6 DoF force balanced constrained spatial pantograph could be of good use, as it is force balanced using only 6 counter masses. Other applications may lie in the reducing reaction forces and moments in cases for which they do not necessarily have to be zero.

Recommendations for future work

The results in this thesis show improvements in the state-of-the-art on spatial dynamic balance, but there are still some improvements possible in this research area.

In the current ADAMS simulation, which was used to verify the balance conditions, it was not possible to include the mass and inertia of the out-of-plane links, as the software did not allow for overconstraints. Although the author is confident that the conditions presented in this thesis are correct, it would be good to simulate the manipulator, including all the out-of-plane links. A further improvement in this direction is to simulate the 6 DoF linkage to see the result of the roll rotations of the out-of-plane links and the approximation made in the inclusion of the platform.

There are also some improvements that could be made in the design of the constrained spatial pantograph linkage. These could be improvements such as combining the functions of the counter masses and counter-rotations presented by Herder and Gosselin (2004), or performing an optimization of the mass and length parameters of the linkage. Other improvements could be in the design of the joints to increase the workspace of the manipulator. The improved design could then be fabricated with high precision such that tests could be performed.

Lastly, control of the constrained spatial pantograph linkage could be an exciting research topic. Due to its spatial motion and the coupling of the three arms to the platform, controlling this linkage to perform specified trajectories would be a great challenge.

Chapter 5

Conclusion

Conclusion

In chapter 2 of this thesis, it was found that only three designs for spatial 6 DoF dynamically balanced manipulators exist: the parallelepiped [9], the compound four-bar [10] and the PAMINSA [11]. Another promising design is the spatial pantograph linkage [12], as this linkage has 6 DoF motion capability and is force balanced using only 2 counter masses. These linkages were compared concerning their potential use in aerial manipulation, from which it was concluded that none of them was useable yet for aerial manipulation as the balancing led to a significant increase in mass and complexity of the manipulators.

In chapter 3, a systematic study on novel 3 DoF and 6 DoF force and moment balanced manipulators was conducted. This study started with constraining the general spatial pantograph from 6 DoF to 3 DoF, so that it could be used as a leg for a parallel 6 DoF manipulator. For the 3 DoF linkages, the forward and inverse kinematics were obtained next to the singularities, resulting in the manipulator's torus-shaped workspace. The force and moment balance conditions were obtained using the conservation of linear and angular momentum and were verified using the dynamic simulation software ADAMS. Three possible designs that fulfil the balance conditions were presented: (1) a force balanced 3 DoF manipulator that is balanced by 2 counter masses, (2) a dynamically balanced 3 DoF manipulator that is balanced by 4 counter masses and 3 counter-rotations, and (3) a dynamically balanced 3 DoF manipulator that is balanced by 3 counter masses and 3 counter-rotations. Each of the 3 DoF linkages was used to synthesize a 6 DoF parallel manipulator resulting in three other designs: (4) a force balanced 6 DoF manipulator which is balanced by 6 counter masses, (5) a dynamically balanced 6 DoF manipulator which is balanced by 12 counter masses and 9 counter-rotations, and (6) a dynamically balanced 6 DoF manipulator which is balanced by 9 counter masses and 9 counter-rotations. For the first dynamically balanced 6 DoF manipulator, a demonstrator was made, which showed the feasibility of the proposed design.

With the novel manipulators presented in this thesis, improvements are made regarding the state-of-the-art in the number of moving links, the number of counter masses, and by keeping counter masses close to the base of the linkage. Additionally, new knowledge is presented regarding the balancing of 2 DoF links. This thesis was the first to build a physical demonstrator of a 6 DoF balanced linkage to show its feasibility and provide inside into the motion of such linkages.

Before dynamically balanced linkages, as presented in this thesis, could be used in practical situations, a lot of optimization is needed. This might be in optimizing mass and length parameters, but also in reducing the added mass by combining the counter mass and the counter-rotation as in [14]. Concerning aerial manipulation, there is still a long way to go as the designs presented in this thesis still add too much mass and complexity. However, more short-term applications might be better off by using knowledge from this thesis to make lower DoF robotics, such as the passive balancing for 2 DoF links, or robotics that are only force balanced.

Bibliography

[1] G. G. Lowen and R. S. Berkof, "Survey of investigations into the balancing of linkages," *Journal of Mechanisms*, vol. 3, no. 4, pp. 221–231, Dec. 1968.

[2] A. Suarez, A. E. Jimenez-Cano, V. M. Vega, G. Heredia, A. Rodriguez-Castaño, and A. Ollero, "Lightweight and human-size dual arm aerial manipulator," in *2017 International Conference on Unmanned Aircraft Systems (ICUAS)*, Jun. 2017, pp. 1778–1784.

[3] J. Fielding, "The Challenges of Making Giant Robots: Yaskawa MH900 - Jeremy Fielding Episode 108," Dec. 2022. [Online]. Available: https://www.youtube.com/watch?v=hMAvbu9OzwI

[4] V. van der Wijk, "TOWARDS LOW MASS AND LOW INERTIA DYNAMIC BALANCING OF MECHANISMS," Master's thesis, Delft University of Technology, Delft, 2008.

[5] A. Davis, T. Kicera, and M. Hales, "Motion control system and motion control process," US Patent US20 120 051 879A1, Mar., 2012. [Online]. Available: https://patents.google.com/patent/US20120051879/en?oq=royal+shakespeare+company

[6] V. Herbert, "An oscillation damping system," GB Patent GB2 483 443A, Mar., 2012. [Online]. Available: https://patents.google.com/patent/GB2483443A/en?inventor=Vince+Herbert

[7] P. J. Bennett, G. Cook, M. R. Jones, K. Ashenayi, M. F. Henry, and A. MacDonald, "Aerial camera system," US Patent US9 964 836B2, May, 2018. [Online]. Available: https://patents.google.com/patent/US9964836B2/en?assignee=skycam&oq=skycam

[8] Y. Wu and C. M. Gosselin, "Dynamic Balancing of Multi-Degree-of-Freedom Parallel Mechanisms With Multiple Legs," in *Volume 2: 28th Biennial Mechanisms and Robotics Conference, Parts A and B*, Salt Lake City, Utah, USA, Sep. 2004, pp. 1293–1301.

[9] ——, "Design of reactionless 3-DOF and 6-DOF parallel manipulators using parallelepiped mechanisms," *IEEE Transactions on Robotics*, vol. 21, no. 5, pp. 821–833, Oct. 2005.

[10] ——, "Synthesis of Reactionless Spatial 3-DoF and 6-DoF Mechanisms without Separate Counter-Rotations," *The International Journal of Robotics Research*, vol. 23, no. 6, pp. 625–642, Jun. 2004.

[11] S. Briot and V. Arakelian, "Complete Shaking Force and Shaking Moment Balancing of the Position-Orientation Decoupled PAMINSA Manipulator," in *2009 IEEE/ASME International Conference on Advanced Intelligent Mechatronics*, Singapore, Jul. 2009, pp. 1521–1526.

[12] V. van der Wijk, "The Spatial Pantograph and its Mass Balance," in *Springer Proceedings in Advanced Robotics*, ser. Springer Proceedings in Advanced Robotics, O. Altuzarra and A. Kecskeméthy, Eds., vol. 24. Springer Science+Business Media", 2022, pp. 426–433.

[13] Y. Wu, "SYNTHESIS AND ANALYSIS OF REACTIONLESS SPATIAL PARALLEL MECHANISMS," PhD, Université Laval, Québec, 2003.

[14] J. L. Herder and C. M. Gosselin, "A Counter-Rotary Counterweight (CRCW) for Light-Weight Dynamic Balancing," in *DETC2004: proceedings of the ASME 2004 design engineering technical conferences and computers and information in engineering conference.* Salt Lake City, Utah, USA: ASME, 2004, pp. 1–9.

Appendices

Appendix A

Kinematic description of the spatial pantograph using quaternions and a comparison to the Euler method

Kinematic description of the constrained spatial pantograph linkage using quaternions and a comparison to the Euler method

1 Kinematic description using Quaternions

In order to check the kinematic description using Euler Angles, the same description was made using Quaternions. Quaternions are based on axis-angle rotations, which state that any rotation in three-dimensional space can be represented by a rotation about a fixed axis at a given angle [1]. With quaternions, the axis-angle parameters are described as a 4-dimensional vector with unit length in the following form:

$$q = \begin{pmatrix} q_0 \\ \mathbf{q} \end{pmatrix} \tag{1}$$

In which

$$q_0 = \cos(\frac{\theta}{2}), \qquad \mathbf{q} = \begin{pmatrix} q_1 \\ q_2 \\ q_3 \end{pmatrix} = \sin(\frac{\theta}{2})\mathbf{u} \tag{2}$$

Because the spatial pantograph has 6 DoF, two quaternions are needed to describe its configuration. Just like with the Euler Angles description, the quaternion for link 3 is equal to the quaternion for link 1, and the quaternion for link 4 is equal to the one for link 2 because they move parallel.

2 Comparison between the Euler angles and the Quaternion approach

The method using Euler Angles is more intuitive compared to the one using Quaternions. With Euler angles, it is easy to visualize how the links are moving, whilst this is all done in maths using the quaternion approach. Results from both methods with equal input angles are plotted in Figure 1 and give the same results. The results were also checked with a SolidWorks model and can therefore be assumed to be correct.

With both methods, it was impossible to find eccentric Centre of Mass positions for the out-of-plane links. This is due to the dependency of all input angles on the roll angle of each out-of-plane link which will also be shown in another appendix. However, it was already shown by van der Wijk (2022) that the force balance conditions do not allow for eccentric CoM positions of the out-of-plane links. Therefore, the on-axis CoM position calculation satisfies.

References

[1] H. Vallery and A. L. Schwab, *Advanced Dynamics*. Delft: Stichting Newton-Euler, Aug. 2020, vol. 3.

[2] V. van der Wijk, "The Spatial Pantograph and its Mass Balance," in *Springer Proceedings in Advanced Robotics*, vol. 24, 2022.

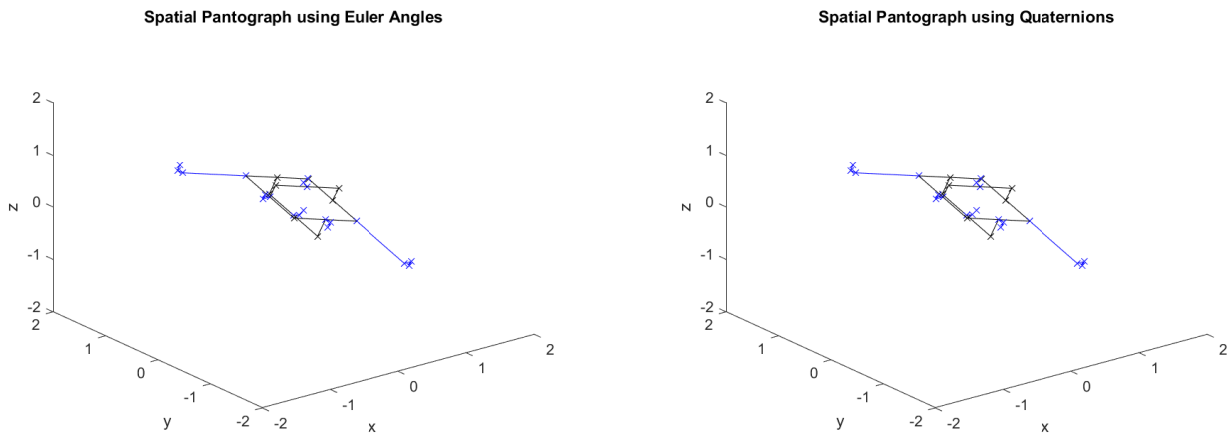

Figure 1: Visualization of the spatial pantograph using Euler Angles and Quaternions respectively

Appendix B

Solution for the inverse kinematics using a Gauss-Newton optimization process and a comparison to the geometric method

Solution for the inverse kinematics using a Gauss-Newton optimization process and a comparison to the geometric method

A widely used method for solving the inverse kinematics of a linkage is to use optimization. In this method, a constraint equation is formulated which should equal zero for all valid solutions. An optimization process is then used to minimize the value of the constraint equations up to a specified tolerance to solve the inverse kinematics. In this appendix, a Gauss-Newton process is used as the optimization process.

1 Linearized Gauss-Newton Process

In the process of finding a solution to the inverse kinematics problem with a linearized Guass-Newton process, we start with defining a constraint-vector $\mathbf{C}$ that equals zero when all the constraints are fulfilled. This vector is the difference between the position for point A with the current input variables and the wanted position for point A;

$$\mathbf{C} = \mathbf{p}_A - \mathbf{s} = \begin{pmatrix} (a_1 + a_3)\,\cos(\theta_1)\,\cos(\theta_2) & -s_x \\ (a_1 + a_3)\,\sin(\theta_1)\,cos(\theta_2) + a_2\,\cos(\theta_3) & -s_y \\ -(a_1 + a_3)\,\sin(\theta_2) + a_2\,\sin(\theta_3) & -s_z \end{pmatrix} = \mathbf{0} \tag{1}$$

With the equation $\mathbf{C} = \mathbf{0}$, a constraint surface can be drawn on which the solution must be in order to be a valid solution. There are infinitely many ways to reach the constraint surface from a given point, but it is proposed to use the direction in which the distance to the constraint surface is minimal. This could be mathematically written down as a *non-linear constrained least-square problem* [1].

The Gauss-Newton method is an iterative method for solving non-linear constrained least-squares problems as described above [1]. In this method, a vector $\mathbf{q}$ is used to describe the nearest set of input angles that fulfil the constraints, $\bar{\mathbf{q}}$ as the current set of input angles and $\Delta\mathbf{q}$ as the distance between these two points. The relation between these points could be written as follows;

$$\mathbf{q} = \bar{\mathbf{q}} + \Delta\mathbf{q} \tag{2}$$

We can fill in this expression into the constraint expression leading to;

$$\mathbf{C}(\mathbf{q}) = \mathbf{C}(\bar{\mathbf{q}} + \Delta\mathbf{q}) = \mathbf{C}(\bar{\mathbf{q}}) + \mathbf{C}_{,\mathbf{q}}\,\Delta\mathbf{q} = \mathbf{0} \tag{3}$$

in which $\mathbf{C}_{,\mathbf{q}}$ represents the jacobian of the constraint vector.

We want the vector $\Delta\mathbf{q}$ in the direction in which the gradient of the constraint vector is the greatest, because this represents the shortest distance to the constraint surface for a linear system. With this, we can write the following equation [1];

$$\begin{pmatrix} \mathbf{E} & \mathbf{C}_{,\mathbf{q}}^T \\ \mathbf{C}_{,\mathbf{q}} & \mathbf{0} \end{pmatrix} \begin{pmatrix} \Delta\mathbf{q} \\ \boldsymbol{\mu} \end{pmatrix} = \begin{pmatrix} \mathbf{0} \\ -\mathbf{C}(\bar{\mathbf{q}}) \end{pmatrix} \tag{4}$$

in which $\mathbf{C}(\bar{\mathbf{q}})$ is the error in fulfilling the constraints. Then, if the linearised constraints are independent, we can solve for $\Delta\mathbf{q}$;

$$\Delta\mathbf{q} = \mathbf{C}_{,\mathbf{q}}^T\,(\mathbf{C}_{,\mathbf{q}}\mathbf{C}_{,\mathbf{q}}^T)^{-1}\mathbf{C}(\bar{\mathbf{q}}) \tag{5}$$

The greatest part of this expression could be written as the *Moore-Penrose pseudo-inverse*, which gives the least square solution of the problem [1];

$$\mathbf{C}_{,\mathbf{q}}^{+} = \mathbf{C}_{,\mathbf{q}}^T\,(\mathbf{C}_{,\mathbf{q}}\mathbf{C}_{,\mathbf{q}}^T)^{-1} \tag{6}$$

2 Using the Gauss-Newton Process for the Non-Linear Constraint Problem

Because the Gauss-Newton method, as described above, minimizes the linearized problem, it will most of the time not reach the wanted position immediately with non-linear problems. Therefore, this process is iteratively repeated until the solution to the problem is found.

The search stops if either a set of input values is found that lies on the constraint surface or when the defined maximum number of iterations is exceeded. It is known that convergence to a feasible point is not guaranteed for the Gauss-Newton process. For some end-effector points of the manipulator it was observed that, although the point was inside the workspace, no solution was found and the algorithm converged to an infeasible point. In order to solve this problem, multiple initial guesses were used before a point was considered infeasible. These were later checked and shown to be equal to the results of the geometric method.

By discretization of the possible workspace, the workspace of the constrained spatial pantograph mechanism could be computed by checking if solutions exist for each point. This is done in Figure 1 for the domain $-80 \leq x \leq 80$, $-160 \leq y \leq 160$, $-160 \leq z \leq 160$ mm, and plotting a red dot whenever no inverse-kinematic solution exists and a black cross when there is a solution. In order to verify the results, the singularity surface that will be discussed later is plotted in the same figure. By refining the mesh of the test points, the workspace boundaries could be found. However, this process takes very long, will need a high resolution to obtain accurate solutions and needs a method to transfer the point cloud into a workspace boundary surface. Therefore, this method is not very well suited for obtaining the workspace boundaries.

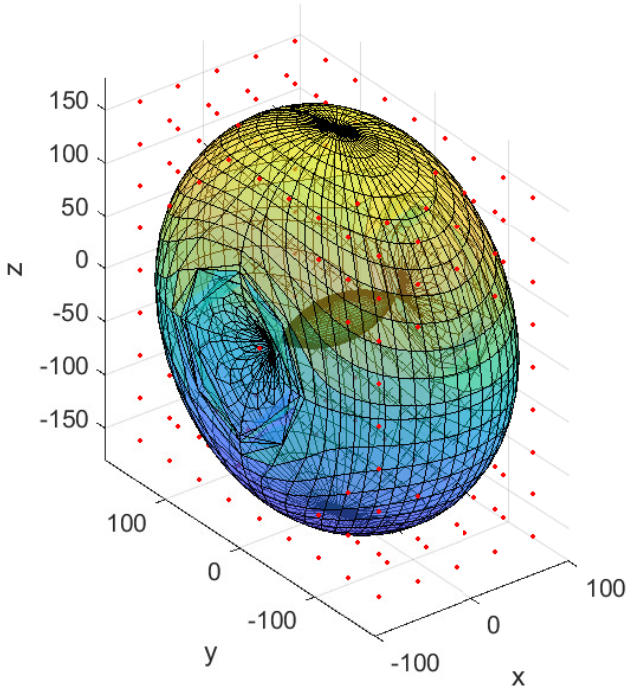

Figure 1: Basic workspace analysis using the Gauss-Newton inverse kinematics method

3 Comparison Between the Geometric and the Gauss-Newton Inverse Kinematic Solutions

After both methods for solving the inverse kinematics were defined, they will be compared. First of all, it needs to be stated that both methods result in proper solutions to the inverse kinematics. They reach the desired end-point, and both methods give equal results regarding the feasibility of certain solutions (results in the same workspace).

A remark that has to be made for both methods is that they do not necessarily result in practically feasible configurations. Some configurations will not be possible due to mechanical interference in the mechanism. With the Gauss-Newton method, this can be steered by providing different initial conditions, resulting in another solution for the desired point A. However, to do this properly, one should already have a rough understanding of the joint angles for the desired output position. With the geometric method, results can be steered by choosing another solution because the solutions for all working modes can easily be calculated. Therefore, an algorithm to find mechanically feasible configurations is easier to achieve using the geometric approach.

Another important aspect of each method is the time needed to find the inverse kinematic solution for a given point A. In order to compare this, both methods were programmed to find inverse kinematics solutions for the domain $-80 \leq x \leq 80$, $-160 \leq y \leq 160$, $-160 \leq z \leq 160$ mm with a step size of 40 mm in each direction, resulting in a point cloud with 405 equally spaced points. Both methods were tasked to determine if inverse kinematics solutions exist for all the points, and this was then timed. Both methods agreed with all the points on whether inverse kinematics solutions exist.

The Gauss-Newton method took 14.3 seconds to calculate solutions for all the points, resulting in 0.0354 seconds per point on average. The Geometric method took 0.0417 seconds to calculate inverse kinematics solutions for all the points, which equals an average of 0.1031 milliseconds per point. This means that the geometric is around 350 times faster than the Gauss-Newton method, and thereby is a more suitable candidate for finding inverse kinematics solutions.

Although the geometric method is faster and provides more insight into the mechanism, the main advantage of the Gauss-Newton method is that it is a more general method. For setting up the geometric method, a lot of insight is needed, which is often more complex than it seems. Next to that, specific kinematic equations need to be solved in order to obtain solutions. With the Gauss-Newton method, only the constraint vector containing the joint constraints of the mechanism is needed, which is easy to set up for each system. Thereby the Gauss-Newton method is easier to use.

References

[1] H. Vallery and A. L. Schwab, *Advanced Dynamics*. Delft: Stichting Newton-Euler, Aug. 2020, vol. 3.

Appendix C

Methods to calculate the workspace boundaries for the constrained spatial pantograph linkage

Methods to calculate the workspace boundaries for the constrained spatial pantograph linkage

Although a singularity analysis suffices to obtain the workspace boundary of the constrained spatial pantograph linkage, two other methods were used to calculate the workspace boundaries. These will be discussed in this appendix.

1 Discretization methods

A way to obtain the workspace of the constrained spatial pantograph is by discretization. This involves discretizing a domain in cartesian space and determining for each point if inverse kinematic solutions exist. The workspace boundaries can then be determined using interpolation. However, finding all valid points takes quite a lot of time, and it is hard to interpolate the points to plot the workspace boundaries. Additionally, this method only approximates the workspace and does not find exact solutions.

The advantage of this method is that no kinematic model has to exist for the manipulator, which is very useful for complex kinematic situations like in the 6 DoF parallel linkage with constrained spatial pantographs as legs. The inverse kinematics for each leg could be solved, but it is very hard or even impossible to find the inverse kinematic solution for the complete linkage. In such complex cases, discretization methods could be of great use.

2 Geometric method

Another method for determining the workspace is based on the geometric approach for the inverse kinematics. This method makes use of the two known points in the inverse kinematics problem: de base (point S), and the desired end-effector position (point A_{goal}). Around point S, a circle in the yz-plane is drawn, which shows all possible positions for point P_1 due to link 2. Around point A_{goal} a sphere is drawn, which defines all possible positions for P_1 due to link 3.

The geometric method searches for inverse kinematic solutions by finding intersection points between the black circle and the sphere, as shown in Figure 1. When $\mathbf{A}_{goal}$ is inside the workspace, there are always two intersection points between the circle and the sphere. On the workspace boundary, the sphere touches the yz-plane, resulting in only one intersection point. Outside the workspace, there are no intersection points because either the sphere does not intersect the yz-plane, or the slice of the sphere on the yz-plane is inside the circle. From this, it can be concluded that the boundary of the workspace is always at a distance $a_1 + a_3$ from the black circle in Fig. 1.

In Figure 2, the geometric method for obtaining the workspace is shown. The black circle represents the possible points P_1 due to the rotation of link 2, exactly as in Figure 1. The red circle represents the workspace boundaries for a plane perpendicular to the plane of the black circle. In this way, the workspace boundaries can be determined for each value of θ_3.

By rotating the red circle along the inertial x-axis, the total workspace of the manipulator could be obtained. This is shown in Figure 3. This workspace is equal to the workspace obtained using the singularity surface. However, calculations are faster, and a finer mesh could be chosen.

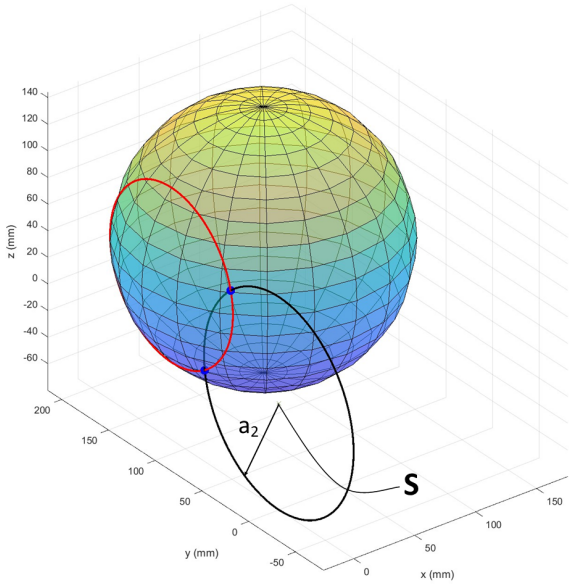

Figure 1: Geometric approach for the inverse kinematics in which the intersection between a circle and a sphere is calculated to solve the inverse kinematics

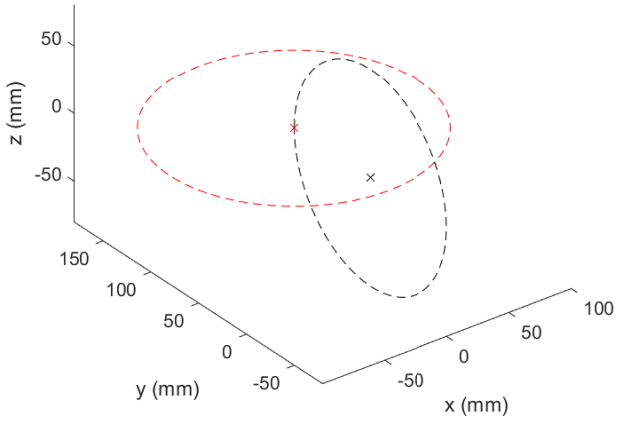

Figure 2: Schematic representing how the workspace can be drawn using the geometric method

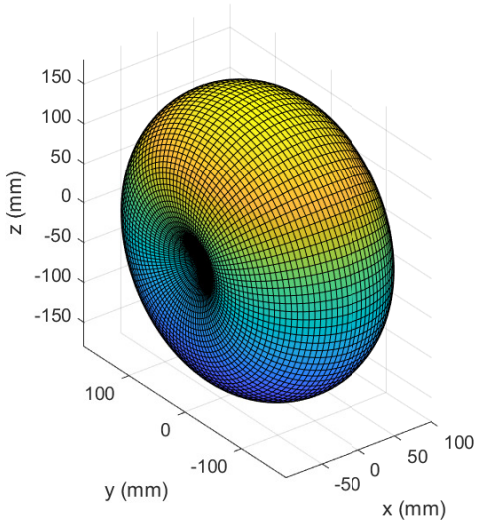

Figure 3: Workspace of the constrained spatial pantograph using the geometric method

Appendix D

Visualization of inverse kinematics solutions of the 3 DoF and 6 DoF constrained spatial pantograph linkage using MATLAB apps

Visualization of inverse kinematics solutions of the 3 DoF and 6 DoF constrained spatial pantograph linkage using MATLAB apps

In order to verify the inverse kinematics and the workspace analysis, apps were built in which the end effector point could be chosen, and a possible posture that reaches the end effector point is shown. Next to the verification purpose, these apps also give insight into how different points could be reached.

In this appendix, we will first discuss the app made for the 3 DoF constrained spatial pantograph linkage, after which the app for the 6 DoF linkage is discussed. Both apps were built using the MATLAB App Designer.

1 App concerning the 3 DoF linkage

The 3 DoF constrained spatial pantograph linkage has three input angles that can be controlled to reach a position with its end-effector point. Therefore, in this app, the translational position of the end-effector point could be set as an input. With this input position, a non-linear gauss-newton optimization is used to solve for a set of input angles, which is shown in the table in Figure 1. Furthermore, the calculated result is plotted with the goal position marked with a red circle. A screenshot of the app concerning the 3 DoF constrained spatial pantograph can be seen in Figure 1.

Lastly, it is also possible in this app to choose the configuration of the linkage, which changes the position of the counter-masses as described in the force balanced general spatial pantograph by van der Wijk (2022).

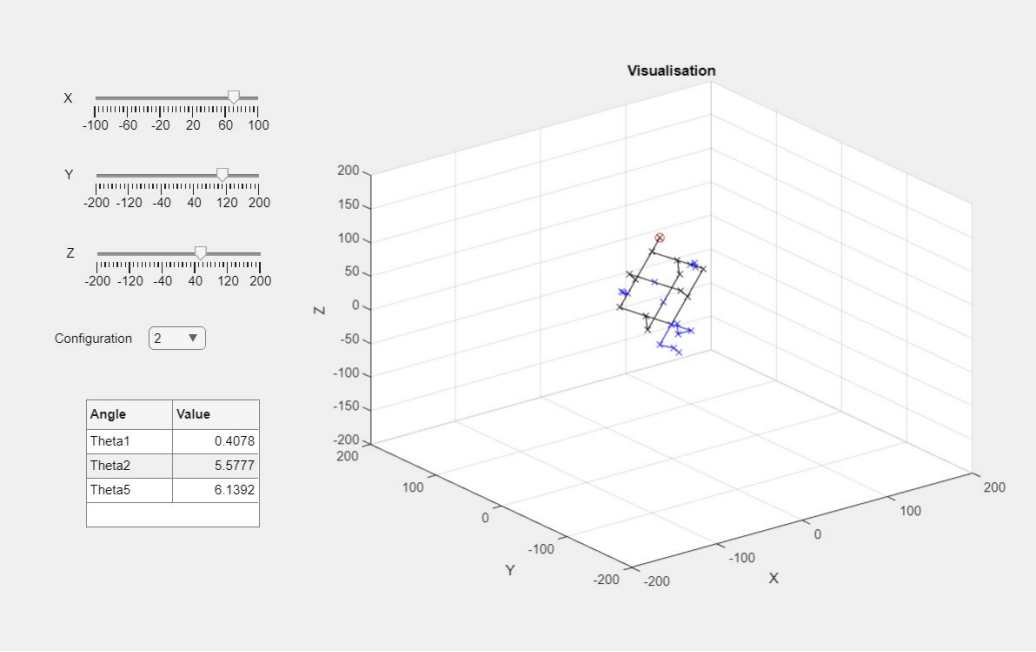

Figure 1: Screenshot of the app concerning the inverse kinematics of the 3 DoF constrained spatial pantograph linkage

2 App concerning the 6 DoF parallel manipulator

After the app for the 3 DoF linkage was built, this was extended for the 6 DoF linkage. A screenshot of this app can be seen in Figure 2. In this app, the following input parameters can be set by the user:

1. The position and orientation of the platform;
2. The radius of the platform;
3. The radius of the circle to which the base of each leg is attached, shown as a striped black circle in Figure 2;
4. The vertical rotation of the base of each platform, named Alpha1, Alpha2 and Alpha3.
5. The configuration of the legs, which changes the position of the counter-masses as described in [1].

In order to solve the inverse kinematics, we will start by taking the difference between the attachment point on the platform and the base for a leg. This vector is then rotated back with the rotation angle of the leg (Alpha) such that the problem becomes equal to the original inverse kinematic problem described in the paper. This problem is then solved using the geometric method. With this solution for the input angles, the linkage is rotated with the prescribed rotation of the leg and is plotted afterwards. This process was repeated for each leg.

When no inverse kinematic solution exists, the legs are not plotted, and there is a text shown on the plot that no solution exists.

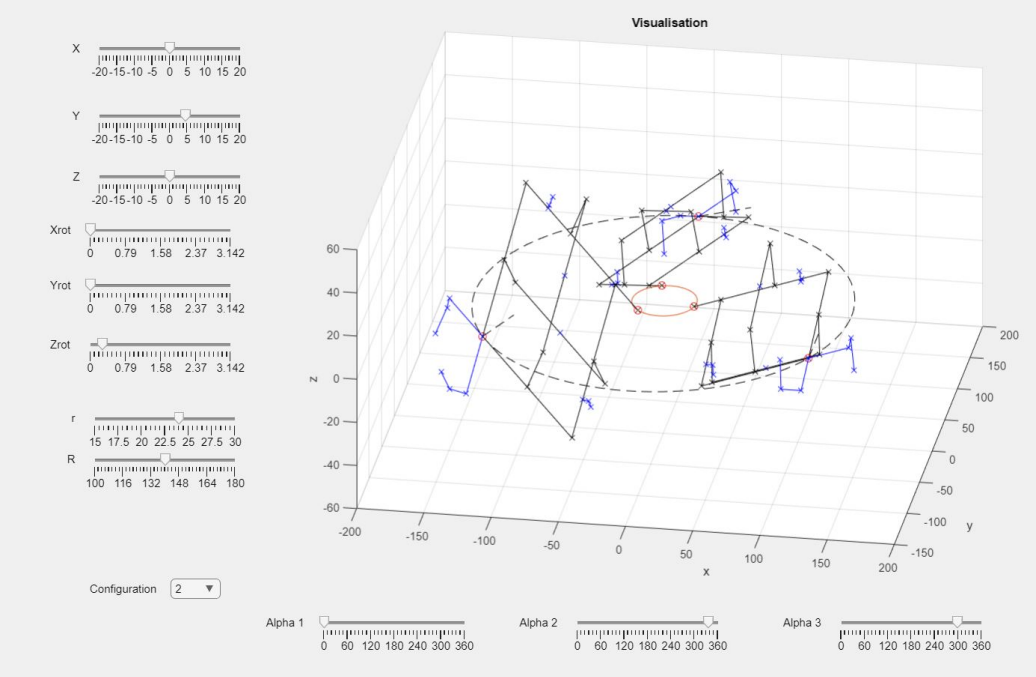

Figure 2: Screenshot of the app concerning the inverse kinematics of the 6 DoF parallel mechanism consisting of constrained spatial pantograph linkages

References

[1] V. van der Wijk, "The Spatial Pantograph and its Mass Balance," in *Springer Proceedings in Advanced Robotics*, ser. Springer Proceedings in Advanced Robotics, O. Altuzarra and A. Kecskeméthy, Eds., vol. 24. Springer Science+Business Media", 2022, pp. 426–433.

Appendix E

Non-linear relations between the rotations of the input links and the roll rotation of the out-of-plane links

Non-linear relations between the rotations of the input links and the roll rotation of the out-of-plane links

Linkages could be moment balanced actively, by using inertia wheels attached to actuators, or passively, by attaching an inertia wheel to one of the links using a transmission. In passive balance, the inertia wheel rotates in the opposite direction of the link to cancel the angular momentum generated by the mechanism. For practically feasible mechanisms, all links should have a linear relation with one of the input links. Otherwise, a complex transmission that exactly follows the mechanism's non-linearity is needed to balance the mechanism passively. In this appendix, the relation between the input links and the out-of-plane links is investigated.

As stated in the paper, it was not possible to calculate the orientation of the out-of-plane links with the Euler Angles or Quaternion approach. Therefore another method was found to calculate this orientation, which will be demonstrated for link 6 in this appendix.

Due to the way the universal joint is assembled, the body-fixed z-axis of link 6 should be perpendicular to the plane spanned by point P_1 and P_2. This direction can be found by taking the cross product:

$$\mathbf{z}_6 = \|\mathbf{P}_2 \times \mathbf{P}_1\| \tag{1}$$

Then, the body-fixed y-axis should be along the length-axis of the link, which can be calculated as follows:

$$\mathbf{y}_6 = \begin{pmatrix} 0 \\ cos(\theta_3) \\ sin(\theta_3) \end{pmatrix} \tag{2}$$

Lastly, we know that the x-axis should be perpendicular to both the z-axis and the y-axis so we can calculate the x-axis as:

$$\mathbf{x}_6 = \|\mathbf{y}_6 \times \mathbf{z}_6\| \tag{3}$$

Writing this out as a formula results in very complex equations, so it was chosen to just plot the relations between different input angles and the roll rotation of link 6. The base values for the input angles were:

$$\theta_1 = 45\,\text{deg} \tag{4}$$
$$\theta_2 = 10\,\text{deg} \tag{5}$$
$$\theta_3 = 22.5\,\text{deg} \tag{6}$$

For each plot, one of the angles was changing their value between 0 and 90 degrees. The results can be seen in Figures 1, 2 and 3. In these figures it is visible that all input angles influence the roll angle of link 6, and all these relations are non-linear. Therefore, passive moment balance is not possible for the current design of the linkage.

Several solutions may exist to overcome this problem. Probably choices for the joints in point P_1 and P_2 exist such that the out-of-plane links are no longer needed. A second possible solution may be to construct the out-of-plane links in such a way that the inertia around its length axis is negligible, such as with a slender rod. When the inertias around the other two axes are identical, it is possible to take the other two rotation axes into account, as shown in the paper. The disadvantage of this solution is that the constrained spatial pantograph linkage is only balanced approximately. However, having out-of-plane links is expected to increase the rigidity of the mechanism compared to the other solution described above which may be beneficial.

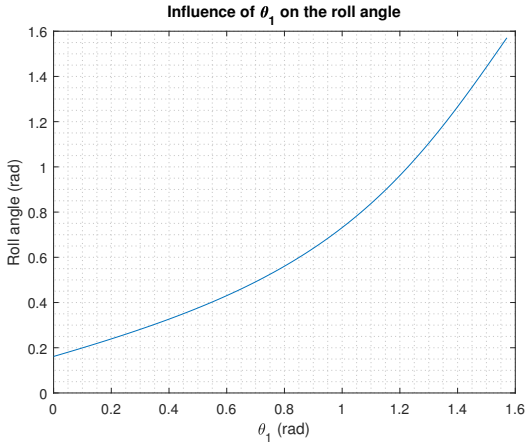

Figure 1: Influence of θ_1 on the roll angle of link 6

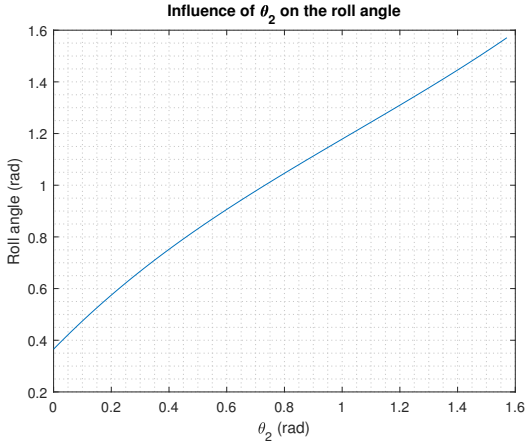

Figure 2: Influence of θ_2 on the roll angle of link 6

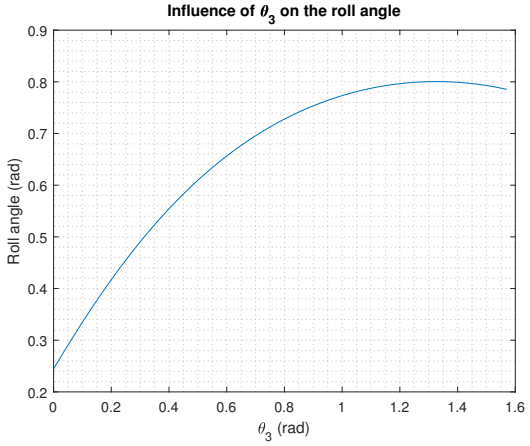

Figure 3: Influence of θ_5 on the roll angle of link 6

Appendix F

Detailed solution for the moment balance of the constrained spatial pantograph

Detailed solution for the Moment Balance of the Constrained Spatial Pantograph

1 Moment Balance

A linkage is said to be moment balanced when the linkage's total angular momentum is independent of the input angles and velocities. Angular momentum could be split up into two parts. Firstly the *orbital angular momentum*, which describes the angular momentum generated by moving the Centre of Mass (CoM) of a link along a circular trajectory. This value could be calculated by taking the cross product between the CoM position and the linear momentum of the link.

The second part of angular momentum is called *spin angular momentum*, which describes the angular momentum generated by rotating a link around its centre of mass.

2 Rotation matrices and angular velocity vectors

Before we start calculating the different angular momentum values, we first need to define some rotation tensors and vectors defining the direction of the angular velocity of the links.

Firstly, the rotation tensors for link 1 are defined. The rotation of link 1 is split up into a pitch motion around the body-fixed y-axis, and a yaw motion around the inertia z-axis:

$$\mathbf{R}_{yaw,1} = \begin{pmatrix} \cos(\theta_1) & -\sin(\theta_1) & 0 \\ \sin(\theta_1) & \cos(\theta_1) & 0 \\ 0 & 0 & 1 \end{pmatrix} \tag{1}$$

$$\mathbf{R}_{pitch,1} = \begin{pmatrix} \cos(\theta_2) & 0 & \sin(\theta_2) \\ 0 & 1 & 0 \\ -\sin(\theta_2) & 0 & \cos(\theta_2) \end{pmatrix} \tag{2}$$

Then, the angular velocities and their directions can be specified. The yaw-motion of link 1 is described using θ_1 and is directed along the inertial z-axis.

$$\boldsymbol{\omega}_1 = \begin{pmatrix} 0 \\ 0 \\ \dot{\theta}_1 \end{pmatrix} \tag{3}$$

The pitch motion of link 1 is around the body-fixed y-axis and is described using θ_2. The fact that this is a body-fixed vector is denoted by superscript $^{\mathcal{B}}$.

$${}^{\mathcal{B}}\boldsymbol{\omega}_2 = \begin{pmatrix} 0 \\ \dot{\theta}_2 \\ 0 \end{pmatrix} \tag{4}$$

Lastly, the pitch rotation of link 2 is around the inertial x-axis and described by θ_3.

$$\boldsymbol{\omega}_3 = \begin{pmatrix} \dot{\theta}_3 \\ 0 \\ 0 \end{pmatrix} \tag{5}$$

3 Angular Momentum of the Different Parts

With the rotation tensors and the angular velocity vectors described above, the angular momentum of the counter-inertia's could be written down. Due to the force-balance conditions, the counter-rotations should be either attached to the base or axisymmetric to it. Therefore, these counter-rotations do not have any orbital angular momentum.

$$\mathbf{L}_{\theta_1} = -\mathbf{I}_{\theta_1}\boldsymbol{\omega}_1 \tag{6}$$

$$\mathbf{L}_{\theta_2} = \mathbf{R}_{yaw,1}\mathbf{R}_{pitch,1}\mathbf{I}_{\theta_2}\mathbf{R}^T_{pitch,1}\mathbf{R}^T_{yaw,1}\boldsymbol{\omega}_1 - \mathbf{R}_{yaw,1}\mathbf{R}_{pitch,1}\mathbf{I}_{\theta_2}\boldsymbol{\omega}_2 \tag{7}$$

$$\mathbf{L}_{\theta_3} = -\mathbf{I}_{\theta_3}\boldsymbol{\omega}_3 \tag{8}$$

For each link, the CoM position $\mathbf{r}_i$ is calculated from which the linear momentum could easily be obtained using the following formula:

$$\mathbf{p}_i = m_i\dot{\mathbf{r}}_i \tag{9}$$

This linear momentum could be used to calculate the orbital angular momentum for each link:

$$\mathbf{L}_{orbit,i} = \mathbf{r}_i \times \mathbf{p}_i \tag{10}$$

The calculation of the spin angular momentum differs per link, because not every link has the same Degrees of Freedom (DoF). For link 1 and 3, the spin angular momentum could be calculated as follows:

$$\mathbf{L}_{spin,i} = \mathbf{R}_{yaw,1}\mathbf{R}_{pitch,1}\mathbf{I}_i\mathbf{R}^T_{pitch,1}\mathbf{R}^T_{yaw,1}\boldsymbol{\omega}_1 + \mathbf{R}_{yaw,1}\mathbf{R}_{pitch,1}\mathbf{I}_i\boldsymbol{\omega}_2 \tag{11}$$

For link 2 and 4, the spin angular momentum is calculated by:

$$\mathbf{L}_{spin,i} = \mathbf{I}_i\boldsymbol{\omega}_3 \tag{12}$$

4 Total Angular Momentum

By summing the angular momentum of all the links, the total angular momentum of the linkage could be obtained. In these calculations, all links are assumed to have concentric CoM positions. This is because it was observed that the linkage is not balanceable with non-concentric CoM positions, and adding the non-concentric terms decreases the readability of the equations.

The total angular momentum of the linkage could be written as:

$$\begin{aligned}
\mathbf{L}_x = {} & [A\sin(\theta_1)\sin(\theta_2) - C\sin(\theta_1)\cos(\theta_2) + L\cos(\theta_1)sin(\theta_2)sin(\theta_3) \\
& + G\cos(\theta_1)\sin(\theta_2)\cos(\theta_2) - F\cos(\theta_1)\cos(\theta_2)\sin(\theta_3) + 2(B+K)\cos(\theta_1)\cos(\theta_2)^2 \\
& + M\cos(\theta_1)\cos(\theta_2)\cos(\theta_3) - (B+K)\cos(\theta_1)]\dot{\theta}_1 \\
& + [F\sin(\theta_1)\sin(\theta_2)\sin(\theta_3) - M\sin(\theta_1)\sin(\theta_2)\cos(\theta_3) + L\sin(\theta_1)\cos(\theta_2)\sin(\theta_3) - H\sin(\theta_1) \\
& + C\cos(\theta_1)\sin(\theta_2) + A\cos(\theta_1)\cos(\theta_2) - F\cos(\theta_2)\cos(\theta_3) + L\cos(\theta_2)\cos(\theta_3) - M\cos(\theta_2)\sin(\theta_3)]\dot{\theta}_2 \\
& + [-L\sin(\theta_1)\sin(\theta_2)\cos(\theta_3) + M\sin(\theta_1)\cos(\theta_2)\sin(\theta_3) + L\cos(\theta_2)\sin(\theta_3) \\
& + F\sin(\theta_1)\cos(\theta_2)\cos(\theta_3) - F\sin(\theta_2)\sin(\theta_3) + M\sin(\theta_2)\cos(\theta_3) + I]\dot{\theta}_3
\end{aligned} \tag{13}$$

$$\begin{aligned}
\mathbf{L}_y = {} & [L\sin(\theta_1)\sin(\theta_2)\sin(\theta_3) + G\sin(\theta_1)\sin(\theta_2)\cos(\theta_2) - F\sin(\theta_1)\cos(\theta_2)\sin(\theta_3) \\
& + 2(B+K)\sin(\theta_1)\cos(\theta_2)^2 + M\sin(\theta_1)\cos(\theta_2)\cos(\theta_3) - (B+K)\sin(\theta_1) - A\cos(\theta_1)\sin(\theta_2) \\
& + C\cos(\theta_1)\cos(\theta_2)]\dot{\theta}_1 \\
& + [C\sin(\theta_1)\sin(\theta_2) + A\sin(\theta_1)\cos(\theta_2) - F\cos(\theta_1)\sin(\theta_2)\sin(\theta_3) + M\cos(\theta_1)\sin(\theta_2)\cos(\theta_3) \\
& + L\cos(\theta_1)\cos(\theta_2)\sin(\theta_3) + H\cos(\theta_1)]\dot{\theta}_2 \\
& + [L\cos(\theta_1)\sin(\theta_2)\cos(\theta_3) + M\cos(\theta_1)\cos(\theta_2) - F\cos(\theta_1)\cos(\theta_2)\cos(\theta_3) + D]\dot{\theta}_3
\end{aligned} \tag{14}$$

$$\begin{aligned}\mathbf{L}_z = [&-L\sin(\theta_1)\sin(\theta_2)\cos(\theta_3) + M\sin(\theta_1)\cos(\theta_2)\sin(\theta_3) + F\sin(\theta_1)\cos(\theta_2)\cos(\theta_3)\\ &-(B+K)\sin(2\theta_2) + G\cos(\theta_2)^2 + J]\dot{\theta}_1\\ [&M\cos(\theta_1)\sin(\theta_2)\sin(\theta_3) + F\cos(\theta_1)\sin(\theta_2)\cos(\theta_3) - A\sin(\theta_2) + L\cos(\theta_1)\cos(\theta_2)\cos(\theta_3)\\ &+C\cos(\theta_2)]\dot{\theta}_2\\ +[&L\cos(\theta_1)\sin(\theta_2)\sin(\theta_3) - F\cos(\theta_1)\cos(\theta_2)\sin(\theta_3) + M\cos(\theta_1)\cos(\theta_2)\cos(\theta_3) + E]\dot{\theta}_3\end{aligned} \tag{15}$$

In which

$$A = I_{xy,1} + I_{xy,3} \tag{16}$$
$$B = I_{xz,1} + I_{xz,3} \tag{17}$$
$$C = I_{yz,1} + I_{yz,3} \tag{18}$$
$$D = I_{xy,2} + I_{xy,4} \tag{19}$$
$$E = I_{xz,2} + I_{xz,4} \tag{20}$$
$$F = m_3p_3a_2 + m_4p_4a_1 + m_5p_5o_3 + m_6p_6o_1 + m_7p_7o_3 + m_8p_8o_1 \tag{21}$$
$$\begin{aligned}G = {} & I_{zz,1} - I_{xx,1} + m_1p_1^2 + I_{zz,3} - I_{xx,3} + m_3p_3^2 + m_4a_1^2 + m_5p_5^2 + m_6o_1^2 - m_6o_2^2 + m_7p_7^2\\ & + m_8o_1^2 - m_8o_5^2 + I_{zz,\theta_2} - I_{xx,\theta_2}\end{aligned} \tag{22}$$
$$H = I_{yy,1} + I_{yy,3} + m_1p_1^2 + m_3p_3^2 + m_4a_1^2 + m_5p_5^2 + m_6o_1^2 + m_6o_2^2 + m_7p_7^2 + m_8o_1^2 + m_8o_5^2 - I_{yy,\theta_2} \tag{23}$$
$$I = I_{xx,2} + I_{xx,4} + m_2p_2^2 + m_3a_2^2 + m_4p_4^2 + m_5o_3^2 + m_5o_4^2 + m_6p_6^2 + m_7o_3^2 + m_7o_6^2 + m_8p_8^2 - I_{xx,\theta_3} \tag{24}$$
$$J = I_{xx,1} + I_{xx,3} + I_{zz,\theta_2} + I_{zz,base} - I_{zz,\theta_1} \tag{25}$$
$$K = m_8o_1o_5 - m_6o_1o_2 \tag{26}$$
$$L = m_8p_8o_5 - m_6p_6o_2 \tag{27}$$
$$M = m_5p_5o_4 - m_7p_7o_6 \tag{28}$$

5 Moment Balance

In order to obtain a moment balanced linkage, the angular momentum of the linkage should be independent of the input angles and angular velocities. Therefore, the linkage is moment balanced when all terms (A through M) are equal to zero.

Appendix G

Simulation of a dynamically balanced 2 DoF joint using ADAMS

Simulation of a dynamically balanced 2 DoF joint using ADAMS

In the paper, the design conditions for a dynamically balanced 2 DoF joint were obtained. These state that the links should be symmetrical about all planes, and the inertia around the length axis and the other axis in the rotation plane have to be equal. Then, the angular momentum could be compensated for by two counter-rotations. The conditions are:

$$p_1 = 0 \tag{1}$$
$$I_{xx,1} = I_{zz,1} \tag{2}$$
$$I_{yy,\theta_2} = I_{yy,1} \tag{3}$$
$$I_{xx,\theta_2} = I_{zz,\theta_2} \tag{4}$$
$$I_{zz,\theta_1} = I_{zz,1} + I_{zz,\theta_2} \tag{5}$$

1 Computation of the variables

In order to satisfy the inertia conditions for the link, the equivalent inertia method was used. With this method, two masses which have the same values for I_{xx} and I_{zz} as the initial link are added (the red masses in Fig. 1). The conditions for zero products of inertia were satisfied by making the links symmetrical along the body-fixed xz-plane.

In order to compensate for the momentum generated by the pitch motion, two counter-inertia's were added to the frame (green parts in Fig. 1), such that its centre of mass lies on the z-axis. This is a necessary condition as the force balance conditions are not met otherwise.

The moment-balance for the yaw motion was performed using a single counter inertia at the base (cyan part in Fig. 1).

In this model, all parts are made of the same material and thus have the same inertia. The numerical values used in this simulation can be found in Table 1.

Link i	m_i (g)	$I_{xx,i}$ (g mm^2)	$I_{yy,i}$ (g mm^2)	$I_{zz,i}$ (g mm^2)
1	16.5005	9354.88	18050.1483	9354.88
cr, θ_1	102.1033	37258.2767	37258.2767	62538.309
cr, θ_2	57.7605	50183.9549	18050.1483	50183.9549
base	11.9148	9828.9217	8048.722	2999.4764

Table 1: Numerical values for the simulation of the dynamically balanced 2DoF joint

2 Simulation results

The 2 DoF link was tested using the dynamic simulation software ADAMS, of which a screenshot can be seen in Figure 1. In this simulation the following input torques in Nmm were used:

$$T_{\theta_1} = 10\,\cos(2\pi\,t) \tag{6}$$
$$T_{\theta_2} = \cos(2\pi\,t) \tag{7}$$

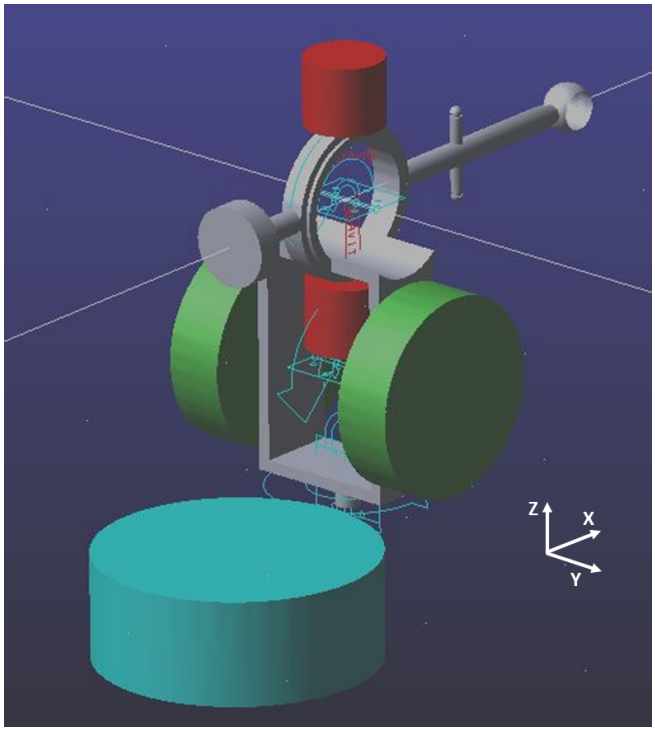

Figure 1: Screenshot of the ADAMS simulation for the 2 DoF dynamically balanced joint

The test results without counter-rotations can be seen in Figure 2. The results of the balanced test with counter-rotations can be seen in Figure 3.

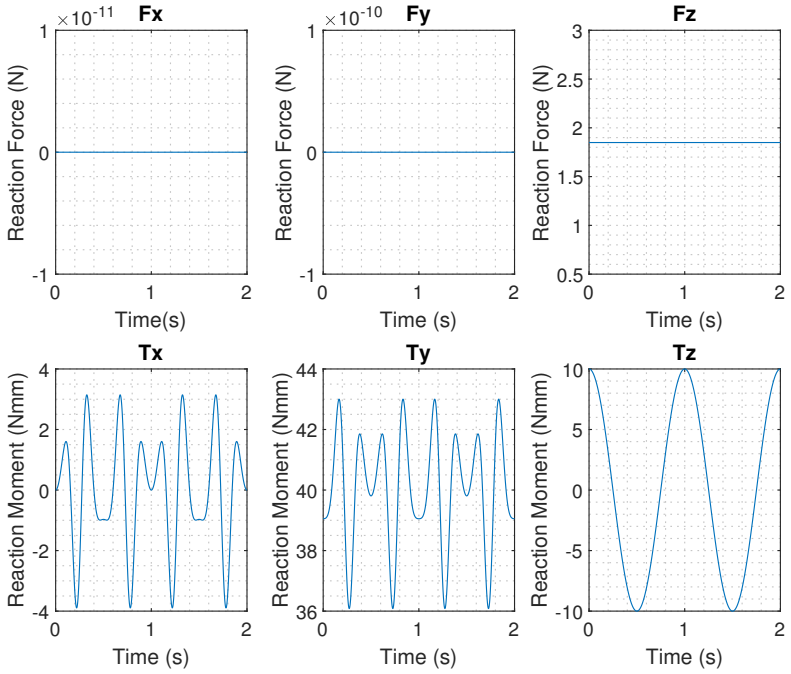

Figure 2: Reaction forces and moments for the unbalanced case with $\theta_1 = 30\,sin(2\pi\,t)$ and $\theta_2 = 50\,sin(2\pi\,t)$ degrees

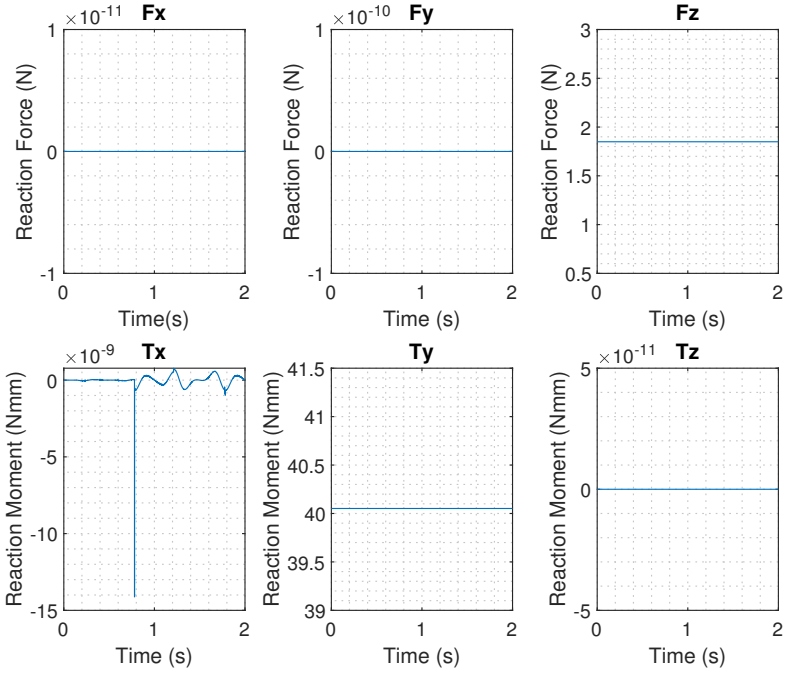

Figure 3: Reaction forces and moments for the balanced case with $\theta_1 = 30\,sin(2\pi\,t)$ and $\theta_2 = 50\,sin(2\pi\,t)$ degrees

For both tests, the reaction force graphs are similar. This is in line with the expectation because the counter-inertia's should not have any influence on the force balance of the joint.

It is clearly visible that the reaction moments reduced significantly with the inclusion of the counter-rotations. In the balanced case, these reaction moments are almost constant. The non-zero elements could be attributed to numerical errors due to the finite number of decimals used in ADAMS and to numerical integration errors. With these results, the theory regarding the moment balance of a 2 DoF link can be assumed to be correct.

Appendix H

Simulation inaccuracies using ADAMS

Simulation inaccuracies using ADAMS

As can be seen in the ADAMS simulation results, a significant amount of noise is present in the results. In this appendix, the errors will be investigated, and we will estimate if the errors could be attributed to numerical errors.

1 Experiment 1: Setting all input angles to zero

In the first experiment, the values of θ_1, θ_2 and θ_3 are set to be zero using the motion tab in ADAMS. The mass parameters are calculated using MATLAB and imported into ADAMS with the highest possible number of decimals. The resulting graphs for the CoM positions can be seen in Figure 1. At first glance, this seems like a perfect force balance solution, but there are some inaccuracies.

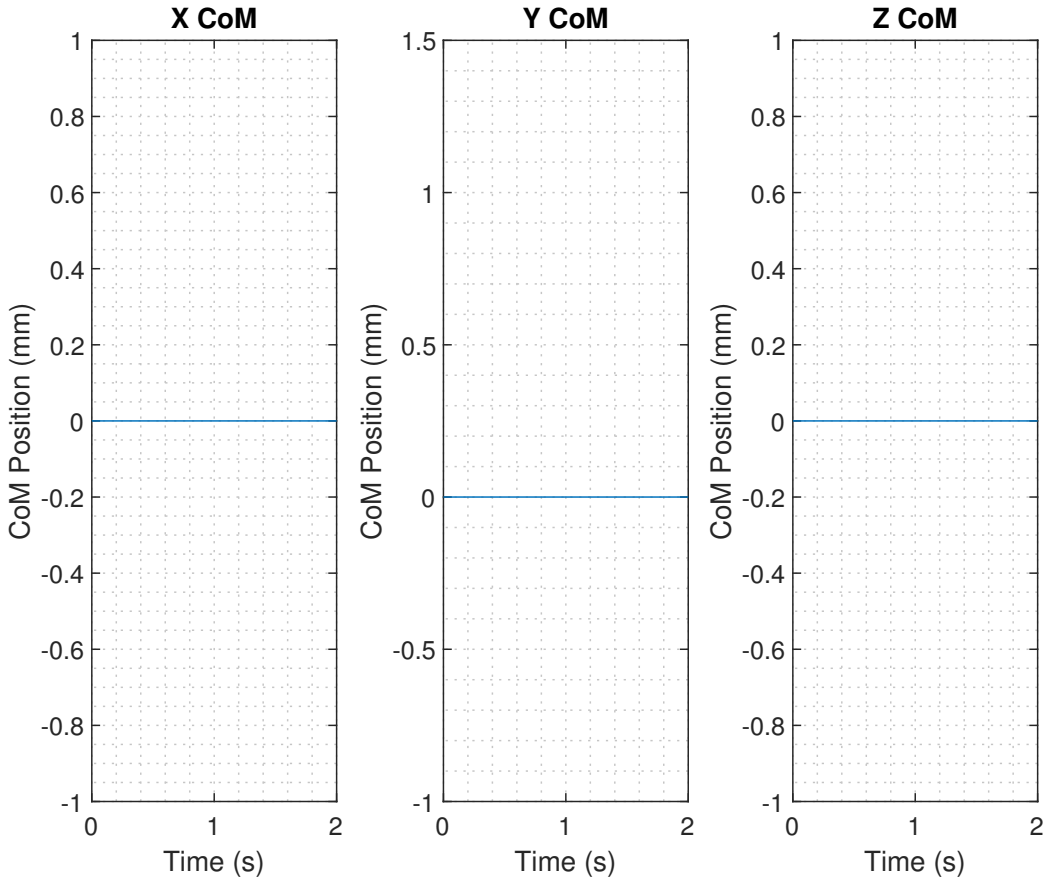

Figure 1: Simulation results for the CoM position of the linkage when the input angles are set to 0 degrees

Although the design variables were calculated to result in a total CoM position at the origin ($[0, 0, 0]$), the simulation results are not exactly zero, but a near-zero constant value in the order of 10^{-29} to 10^{-6}. When changing the stepsize for integration, the size of these non-zero values do also change.

2 Experiment 2: No input torques for different stepsizes

In the second experiment, the input torques are set to zero. Firstly with a stepsize of 4 ms and afterwards with a stepsize of 1 ms. For a perfectly force balanced linkage, both should result in constant CoM positions. The results from these experiments can be seen in Figures 2 and 3 respectively.

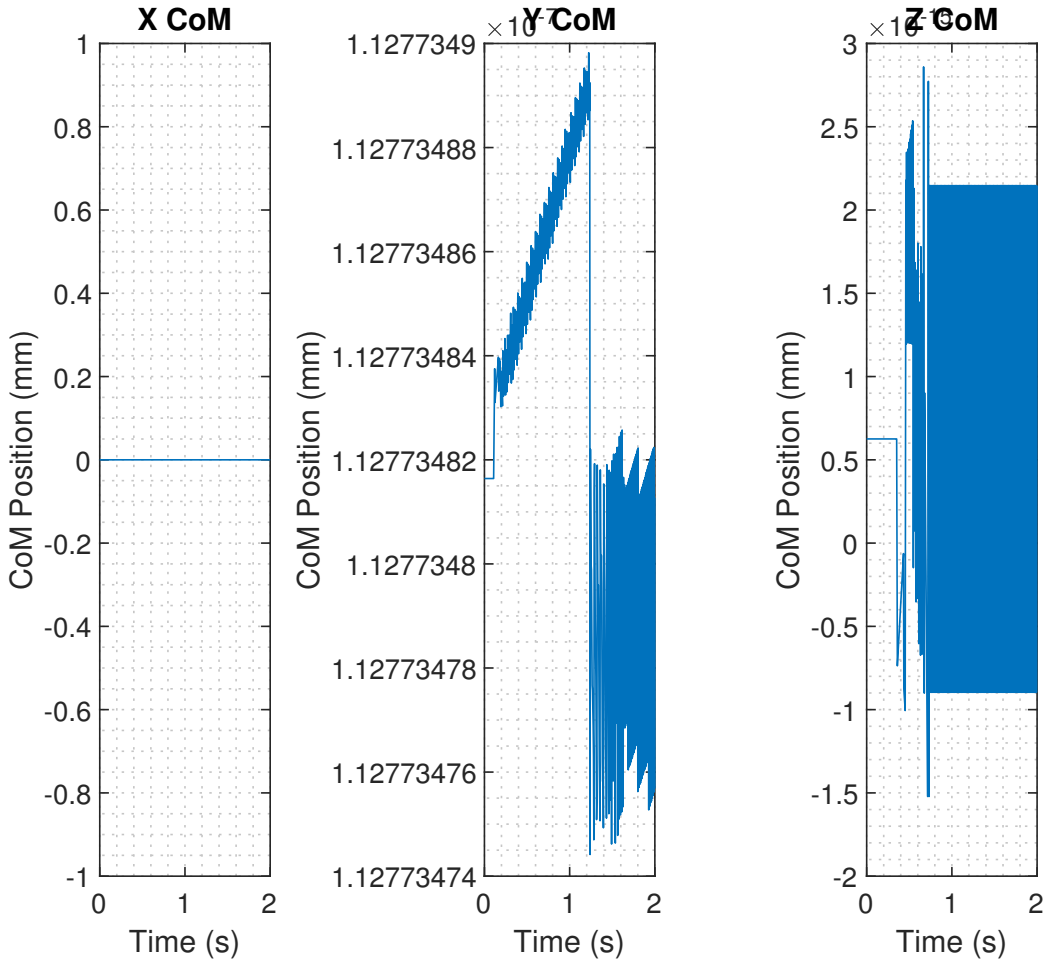

Figure 2: Noise in the CoM positions when no torques are applied to the linkage with a stepsize of 4ms

3 Discussion

For a perfectly balanced linkage, Figures 1, 2 and 3 should be identical. However, this is clearly not the case. Next to that, when alternating the stepsize of a linkage that should experience no motion (because it is force balanced and experiences no input torques), the results for the CoM positions change. These Figures suggest that these errors are due to numerical inaccuracies, most likely due to the finite number of decimals that can be inputted into ADAMS and to round-off errors. This explanation was also used for the simulation of the parallelepiped linkage in [3]

Another explanation for the noise in the moment balanced linkage could be the use of a coordinate projection method as described in [1]. During dynamic simulations, it commonly happens that after an integration step, the constraints are no longer satisfied. Using a coordinate projection method, the integration results of the last step are mapped back onto the constraint surface to meet the constraints. Using this process slightly changes the acceleration

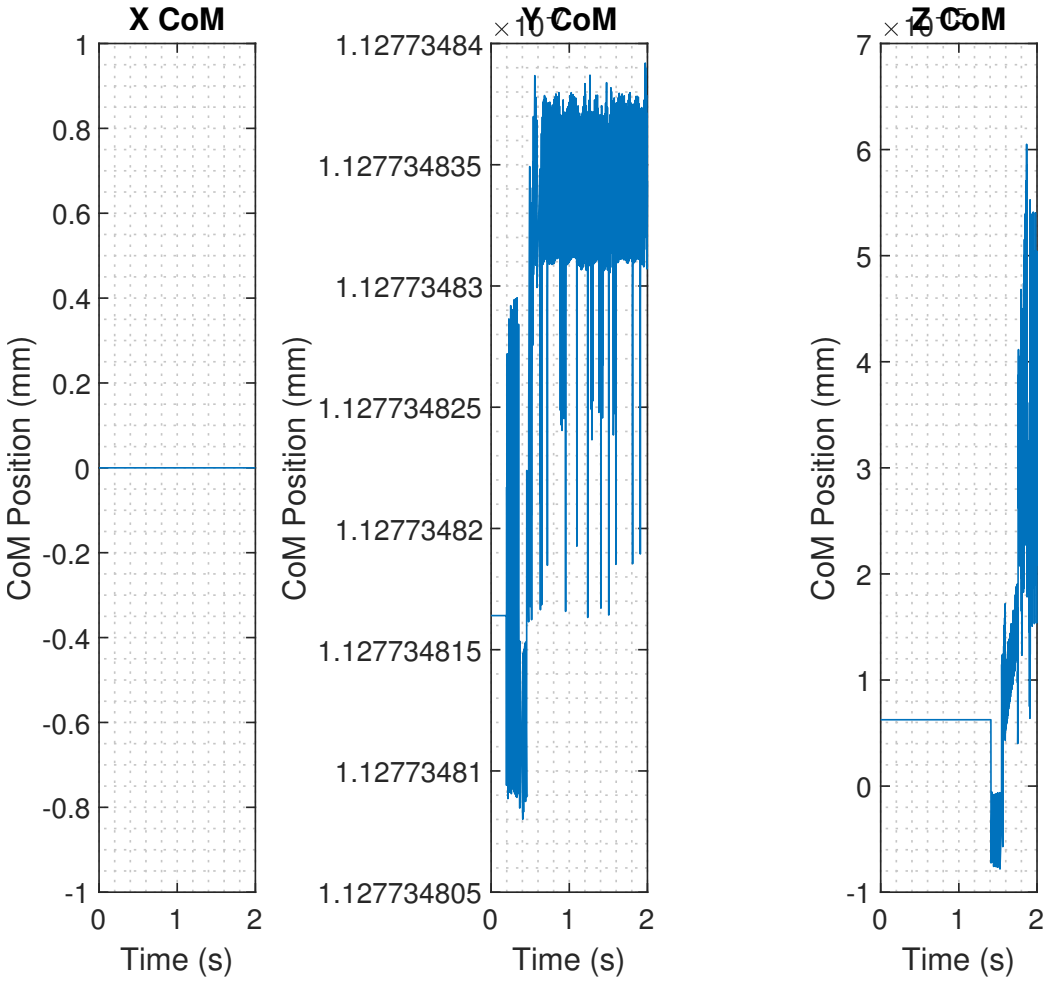

Figure 3: Noise in the CoM positions when no torques are applied to the linkage with a stepsize of 1ms

values for the links in the simulation results, but probably not the acceleration values of the counter-rotations, as for most of them their CoM does not move. This could lead to a little unbalance in the results.

It was also observed that this noise mainly occurs at near-zero values. When looking at the reaction moments around the y-axis of the balanced results, as presented in the paper, the value of the reaction moment is constant (minimal and maximal values are equal according to MATLAB). However, noise is observed when changing the mass of the counter-rotation for θ_3 to zero and thereby giving near-zero values to T_y. This suggests that the integration method does not perform well for near-zero values.

Lastly, the numerical noise could be explained by the used integration method. The default integration method that is used by ADAMS is a GSTIFF method. This method uses a variable stepsize and a variable order during integration. The GSTIFF is a fast and accurate method for computing displacements for a wide range of motion analysis problems [2]. Another available method in ADAMS is the WSTIFF method, which is comparable to the GSTIFF method. The main difference between these methods is that in the GSTIFF method coefficients are calculated assuming a constant step size, whereas WSTIFF coefficients are a function of the stepsize [2]. If the stepsize is suddenly changed during integration, an error is introduced when using the GSTIFF method, while WSTIFF could handle these situations without loss in accuracy.

By experimenting in ADAMS, the GSTIFF method showed large peaks and noise in the results, whereas the WSTIFF method resulted in smooth curves. Therefore, it was chosen to use the WSTIFF method for all the integrations.

4 Conclusion

It was observed that the noise present in the integration results is most likely due to numerical errors during integration. However, some steps could be taken to reduce the size of the noise:

1. Insert all values with the maximum number of digits possible. This reduces inaccuracies in the simulation results due to a difference in precision between ADAMS and the MATLAB calculations for satisfying the balancing constraints.
2. Choose a proper integrator for the system. The WSTIFF integrator showed to work better than the standard GSTIFF integrator for the constrained spatial pantograph linkage.
3. Reduce the maximum error tolerance in the integration settings. The smallest possible setting is $1E-10$.
4. Choose a proper stepsize for the integration. Smoother results are generally obtained with smaller stepsizes, but these simulations take longer to run.

Although the amount of noise could be reduced with the tips stated here, numeric integration always comes with some inaccuracies. Therefore, we can still assume the dynamic balance conditions to be correct.

References

[1] H. Vallery and A. L. Schwab, *Advanced Dynamics*. Delft: Stichting Newton-Euler, Aug. 2020, vol. 3.

[2] SolidWorks, "Integration Methods," 2023.

[3] Y. Wu, "SYNTHESIS AND ANALYSIS OF REACTIONLESS SPATIAL PARALLEL MECHANISMS," PhD, Université Laval, Québec, 2003.

Appendix I

Detailed solution for the force and moment balance of compound four-bar linkage

Detailed solution for the force and moment balance of compound four-bar linkage

1 Introduction

This appendix is meant to give an in-depth explanation for the work done on the dynamically balanced compound four-bar mechanism. The methods and work in this document are based on the work of Berkof and Lowen (1969, 1971) on the dynamic balancing of four-bar mechanisms, and the work of Wu (2003) on the dynamic decoupling of four-bar mechanisms.

Compared to the different papers cited above, the benefit of this appendix are that the same notation is used throughout the whole calculation, and all the in-between steps are also shown which is often not possible in a paper.

2 Single fourbar prerequisites

In order to obtain dynamic balance conditions for the single four-bar, one should have a clear understanding of the kinematics of this linkage. This section will present a description of all parameters, and the essential geometric relations.

The four-bar mechanism that will be investigated, including the definitions for the used angles, can be seen in Fig. 1. Note that the angle ψ_2' is not correctly shown, and the arrow should stop at r_2'.

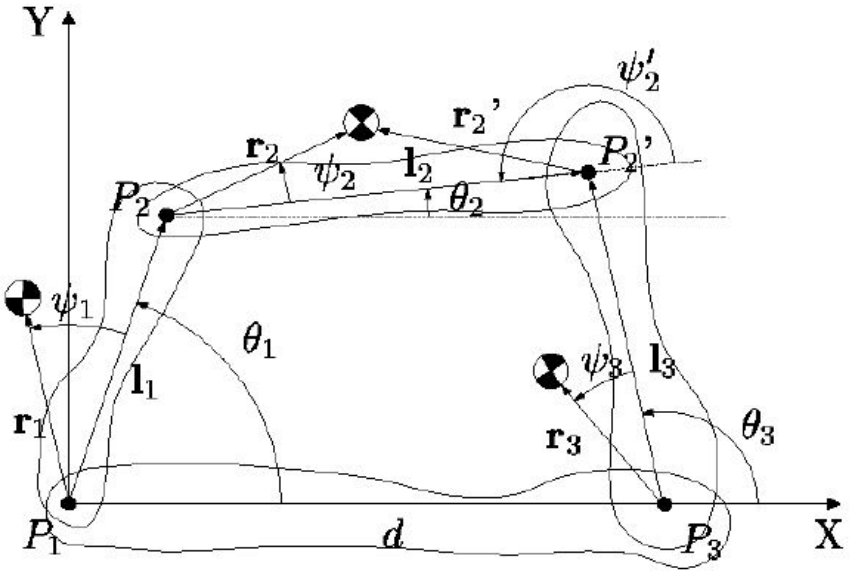

Figure 1: Schematic of a four-bar mechanism [4]

Instead of using all the link lengths as variables, we will use their ratio with L_2 as variables to simplify equations

later on. These ratios will be used as follows:

$$\mu_1 = \frac{L_1}{L_2}, \qquad \mu_2 = \frac{L_3}{L_2}, \qquad \mu_3 = \frac{d}{L_2} \tag{1}$$

2.1 Useful identities

The four-bar mechanism has complex geometric relations between the angles of the different links because it is a closed-loop linkage. In order to make equations more insightful, it is often helpful to use geometric identities.

These identities were calculated by expanding the expression on the left-hand side and then substituting the geometric constraint relation (Eq. 7) of a four-bar mechanism. This resulted in the following identities:

$$\begin{aligned} cos(\theta_1 - \theta_2) &= \tau_2 - \mu_1 \\ sin(\theta_1 - \theta_2) &= \tau_1 \\ sin(\theta_3 - \theta_2) &= \tau_3 \end{aligned} \tag{2}$$

In which τ_1 and τ_2 could be written as follows using the geometric conditions of a four-bar that are written down in Eq. 7.

$$\begin{aligned} \tau_1 &= \mu_2 sin(\theta_1 - \theta_3) + \mu_3 sin(\theta_1) \\ \tau_2 &= \mu_2 cos(\theta_1 - \theta_3) + \mu_3 cos(\theta_1) \\ \tau_3 &= \mu_1\, sin(\theta_1 - \theta_3) + \mu_3\, sin(\theta_3) \end{aligned} \tag{3}$$

2.1.1 Freudenstein Equation

Another useful equation for four-bar mechanisms is the Freudenstein equation from [5]. The calculation of this equation started with writing the relation between the links in the following vector form.

$$\mathbf{r}_{P_2/P_1} = \mathbf{r}_{P_1/P_3} + \mathbf{r}_{P_3/P_2'} - \mathbf{r}_{P_1/P_2} \tag{4}$$

With this vector form, it could be easily realized that the square of both sides should also be equal.

$$(\mathbf{r}_{P_2/P_1})^2 = L_2^2 = (\mathbf{r}_{P_1/P_3} + \mathbf{r}_{P_3/P_2'} - \mathbf{r}_{P_1/P_2})^2 \tag{5}$$

By filling in the vectors in Eq. 5 for the other links, the Freudenstein equation could finally be obtained:

$$\mu_1^2 + \mu_2^2 + \mu_3^2 - 1 = 2\,\mu_1\,\mu_2 cos(\theta_1 - \theta_3) + 2\,\mu_1\,\mu_3\,cos(\theta_1) - 2\,\mu_2\,\mu_3\,cos(\theta_3) \tag{6}$$

2.2 Geometric relations

In order to express all the equations in this appendix in a minimal set of coordinates (depending only on θ_1 and $\dot{\theta}_1$), the relation between the different angles has to be found. For the geometrics of the single four-bar mechanism, the following constraint equations must hold:

$$\begin{aligned} \mu_1\, cos(\theta_1) + cos(\theta_2) &= \mu_2\, cos(\theta_3) + \mu_3 \\ \mu_1\, sin(\theta_1) + sin(\theta_2) &= \mu_2\, sin(\theta_3) \end{aligned} \tag{7}$$

With this relation θ_3 could be written in terms of θ_1 and θ_2 in the following way

$$\begin{aligned} cos(\theta_3) &= \frac{\cos(\theta_2) - \mu_3 + \mu_1\, \cos(\theta_1)}{\mu_2} \\ sin(\theta_3) &= \frac{\sin(\theta_2) + \mu_1\, \sin(\theta_1)}{\mu_2} \end{aligned} \tag{8}$$

When substituting this into the trigonometric identity $cos^2(\theta_3) + sin^2(\theta_3) = 1$ the following results can be found for $sin(\theta_2)$:

$$sin(\theta_2) = -\frac{\mathrm{H} - \mu_3\, \cos(\theta_2) - \mu_1\,\mu_3\, \cos(\theta_1) + \mu_1\, \cos(\theta_1)\, \cos(\theta_2)}{\mu_1\, \sin(\theta_1)} \tag{9}$$

In which

$$H = \frac{1}{2}(\mu_1^2 - \mu_2^2 + \mu_3^2 + 1) \tag{10}$$

Then all that is left is to find an expression for $cos(\theta_2)$ in terms of θ_1. When using the trigonometric relation $cos^2(\theta_2) + sin^2(\theta_2) = 1$ an equation in the following form can be obtained:

$$\frac{A_2\, cos^2(\theta_2) + A_1\, cos(\theta_2) + A_0}{\mu_1^2(cos^2(\theta_1) - 1)} = 0 \tag{11}$$

In which

$$\begin{aligned} A_2 &= -{\mu_1}^2 + 2\,\cos(\theta_1)\,\mu_1\,\mu_3 - {\mu_3}^2 \\ A_1 &= 2\,{\mu_1}^2\,\mu_3\cos^2(\theta_1) - 2\,\mu_1\,{\mu_3}^2\,\cos(\theta_1) - 2\,\mathrm{H}\,\mu_1\,\cos(\theta_1) + 2\,\mathrm{H}\,\mu_3 \\ A_0 &= -\mathrm{H}^2 + 2\,\mathrm{H}\,\mu_1\,\mu_3\,\cos(\theta_1) - {\mu_1}^2\,{\mu_3}^2\cos^2(\theta_1) - {\mu_1}^2\cos^2(\theta_1) + {\mu_1}^2 \end{aligned} \tag{12}$$

Using the abc-formula, the following result can be obtained for $cos(\theta_2)$:

$$cos(\theta_2) = \frac{-A_1 + \epsilon\Delta}{2A_2} \tag{13}$$

in which ϵ is dependent on the assembly mode of the four-bar and has a value of either 1 or -1. More on that will follow in the next subsection. The value for Δ in the formula above can be written as:

$$\Delta = \sqrt{A_1^2 - 4A_2A_0} \tag{14}$$

Simplification of this equation in *MATLAB* results in the following expression:

$$\Delta = 2\,\mu_1\sqrt{\left(\cos(\theta_1)^2 - 1\right)\,(\mathrm{H}^2 - 2\,\mathrm{H}\,\mu_1\,\mu_3\,\cos(\theta_1) + {\mu_1}^2\,{\mu_3}^2\cos^2(\theta_1) - {\mu_1}^2 + 2\,\mu_1\,\mu_3\,\cos(\theta_1) - {\mu_3}^2)} \tag{15}$$

2.2.1 Assembly modes of the four-bar mechanism

As said above, the value of ϵ in Eq. 13 determines the assembly mode of the four-bar mechanism. There are two possible values for ϵ: 1 or -1. These are depicted in Fig. 2 and 3, respectively.

2.2.2 Simplification of the root of Δ

The root in the expression of Δ makes computation very difficult. Therefore it is necessary to simplify the expression of this root. This will be done in two ways in this section.

Extracting the $cos^2(\theta_1)$ term from the root

One way to simplify the root of Δ is by replacing the $(cos^2(\theta_1) - 1)$ term with $-sin^2(\theta_1)$ and extracting this from the root. This results in the following expression for Δ:

$$\begin{aligned} \Delta &= 2\,\mu_1\,\sin(\theta_1)\,\sqrt{-\mathrm{H}^2 + 2\,\mathrm{H}\,\mu_1\,\mu_3\,\cos(\theta_1) - {\mu_1}^2\,{\mu_3}^2\cos^2(\theta_1) + {\mu_1}^2 - 2\,\mu_1\,\mu_3\,\cos(\theta_1) + {\mu_3}^2} \\ &= 2\,\mu_1\,\sin(\theta_1)\,\xi \end{aligned} \tag{16}$$

We will call this simplification of Δ solution set CP0

Writing Δ as an exact square

Another way to simplify Δ is to write it as an exact square ($\sqrt{A^2} = |A|$) such that the square root is eliminated. We will start by writing Δ in the form

$$\Delta = \sqrt{\Omega} \tag{17}$$

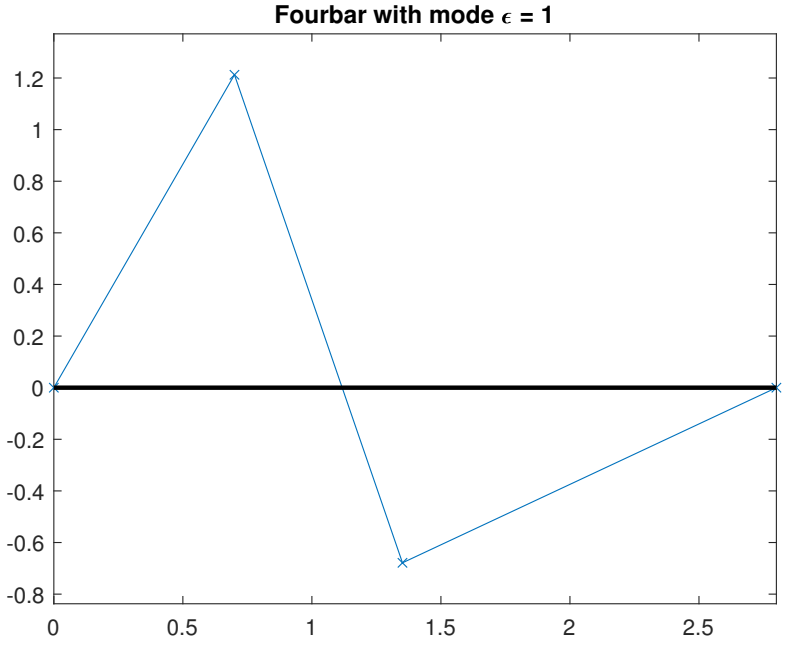

Figure 2: Assembly mode for $\epsilon = 1$

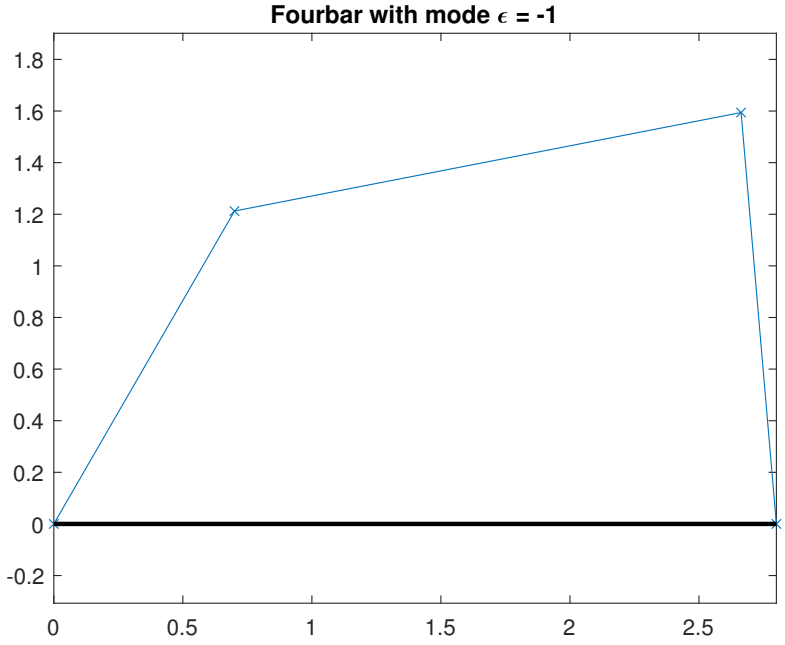

Figure 3: Assembly mode for $\epsilon = -1$

In which Ω could be written as a polynomial in the form

$$\Omega = \mu_1^2(b_4 cos^4(\theta_1) + b_3 cos^3(\theta_1) + b_2 cos^2(\theta_1) + b_1 cos(\theta_1) + b_0) \tag{18}$$

In which

$$\begin{aligned} b_4 &= 4\mu_1^2\mu_3^2 \\ b_3 &= -8\mu_1\mu_3(H-1) \\ b_2 &= 4H^2 - 4\mu_1^2\mu_3^2 - 4\mu_1^2 - 4\mu_3^2 \\ b_1 &= 8\mu_1\mu_3(H-1) \\ b_0 &= -4H^2 + 4\mu_1^2 + 4\mu^2 \end{aligned} \tag{19}$$

Let's suppose that we can write this equation of Ω in the following form that would simplify Δ tremendously

$$\Omega = (a_2 cos^2(\theta_1) + a_1 cos(\theta_1) + a_0)^2 \tag{20}$$

Expansion of Eq. 20 results in

$$\Omega = {a_2}^2 \cos(\theta_1)^4 + (2\,a_1\,a_2)\,\cos(\theta_1)^3 + \left({a_1}^2 + 2\,a_0\,a_2\right)\cos(\theta_1)^2 + (2\,a_0\,a_1)\,\cos(\theta_1) + {a_0}^2 \tag{21}$$

So in order to write Eq. 18 in the form of Eq. 20 the following equations must hold:

$$\begin{aligned} b_4 &= a_2^2 \\ b_3 &= 2a_1a_2 \\ b_2 &= a_1^2 + 2a_0a_2 \\ b_1 &= 2a_0a_1 \\ b_0 &= a_0^2 \end{aligned} \tag{22}$$

By comparing Eq. 18 and 21, the coefficients from Eq. 20 can be found. The equation with b_4 leads to:

$$a_2 = 2\mu_1\mu_2 \tag{23}$$

The negative form of this solution is also possible but is redundant because the equation will be squared, after which the square root is taken, resulting in the absolute value of the equation.

With the next equation, we can find:

$$a_1 = 2(1-H) = -{\mu_1}^2 + {\mu_2}^2 - {\mu_3}^2 + 1 \tag{24}$$

Then the other equations can be used to find the expression for a_0 and the conditions for the link lengths.

The equation with b_2 results in the following expression for a_0

$$a_0 = -\frac{{\mu_1}^2{\mu_3}^2 + {\mu_2}^2}{\mu_1\mu_3} \tag{25}$$

The equation with b_1 results in the following expression for a_0

$$a_0 = -2\mu_1\mu_3 \tag{26}$$

Equating Eq. 25 and 26 results in

$$\mu_2 = \mu_1\mu_3 \tag{27}$$

The equation with b_0 is very long and complex and will therefore not be shown here. In order to have this equation satisfy Eq. 25 and 26 two conditions are possible:

$$\mu_3 = 1 \tag{28}$$

$$\mu_1 = 1 \tag{29}$$

This results in two possible solution sets. The first one is called M4-F-CP1 in [4]:

$$\begin{aligned} L_2 &= d \\ L_1 &= L_3 \\ a_2 &= 2\mu_1 = 2\mu_2 \\ a_1 &= 2(1-H) = 0 \\ a_0 &= -2\mu_1 = -2\mu_2 \end{aligned} \tag{30}$$

The second one (M4-F-CP2 in [4])

$$\begin{aligned} L_2 &= L_1 \\ L_3 &= d \\ a_2 &= 2\mu_3 = 2\mu_2 \\ a_1 &= 2(1-H) = 0 \\ a_0 &= -2\mu_3 = -2\mu_2 \end{aligned} \tag{31}$$

With these sets of constraints, two solutions for Δ can be written. The absolute value signs can be eliminated from the equation by realizing that $cos^2(\theta_1) \leq 1$, and the two solution sets can be written as follows:

$$\Delta_{CP1} = 2\mu_2^2 |cos^2(\theta_1) - 1| = 2\mu_2^2 [1 - cos^2(\theta_1)] \tag{32}$$

$$\Delta_{CP2} = 2\mu_2 |cos^2(\theta_1) - 1| = 2\mu_2 [1 - cos^2(\theta_1)] \tag{33}$$

2.3 Kinematic relations

By taking the time derivative of these constraint equations, relations between the angular velocities can be found. This leads to the following relation

$$\begin{aligned} \dot{\theta}_2 &= -\dot{\theta}_1 \frac{L_1 \left(\cos\left(\theta_1\right) \sin\left(\theta_3\right) - \cos\left(\theta_3\right) \sin\left(\theta_1\right)\right)}{L_2 \left(\cos\left(\theta_2\right) \sin\left(\theta_3\right) - \cos\left(\theta_3\right) \sin\left(\theta_2\right)\right)} \\ \dot{\theta}_3 &= -\dot{\theta}_1 \frac{L_1 \left(\cos\left(\theta_1\right) \sin\left(\theta_2\right) - \cos\left(\theta_2\right) \sin\left(\theta_1\right)\right)}{L_3 \left(\cos\left(\theta_2\right) \sin\left(\theta_3\right) - \cos\left(\theta_3\right) \sin\left(\theta_2\right)\right)} \end{aligned} \tag{34}$$

This could be rewritten to

$$\begin{aligned} \dot{\theta}_2 &= -\dot{\theta}_1 \frac{L_1 \sin\left(\theta_1 - \theta_3\right)}{L_2 \sin\left(\theta_2 - \theta_3\right)} \\ \dot{\theta}_3 &= -\dot{\theta}_1 \frac{L_1 \sin\left(\theta_1 - \theta_2\right)}{L_3 \sin\left(\theta_2 - \theta_3\right)} \end{aligned} \tag{35}$$

Using the geometric conditions from Eq. 7 and by assigning variable names, the kinematic conditions could be simplified to

$$\begin{aligned} \dot{\theta}_2 &= \frac{\mu_1}{\tau_3} sin(\theta_1 - \theta_3)\, \dot{\theta}_1 \\ \dot{\theta}_3 &= \frac{\mu_1 \tau_1}{\mu_2 \tau_3} \dot{\theta}_1 \end{aligned} \tag{36}$$

3 Force balancing

Force balance conditions were calculated in [1] using the method of linearly independent vectors. In [6], this was calculated by calculating the CoM position of the total mechanism, and searching for conditions for which this position is constant.

The conditions calculated in these papers are only sufficient and not necessary, meaning that these calculations lead to superfluous constraints. This is because they do not express the CoM expression in a minimal set of coordinates. Because the mechanism only has 1 DoF, the equation should be expressed using 1 independent variable. However, they use both θ_1 and θ_2 as variables in their equations.

3.1 Constant Centre of Mass

The force acting on the base of a mechanism is equal to the time derivative of the linear momentum in that system, as can be seen in the following equation

$$\mathbf{F} = \dot{\mathbf{p}} = \frac{d}{dt}(m\mathbf{v}) = 0 \tag{37}$$

In order to have zero reaction forces, the velocity of the CoM should be constant or zero. Because it is not feasible to have a mechanism in which the CoM has a constant linear velocity, it can be stated that the CoM should be at a constant point in space. The conditions to have a constant position of the CoM can be calculated in two ways. Firstly the method of linearly independent vectors as in [1] will be explained, and afterwards a vector-based method.

For both methods, the CoM of a four-bar mechanism as depicted in Fig. 1 could be calculated using Eq. 38.

$$\mathbf{r}_s = \frac{1}{m_1 + m_2 + m_3} \sum_{i=1}^{3} m_i \mathbf{r}_i = \frac{1}{M_{tot}} \sum_{i=1}^{3} m_i \mathbf{r}_i \tag{38}$$

In this equation vector $\mathbf{r}$ represents a vector from the origin to the CoM of each link.

3.1.1 Method of linearly independent vectors

This section will briefly discuss the method of linearly independent vectors. This method is used in [1] to obtain the force balance conditions.

The position vectors of the individual link CoMs could be written as follows

$$\begin{aligned} \mathbf{r}_1 &= r_1 e^{i(\theta_1 + \psi_1)} \\ \mathbf{r}_2 &= L_1 e^{i\psi_1} + r_2 e^{i(\theta_2 + \psi_2)} \\ \mathbf{r}_3 &= d e^1 + r_3 e^{i(\theta_3 + \psi_3)} \end{aligned} \tag{39}$$

Substituting this into Eq. 38 results in an equation that is linearly dependent. Berkof and Lowen(1969) claim that this equation could be made linearly independent by including the loop closure equation (Eq. 7). However, the equation is still dependent on θ_1 and θ_3 which have linearly dependent terms. As also claimed in [4], the obtained conditions are sufficient but not necessary!

These conditions are discussed here because they are used in other literature. The conditions found with this method are:

$$\begin{aligned} m_1 r_1 &= m_2 r_2' \mu_1 \\ m_3 r_3 &= m_2 r_2 \mu_2 \\ \psi_1 &= \psi_2' \\ \psi_3 &= \psi_2 + \pi \end{aligned} \tag{40}$$

3.1.2 Vector-based method

The method presented here was also used in [6]. However, they only found sufficient conditions in that paper because they did not express Eq. 38 in a minimal set of coordinates.

The CoM coordinates for this method are:

$$\begin{aligned} x_1 &= r_1 \cos(\psi_1 + \theta_1) \\ y_1 &= r_1 \sin(\psi_1 + \theta_1) \\ x_2 &= r_2 \cos(\psi_2 + \theta_2) + \mu_1 L_2 \cos(\theta_1) \\ y_2 &= r_2 \sin(\psi_2 + \theta_2) + \mu_1 L_2 \sin(\theta_1) \\ x_3 &= r_3 \cos(\psi_3 + \theta_3) + \mu_3 L_2 \\ y_3 &= r_3 \sin(\psi_3 + \theta_3) \end{aligned} \tag{41}$$

Filling in these coordinates into Eq. 38 leads to the following expression

$$\mathbf{r}_s = \frac{1}{M_{tot}} \begin{pmatrix} (r_1 \cos(\psi_1 + \theta_1))\, m_1 + (r_2 \cos(\psi_2 + \theta_2) + \mu_1 L_2 \cos(\theta_1))\, m_2 + (\mu_3 L_2 + r_3 \cos(\psi_3 + \theta_3))\, m_3 \\ (r_1 \sin(\psi_1 + \theta_1))\, m_1 + (r_2 \sin(\psi_2 + \theta_2) + \mu_1 L_2 \sin(\theta_1))\, m_2 + (r_3 \sin(\psi_3 + \theta_3))\, m_3 \end{pmatrix} \tag{42}$$

By using the closed loop constraint equation to express $cos(\theta_2)$ and $sin(\theta_2)$ in other angles the CoM coordinate vector could be rewritten to

$$\mathbf{r}_s = \frac{1}{M_{tot}} \begin{pmatrix} A_1 \cos(\theta_1) + A_2 \sin(\theta_1) + A_3 \cos(\theta_3) + A_4 \sin(\theta_3) + A_5 \\ B_1 \cos(\theta_1) + B_2 \sin(\theta_1) + B_3 \cos(\theta_3) + B_4 \sin(\theta_3) + B_5 \end{pmatrix} \tag{43}$$

In which

$$\begin{aligned} A_1 &= \mu_1 L_2\, m_2 + m_1\, r_1 \cos(\psi_1) - m_2\, \mu_1\, r_2 \cos(\psi_2) && = R_{P3} \\ A_2 &= \mu_1\, m_2\, r_2 \sin(\psi_2) - m_1\, r_1 \sin(\psi_1) && = -R_{P1} \\ A_3 &= m_3\, r_3 \cos(\psi_3) + \mu_2\, m_2\, r_2 \cos(\psi_2) && = R_{P4} \\ A_4 &= -\left(m_3\, r_3 \sin(\psi_3) + \mu_2\, m_2\, r_2 \sin(\psi_2)\right) && = -R_{P2} \\ A_5 &= \mu_3 L_2\, m_3 + m_2\, \mu_3\, r_2 \cos(\psi_2) \\ B_1 &= m_1\, r_1 \sin(\psi_1) - \mu_1\, m_2\, r_2 \sin(\psi_2) && = R_{P1} \\ B_2 &= \mu_1 L_2\, m_2 + m_1\, r_1 \cos(\psi_1) - \mu_1\, m_2\, r_2 \cos(\psi_2) && = R_{P3} \\ B_3 &= m_3\, r_3 \sin(\psi_3) + \mu_2\, m_2\, r_2 \sin(\psi_2) && = R_{P2} \\ B_4 &= m_3\, r_3 \cos(\psi_3) + \mu_2\, m_2\, r_2 \cos(\psi_2) && = R_{P4} \\ B_5 &= m_2\, \mu_3\, r_2 \sin(\psi_2) \end{aligned} \tag{44}$$

It can be seen that the coefficients in Eq. 44 are almost identical for the x- and y-equation. These are also equations 54 till 7 in [4].

In the papers from [1] and [6], all coefficients from Eq. 44, except for A_5 and B_5, were set to zero for force balance. This leads to the set of constraints as presented before in Eq. 40. However, in this set, they are written as:

$$\begin{aligned} R_{P1} &= m_1\, r_1 \sin(\psi_1) - \mu_1\, m_2\, r_2 \sin(\psi_2) && = 0 \\ R_{P2} &= m_3\, r_3 \sin(\psi_3) + \mu_2\, m_2\, r_2 \sin(\psi_2) && = 0 \\ R_{P3} &= \mu_1 L_2\, m_2 + m_1\, r_1 \cos(\psi_1) - \mu_1\, m_2\, r_2 \cos(\psi_2) && = 0 \\ R_{P4} &= m_3\, r_3 \cos(\psi_3) + \mu_2\, m_2\, r_2 \cos(\psi_2) && = 0 \end{aligned} \tag{45}$$

The solution set M4 then becomes:

$$\begin{aligned} \epsilon &= \pm 1 \\ R_{P1} &= 0 \\ R_{P2} &= 0 \\ R_{P3} &= 0 \\ R_{P4} &= 0 \end{aligned} \tag{46}$$

These conditions are determined using a set of equations that is not linearly independent. Thereby the found conditions are sufficient but not necessary. Therefore, another method for finding the constraints is needed.

3.1.3 Vector-based method with a simplification of Δ

Force balance conditions for M4-F-CP0

Case CP was first investigated to find new balance conditions. The equations are very elaborate and do not give new insights. Therefore, they will not be shown here. The solution set found with simplification CP0 for Δ was:

$$\begin{aligned} \epsilon &= \pm 1 \\ \Delta &= 2\,\mu_1\,sin(\theta_1)\,\xi \\ \psi_2 &= n\pi \\ R_{P1} &= 0 \\ R_{P2} &= 0 \\ R_{P3} &= 0 \\ R_{P4} &= 0 \end{aligned} \tag{47}$$

This solution set is a subset from Eq. 46 and therefore, we will not look further into this solution. As will be seen later, the constraint $\psi_2 = n\,\pi$ will also follow from the moment balance of solution set M4 later on.

Force balance conditions for M4-F-CP1

In this solution set, the conditions are $L_1 = L_3$ and $L_2 = d$. This means that, when in upright mode ($\epsilon = -1$), the four-bar becomes a parallelogram mechanism. Thereby, all links are rotating in the same direction during movement, and by intuition we can see that no moment balance is possible without counter-rotations in this mode. Therefore, this solution set only works for $\epsilon = 1$. Filling in the conditions from Eq. 30 and the simplification from Eq. 32 into the equation for the CoM (Eq. 38) leads to an expression in the following form:

$$\bar{y}_{CP1} = \frac{A_{30}cos^3(\theta_1) + [A_{21}sin(\theta_1) + A_{20}]\,cos^2(\theta_1) + [A_{11}sin(\theta_1) + A_{10}]\,cos(\theta_1) + A_{01}sin(\theta_1) + A_{00}}{M_{tot}sin(\theta_1)(\mu_2^2 - 2\mu_2 cos(\theta_1) + 1)} \tag{48}$$

In which

$$\begin{aligned} A_{30} &= 2\mu_2 R_{P3} \\ A_{21} &= -2\mu_2 R_{P1} \\ A_{20} &= (1-\mu_2^2)R_{P4} - (1+\mu_2^2)R_{P3} \\ A_{11} &= (1+\mu_2^2)R_{P1} + (1+\mu_2^2)R_{P2} - 2\mu_2 m_2 r_2\,sin(\psi_2) \\ A_{10} &= -2\mu_2 R_{P3} \\ A_{01} &= -2\mu_2 R_{P2} + m_2 r_2\,sin(\psi_2)(\mu_2^2+1) \\ A_{00} &= (1+\mu_2^2)R_{P3} + (\mu_2^2-1)R_{P4} \end{aligned} \tag{49}$$

From which the coefficients R_{P1}, R_{P2}, R_{P3} and R_{P4} are identical to these terms in Eq. 45, using the conditions from Eq. 30.

To have $\bar{y}_{CP1}$ constant for any value of θ_1, the nominator of Eq. 48 has to be zero, or the denominator should be infinite. Due to the presence of $sin(\theta_1)$ in the denominator, it could not be infinite for all values of θ_1, and therefore the nominator should be zero. This could be done by setting all the coefficients to zero. Thereby ψ_2 should be set to be $n\pi$ to have all equations equal to zero. So the conditions are:

$$
\begin{aligned}
\epsilon &= 1 \\
L_1 &= L_3 \\
L_2 &= d \\
\Delta &= 2\mu_2^2[1 - cos^2(\theta_1)] \\
\psi_2 &= n\pi \\
R_{P1} &= 0 \\
R_{P2} &= 0 \\
R_{P3} &= 0 \\
R_{P4} &= 0
\end{aligned}
\tag{50}
$$

With these conditions, the mechanism also has a constant x-position of the CoM.

Force balance conditions for M4-F-CP2

Now we will look into the force balance conditions using the simplification for Δ using solution set M4-F-CP2.

When writing out the y-position of the CoM of the mechanism, again an equation in the form of Eq. 48 is obtained. However, now the coefficients are:

$$
\begin{aligned}
A_{30} &= 2\mu_2\, R_{P3} + (1 - \epsilon)\, R_{P4} \\
A_{21} &= (\epsilon - 1)\, R_{P2} - 2\mu_2\, R_{P1} \\
A_{20} &= \mu_2(\epsilon - 1)\, R_{P4} - (1 + \mu_2^2)\, R_{P3} \\
A_{11} &= (1 + \mu_2^2)\, R_{P1} + 2\mu_2 m_3 r_3\, sin(\psi_3) \\
A_{10} &= (\epsilon - 1)\, R_{P4} - 2\mu_2\, R_{P3} \\
A_{01} &= (1 - \epsilon)\, R_{P2} - m_3 r_3\, (\mu_2^2 + 1)\, sin(\psi_3) \\
A_{00} &= (1 + \mu_2^2)\, R_{P3} + (1 - \epsilon)\, \mu_2\, R_{P4}
\end{aligned}
\tag{51}
$$

Again, the coefficients R_{P1}, R_{P2}, R_{P3} and R_{P4} are identical to these terms in Eq. 45, using the conditions from Eq. 31.

In Eq. 51, in all equations that contain R_{P2} or R_{P4}, they are multiplied by $(\epsilon - 1)$. So in order to get these parts of the equations to zero, we can either set $\epsilon = 1$ or $R_{P2} = R_{P4} = 0$.

With $\epsilon = 1$ we get the following solution set M4-F-CP2a:

$$
\begin{aligned}
\epsilon &= 1 \\
L_2 &= L_1 \\
L_3 &= d \\
\Delta &= 2\mu_2[1 - cos^2(\theta_1)] \\
\psi_3 &= n\pi \\
R_{P1} &= 0 \\
R_{P3} &= 0
\end{aligned}
\tag{52}
$$

The other solution set M4-F-CP2b is:

$$\begin{aligned} \epsilon &= \pm 1 \\ L_2 &= L_1 \\ L_3 &= d \\ \Delta &= 2\mu_2[1 - cos^2(\theta_1)] \\ \psi_3 &= n\pi \\ R_{P1} &= 0 \\ R_{P2} &= 0 \\ R_{P3} &= 0 \\ R_{P4} &= 0 \end{aligned} \tag{53}$$

4 Moment Balance

In the last section, conditions for force balancing were found. This section will focus on the moment balance of the four-bar mechanism, i.e. the conditions for which the four-bar does not induce any reaction moments to its base during motion. In order to obtain these conditions, we will start with a simplification of the angular momentum equation, after which we will extract the conditions for which the total angular momentum of the mechanism vanishes.

4.1 Angular Momentum

The derivation is based on [2], but written according to the variables used in Fig. 1. The total angular momentum of a mechanism consists of two parts. Firstly, the angular momentum generated by moving the CoMs of the mechanism in a circular trajectory with respect to the origin, the *orbital angular momentum*. Secondly, the angular momentum generated by the rotation of the links, the *spin angular momentum*. This is written down in equation 54.

$$\mathbf{H}_o = \sum_{i=1}^{3} (\mathbf{r}_i \times m_i \dot{\mathbf{r}}_i + m_i k_i^2 \dot{\theta}_i) \tag{54}$$

For a planar mechanism this could be rewritten in a scalar form:

$$H_o = \sum_{i=1}^{3} H_i = \sum_{i=1}^{3} m_i (x_i \dot{y}_i - y_i \dot{x}_i + k_i^2 \dot{\theta}_i) \tag{55}$$

In this equation, x_i and y_i are the coordinates for the CoMs of the individual links with respect to the origin, which is at P_1 in the four-bar mechanism. These coordinates can be seen in Eq. 41.

When filling in these coordinates into Eq. 55, the following equation is obtained

$$\begin{aligned} H_o = &\left(m_2 \left({L_1}^2 + r_2 \cos(\psi_2 - \theta_1 + \theta_2)\, L_1\right) + m_1 \left({k_1}^2 + {r_1}^2\right)\right) \dot{\theta}_1 \\ &+ \left(m_2 \left({k_2}^2 + {r_2}^2 + L_1 \cos(\psi_2 - \theta_1 + \theta_2)\, r_2\right)\right) \dot{\theta}_2 \\ &+ \left(m_3 \left({k_3}^2 + {r_3}^2 + d \cos(\psi_3 + \theta_3)\, r_3\right)\right) \dot{\theta}_3 \end{aligned} \tag{56}$$

This equation is not very insightful yet. Therefore it will be rewritten using the identities from Eq. 2. With these identities, the angular momentum can be written as

$$\begin{aligned} H_o = &\left({L_1}^2 m_2 + {k_1}^2 m_1 + m_1 {r_1}^2 + L_1 m_2 r_2 \tau_1 \sin(\psi_2) - L_1 m_2 r_2 \cos(\psi_2)\,(\mu_1 - \tau_2)\right) \dot{\theta}_1 \\ &+ \left({k_2}^2 m_2 + m_2 {r_2}^2 + L_1 m_2 r_2 \tau_1 \sin(\psi_2) - L_1 m_2 r_2 \cos(\psi_2)\,(\mu_1 - \tau_2)\right) \dot{\theta}_2 \\ &+ \left({k_3}^2 m_3 + m_3 {r_3}^2 + d\, m_3 r_3 \cos(\psi_3) \cos(\theta_3) - d\, m_3 r_3 \sin(\psi_3) \sin(\theta_3)\right) \dot{\theta}_3 \end{aligned} \tag{57}$$

To rewrite this expression, the following kinematic relation is used (see Fig. 1)

$$r_2 cos(\psi_2) = L_2 + r_2' cos(\psi_2') \tag{58}$$

With this relation, and by rearranging the expression, equation 57 could finally be written to

$$\begin{aligned} H_o = &\dot{\theta}_1 \left(m_1 \left({k_1}^2 + {r_1}^2\right) - L_1 m_2 \mu_1 {r}_2' \cos(\psi_2')\right) \\ &+ \dot{\theta}_2\, m_2 \left({k_2}^2 + r_2 \left(r_2 - L_2 \cos(\psi_2)\right)\right) \\ &+ \dot{\theta}_3\, m_3 \left({k_3}^2 + r_3 \left(r_3 - L_3 \cos(\psi_3)\right)\right) + V + W \end{aligned} \tag{59}$$

In which the variables V and W are:

$$V = \cos(\psi_2) \left(L_1 \dot{\theta}_2 m_2 r_2 \left(\tau_2 - \mu_1 + \frac{1}{\mu_1}\right) + L_1 \dot{\theta}_1 m_2 r_2 \tau_2 + \frac{\dot{\theta}_3 m_3 r_3 \cos(\psi_3)\,(L_3 + d \cos(\theta_3))}{\cos(\psi_2)}\right) \tag{60}$$

$$W = \sin(\psi_2) \left(L_1 m_2 r_2 \tau_1 \left(\dot{\theta}_1 + \dot{\theta}_2\right) - \frac{d \dot{\theta}_3 m_3 r_3 \sin(\psi_3) \sin(\theta_3)}{\sin(\psi_2)}\right) \tag{61}$$

Using the force balance conditions from Berkof and Lowen

In this section, the moment balance solution will be worked out using the force balancing conditions as stated in [1]. These force balance conditions are shown in Eq. 40

These conditions are not calculated using a minimal set of coordinates, and are thereby sufficient but not necessary for a statically balanced mechanism. However, they will be used to follow the calculations in other reports more easily.

Simplification of V

Filling in the condition from Eq. 40 into Eq. 60 leads to the following expression:

$$V = m_2 L_2 r_2 cos(\psi_2)[\mu_1\tau_2\dot{\theta}_1 + (\mu_1\tau_2 - \mu_1^2 + 1)\dot{\theta}_2 - (\mu_2 + \mu_3\, cos(\theta_3))\mu_2\dot{\theta}_3] = V_1\, V_2 \tag{62}$$

For shorter writing, this expression will be split up in V_1 and V_2 in which V_2 is the part between the square brackets.

Filling in the kinematic relations (Eq. 34) leads to the following expression

$$V_2 = [\mu_1\tau_2\dot{\theta}_1 + (\mu_1\tau_2 - \mu_1^2 + 1)\frac{\mu_1}{\tau_3}\, sin(\theta_1 - \theta_3)\,\dot{\theta}_1 - (\mu_2 + \mu_3\, cos(\theta_3))\frac{\mu_1\tau_1}{\tau_3}\dot{\theta}_1] \tag{63}$$

$$V_2\frac{\tau_3}{\mu_1} = [\tau_2\tau_3 + (\mu_1\tau_2 - \mu_1^2 + 1)\, sin(\theta_1 - \theta_3) - (\mu_2 + \mu_3\, cos(\theta_3))\tau_1]\,\dot{\theta}_1 \tag{64}$$

Writing out the terms τ_1, τ_2 and τ_3 as in Eq. 3 and rearranging the equation leads to

$$\begin{aligned} V_2\frac{\tau_3}{\mu_1\dot{\theta}_1} =& [2\mu_1\mu_2 cos(\theta_1 - \theta_3) + 2\mu_1\mu_3 cos(\theta_1) - \mu_2\mu_3 cos(\theta_3) + 1 - \mu_1^2 - \mu_2^2]\, sin(\theta_1 - \theta_3) \\ &+ [\mu_2\mu_3 cos(\theta_1 - \theta_3) + \mu_3^2 cos(\theta_1)]\, sin(\theta_3) \\ &- [\mu_3^2 cos(\theta_3) + \mu_2\mu_3] sin(\theta_1) \end{aligned} \tag{65}$$

Now we want to write everything in terms of $sin(\theta_1 - \theta_3)$. This could be done by rewriting in the following way:

$$\mu_3^2[cos(\theta_1)sin(\theta_3) - cos(\theta_3)sin(\theta_1)] = -\mu_3^2 sin(\theta_1 - \theta_3) \tag{66}$$

$$\begin{aligned} &\mu_2\mu_3[cos(\theta_1 - \theta_3)sin(\theta_3) - sin(\theta_1)] \\ =& \mu_2\mu_3[cos(\theta_1)cos(\theta_3)sin(\theta_3) + sin(\theta_1)sin(\theta_3)^2 - sin(\theta_1)] \\ =& \mu_2\mu_3[cos(\theta_1)cos(\theta_3)sin(\theta_3) + sin(\theta_1)(1 - cos^2(\theta_3) - 1)] \\ =& \mu_2\mu_3[-sin(\theta_1 - \theta_3)cos(\theta_3)] \end{aligned} \tag{67}$$

With Eq. 66 and 67, Eq. 65 could finally be rewritten to

$$V_2\frac{\tau_3}{\mu_1\dot{\theta}_1} = [2\mu_1\mu_2 cos(\theta_1 - \theta_3) + 2\mu_1\mu_3 cos(\theta_1) - 2\mu_2\mu_3 cos(\theta_3) + 1 - \mu_1^2 - \mu_2^2 - \mu_3^2]\, sin(\theta_1 - \theta_3) \tag{68}$$

When comparing this result with the Freudenstein Equation (6) it can be seen that with these force-balance conditions, V simplifies to

$$V = 0 \tag{69}$$

Simplification of W

After substituting the force balance conditions from Eq. 40 and including the kinematic constraints from Eq. 34 the expression for W from Eq. 61 becomes

$$W = L_2 m_2 r_2 \mu_1 \tau_1 sin(\psi_2)[\tau_3 + \mu_3 sin(\theta_3) + \mu_1 sin(\theta_1 - \theta_3)]\frac{\dot{\theta}_1}{\tau_3} \tag{70}$$

When comparing this with the expression for τ_3 from Eq. 3 the expression between the square brackets could be rewritten to $2\tau_3$ which finally results in

$$W = 2L_2 m_2 r_2 \mu_1 \tau_1 sin(\psi_2)\dot{\theta}_1 \tag{71}$$

Final simplified angular momentum equation

With the results obtained by the simplification of V and W, and substituting the force balance conditions of Eq. 40 into Eq. 59, one finally obtains that

$$H_o = \sum_{i=1}^{3} m_i(k_i^2 + r_i^2 - L_i r_i cos(\theta_i))\,\dot{\theta}_i + 2L_1 m_2 r_2 sin(\psi_2) sin(\theta_1 - \theta_2)\dot{\theta}_1 \tag{72}$$

Which can be written more compactly in the following way:

$$H_o = \sum_{i=1}^{3} I_i \dot{\theta}_i + I_a sin(\theta_1 - \theta_2)\dot{\theta}_1 \tag{73}$$

In which

$$I_i = m_i\,(k_i^2 + r_i^2 - r_i L_i cos(\psi_i)) \tag{74}$$

$$I_a = 2m_2 L_2 r_2 \mu_1 sin(\psi_2) \tag{75}$$

This equation is also used to calculate dynamic balance conditions in [4]. Although I_a and I_i have the same units as moment of inertia, it should not be mistaken to be moment of inertia. It is just a name for a random variable that is independent of the configuration of the mechanism.

Important note: Due to the force balancing conditions used in the simplification of the angular momentum function, this simplification is only valid for solution set M4, M4-F-CP0, M4-F-CP1, and M4-F-CP2b. So, it is not valid for M4-F-CP2a.

4.2 Moment balance for solution set M4

4.3 Moment balance for solution set M4-F-CP0

The simplified angular momentum equation (Eq. 72) could be expressed in a minimal set of coordinates using the expressions found in section 2.2 and 2.3. This results in the following expression for the angular momentum in a minimal set of coordinates

$$H_0 = [\frac{J_n}{J_d}]\,\dot{\theta}_1 \tag{76}$$

In which

$$J_n = \sum_{s=0}^{3}\sum_{t=0}^{1}\sum_{u=0}^{1} j_{s,t,u} cos^s(\theta_1) sin^t(\theta_1)\xi^u \tag{77}$$

$$J_d = 2\,\epsilon\,\xi\,\left({\mu_1}^2 - 2\,\cos(\theta_1)\,\mu_1\,\mu_3 + {\mu_3}^2\right) \tag{78}$$

In which

$$\begin{aligned}
j_{3,0,0} &= \mathrm{I_a}\,{\mu_1}^2\,{\mu_3}^3 \\
j_{2,0,0} &= -\mathrm{I_a}\,\mu_1\,{\mu_3}^2\,\left({\mu_1}^2 + 2\,\mathrm{H} - 2\right) \\
j_{1,1,1} &= -2\,\mathrm{I_a}\,\epsilon\,\mu_1\,{\mu_3}^2 \\
j_{1,1,0} &= -4\,{\mu_1}^2\,{\mu_3}^2\,(I_2 - I_3) \\
j_{1,0,1} &= -2\,\epsilon\,\mu_1\,\mu_3\,(2\,I_1 + I_2 + I_3) \\
j_{1,0,0} &= \mathrm{I_a}\,\mu_3\,\left(\mathrm{H}^2 + 2\,\mathrm{H}\,{\mu_1}^2 - 3\,{\mu_1}^2 - {\mu_3}^2\right) \\
j_{0,1,1} &= 2\,\mathrm{H}\,\mathrm{I_a}\,\epsilon\,\mu_3 \\
j_{0,1,0} &= 4\,\mu_1\,\mu_3\,\left(I_2\,{\mu_1}^2 + I_2\,{\mu_3}^2 - \mathrm{H}\,I_2 - \mathrm{H}\,I_3\right) \\
j_{0,0,1} &= 2\,\epsilon\,\left(I_1\,{\mu_1}^2 + I_2\,{\mu_1}^2 + I_1\,{\mu_3}^2 + I_3\,{\mu_1}^2\right) \\
j_{0,0,0} &= \mathrm{I_a}\,\mu_1\,\left(-4\,\mathrm{H}^2 + 4\,{\mu_1}^2 + 4\,{\mu_3}^2\right)
\end{aligned} \tag{79}$$

For moment balance, J_n should be zero for all values of θ_1. This could be achieved by setting all terms in Eq. 79 to zero. This is a necessary and sufficient condition according to [4] because all terms in Eq. 77 are linearly independent. This also holds for the terms with ξ due to the square root sign. Setting these equations to zero leads to two possible solution sets:

M4-F-CP0-I

$$\begin{aligned} I_a &= 0 \\ I_2 &= I_3 \\ I_1 &= -I_3 \\ I_1 &= 0 \end{aligned} \tag{80}$$

M4-F-CP0-II

$$\begin{aligned} I_a &= 0 \\ I_2 &= I_3 \\ I_1 &= -I_3 \\ \mu_2 &= 1 \\ \mu_1 &= \mu_3 \end{aligned} \tag{81}$$

In [4] it is claimed that these solutions are possibly not force balanced. However, in the calculations for this document, these conditions were readily included. So, these solutions only have to be checked for physical consistency. However, it should be checked that the conditions for moment balance also satisfy the conditions for force balance.

In both solutions, I_a has to be zero. This equation could become zero in the following ways

$$r_2 = 0 \tag{82}$$

$$\psi_2 = 2n\pi \tag{83}$$

$$\psi_2 = (2n+1)\pi \tag{84}$$

4.3.1 Check for solution set M4-F-CP0-I

For solution set M4-F-I, $r_2 = 0$ is not a valid solution because this would lead to the equation $I_2 = m_2 k_2^2 = 0$, which is not physically possible because a mass could not have a zero radius of gyration.

Filling in $\psi_2 = (2n+1)\pi$ into Eq. 74 results in $I_2 = m_2(k_2^2 + r_2^2 + L_2 r_2) = 0$ which also has no physical solution.

The last solution ($\psi_2 = 2n\pi$) would be a possible solution by looking at I_2. However, filling in this solution into the equations for I_3 and R_{P4} leads to:

$$\begin{aligned} I_3 = m_3\left[k_3^2 + r_3^2 - r_3 L_2 \mu_2\, cos(\psi_3)\right] &= 0 \\ R_{P4} = m_3 r_3\, cos(\psi_3) + \mu_2 m_2 r_2 &= 0 \end{aligned} \tag{85}$$

These equations clearly show an inconsistency because the cosine should be positive in the first equation, while in the second equation, this same cosine should be negative. Therefore, M4-F-CP0-I is not a valid solution set!

4.3.2 Check for M4-F-CP0-II

The condition that I_a should be zero results in the same option as in solution set M4-F-I. As also stated in [4], the solutions from Eq. 82 and 84 leads to an incompatibility in the force balance conditions. The solution in Eq. 83 is the only valid solution.

The last conditions from Eq. 81 could be rewritten as $L_3 = L_2$ and $L_1 = d$. With this, we could rewrite the force balance conditions from Eq. 40 as follows:

$$\begin{aligned} r_3 &= \frac{m_2 r_2}{m_3} \\ \psi_3 &= \psi_2 + \pi \end{aligned} \tag{86}$$

With a little bit of rewriting, the second condition could be written as $I_2 = -I_1$, which leads to the condition:

$$k_2 = \sqrt{\frac{-m_2 r_2^2 - I_1}{m_2}} \tag{87}$$

In the same way, the condition $I_3 = -I_1$ leads to

$$k_3 = \sqrt{\frac{-m_2^2 r_2^2 - m_3 I_1}{m_3^2}} \tag{88}$$

In order to not have any imaginary parts due to the minus sign in the square roots for k_2 and k_3, I_1 should be negative. This could only be achieved when ψ_1 is a multiple of π. Due to inconsistencies with other solutions as described in [4], the only valid solution for ψ_1 is $2n\pi$. Substitution of this into the static balance conditions leads to

$$r_2 = \frac{L_2(L_1 m_2 + m_1 r_1)}{L_1 m_2} \tag{89}$$

So, the total set of dynamic balance conditions for solution set M4-F-II is:

$$\begin{aligned}
\epsilon &= \pm 1 \\
L_1 &= d \\
L_2 &= L_3 \\
r_2 &= \frac{L_2(L_1 m_2 + m_1 r_1)}{L_1 m_2} \\
r_3 &= \frac{m_2 r_2}{m_3} \\
k_2 &= \sqrt{\frac{-m_2 r_2^2 - I_1}{m_2}} \\
k_3 &= \sqrt{\frac{-m_2^2 r_2^2 - m_3 I_1}{m_3^2}} \\
\psi_1 &= 0 \\
\psi_2 &= 0 \\
\psi_3 &= \pi
\end{aligned} \tag{90}$$

4.4 Moment balance for solution set M4-F-CP1

In this section, the conditions from Eq. 30 for having Δ as an exact square will be used in the simplified angular momentum equation from Eq. 72. This results in the following expression for the angular momentum in a minimal set of coordinates

$$H_0 = [\frac{J_n}{J_d}]\,\dot{\theta}_1 \tag{91}$$

In which

$$J_n = \sum_{s=0}^{1}\sum_{t=0}^{1} j_{s,t} cos^s(\theta_1) sin^t(\theta_1) \tag{92}$$

$$J_d = \epsilon\,[\mu_2^2 - 2\mu_2\,cos(\theta_1) + 1] \tag{93}$$

In which

$$\begin{aligned}
j_{1,0} &= -2\,\mu_2\,(I_1 + I_2) \\
j_{0,1} &= I_a\,(1 - \mu_2^2) \\
j_{0,0} &= I_1 - I_3 + \mu_2^2\,(I_1 + 2I_2 + I_3)
\end{aligned} \tag{94}$$

As mentioned before, J_n should be zero for a moment balanced mechanism. This results in three possible solution sets:

M4-F-CP1-I

$$\begin{aligned} I_a &= 0 \\ I_1 &= 0 \\ I_2 &= 0 \\ I_3 &= 0 \end{aligned} \tag{95}$$

M4-F-CP1-II

$$\begin{aligned} I_a &= 0 \\ I_2 &= -I_1 \\ I_3 &= I_1 \end{aligned} \tag{96}$$

M4-F-CP1-III

$$\begin{aligned} \mu_2 &= 1 \\ I_2 &= -I_1 \end{aligned} \tag{97}$$

Check for solution set M4-F-CP1-I

At first sight, this solution set looks feasible. However, due to the same reasons as described in Section 4.3.1 for solution set M4-F-I, this solution set has no physical solution.

Check for solution set M4-F-CP1-II

In this solution set, we again have the same three options to set I_a to zero:

$$\begin{aligned} r_2 &= 0 \\ \psi_2 &= 2n\pi \\ \psi_2 &= (2n+1)\pi \end{aligned} \tag{98}$$

With the solution $r_2 = 0$, it follows from R_{P2} and R_{P4} that $r_3 = 0$. Then it follows from R_{P1} and R_{P3} that $\psi_1 = \pi$, because when r_2 would be zero it would be impossible to set equation R_{P3} to zero otherwise. With these obtained solutions, we can fill in the second constraint:

$$I_2 = m_2 k_2^2 = -m_1 \left[k1^2 + r1^2 + \mu_1 r_1 L_2\right] = -I_1 \tag{99}$$

This equation clearly has no physical solutions. Therefore, the solution $r_2 = 0$ is not valid.

We will now look at the other two solutions by stating that $\psi_2 = n\pi$. From R_{P2} and R_{P4} it follows that $\psi_3 = \psi_2 + \pi$ and $r_3 = \frac{\mu_2 m_2 r_2}{m_3}$. Then we will use the equation $R_{P4} = 0$ to rewrite the last two conditions to $I_2 = -I_3$ which finally leads to:

$$m_2(k_2^2 + r_2^2) + m_3(k_3^2 + r_3^2) = m_2 r_2 L_2 \, cos(\psi_2)(1 - \mu_2^2) \tag{100}$$

Because all the terms on the left side are positive, it is clear that $cos(\psi_2) > 0$ and therefore $\psi_2 = 0$. With the last found conditions, it follows that $\psi_3 = \pi$.

In order to find a value for ψ_1 we will look at $R_{P1} = 0$. From this, three possible solutions can exist:

$$\begin{aligned} r_1 &= 0 \\ \psi_1 &= 2n\pi \\ \psi_1 &= (2n+1)\pi \end{aligned} \tag{101}$$

The solution $r_1 = 0$ leads to an inconsistency in the constraint $I_2 = -I_1$, which will finally become $m_2 k_2^2 = -m_1 k_1^2$ which has no physical solution.

In order to find which of the other two solutions for ψ_1 is valid, we will rewrite R_{P1} and R_{P3} using Eq. 58:

$$\begin{aligned} R_{P1} &= m_1 r_1 \, sin(\psi_1) - \mu_1 m_2 r_2' \, sin(\psi_2') &= 0 \\ R_{P3} &= m_1 r_1 cos(\psi_1) - \mu_1 m_2 r_2' \, cos(\psi_2') &= 0 \end{aligned} \tag{102}$$

Because $\psi_2 = 0$, it holds that $\psi_2' = \pi$ as long as $L_2 > r_2$. By looking at the equation for R_{P3} we find that $\psi_1 = \pi$. This finally leads to the following conditions in solution set M4-F-CP1-II:

$$\begin{aligned} \epsilon &= 1 \\ L_1 &= L_3 \\ L_2 &= d \\ \psi_1 &= \pi \\ \psi_2 &= 0 \\ \psi_3 &= \pi \\ r_2 &= L_2 - \frac{m_1 r_1}{\mu_1 r_2} \\ r_3 &= \frac{\mu_2 m_2 r_2}{m_3} \\ k_2 &= \sqrt{\frac{m_2 r_2 (L_2 - r_2) - I_1}{m_2}} \\ k_3 &= \sqrt{\frac{-m_3 r_3 (\mu_2 L_2 + r_3) + I_1}{m_3}} \end{aligned} \tag{103}$$

Which is equal to Case II in [3], except for the sign of ϵ.

Check for solution set M4-F-CP1-III

In this solution set, all link lengths are equal, and thereby $\mu_1 = \mu_2 = \mu_3 = 1$. Additionally, this set imposes no conditions on the inertia of link 3. From reasoning, it can be concluded that this could not be a valid solution set. In a dynamically balanced mechanism, inertias and masses have to be carefully chosen such that all the links compensate for each other's moment of inertia. There could be no possibility for which a mechanism is balanced for each value of k_3 except for a mechanism in which this link does not rotate.

4.5 Moment balance for solution set M4-F-CP2a

In this section, the conditions from Eq. 52 are used to write Δ as an exact square. This results in the following equation for the angular momentum of the mechanism:

$$H_o = (I_1 + I_2)\dot{\theta}_1 \tag{104}$$

This could be set to zero by having the constraint $I_2 = -I_1$. However, just like in case M4-F-CP1-III, this set will have no physical solution.

4.6 Moment balance for solution set M4-F-CP2b

In this section, we will write Δ as an exact square using the conditions from Eq. 53. This will result in the following equation for the total angular momentum of the mechanism:

$$H_0 = [\frac{J_n}{J_d}] \, \dot{\theta}_1 \tag{105}$$

In which

$$J_n = \sum_{s=0}^{1} \sum_{t=0}^{1} j_{s,t} cos^s(\theta_1) sin^t(\theta_1) \tag{106}$$

$$J_d = \epsilon\left[\mu_2^2 - 2\mu_2\, cos(\theta_1) + 1\right] \tag{107}$$

In which

$$\begin{aligned} j_{1,1} &= I_a\mu_2^2(1-\epsilon) \\ j_{1,0} &= -\mu_2[I_2 - I_3 + \epsilon(2I_1 + I_2 + I_3)] \\ j_{0,1} &= I_a\mu_2(\epsilon - 1) \\ j_{0,0} &= \epsilon(I_1 + I_2 + I_3 + \mu_2^2 I_1) + \mu_2^2 I_2 - I_3 \end{aligned} \tag{108}$$

With these equations, a couple of solutions can be found:

M4-F-CP2b-I

$$\begin{aligned} \epsilon &= 1 \\ I_2 &= -I_1 \end{aligned} \tag{109}$$

M4-F-CP2b-I

$$\begin{aligned} \epsilon &= \pm 1 \\ I_a &= 0 \\ I_3 &= -I_1 \\ I_2 &= I_1 \end{aligned} \tag{110}$$

Check for solution set M4-F-CP2b-I

Just like solution set M4-F-CP1-III and M4-F-CP2a, this solution will not have a physical solution because there are no conditions for I_3.

Check for solution set M4-F-CP2b-II

We will start off by looking at the constraint $I_a = 0$. Just like before, this results in the possible solutions

$$\begin{aligned} r_2 &= 0 \\ \psi_2 &= 2n\pi \\ \psi_2 &= (2n+1)\pi \end{aligned} \tag{111}$$

With the static constraints, $r_2 = 0$ would result in conditions $\psi_1 = \pi$ and $r_3 = 0$. When putting this into the constraint $I_3 = -I_1$ we obtain

$$m_3 k_3^2 = -m_1[k_1^2 + r_1^2 + \mu_1 r_1 L_2] \tag{112}$$

Which clearly has no physical solution because the left-hand side will always be positive while the right-hand side will always be negative.

With the other two solutions for ψ_2 we can still obtain the following from R_{P2} and R_{P4}:

$$\begin{aligned} \psi_3 &= \psi_2 + \pi \\ r_3 &= \frac{\mu_2 m_2 r_2}{m_3} \end{aligned} \tag{113}$$

With the condition $I_2 = I_1$ we can write the solution

$$k_2 = \sqrt{\frac{m_2 r_2(L_2 cos(\psi_2) - r_2) + I_1}{m_2}} \tag{114}$$

With the condition $I_3 = -I_1$ we can write the solution

$$k_3 = \sqrt{\frac{m_3 r_3(\mu_2 L_2\, cos(\psi_3) - r_3) - I_1}{m_3}} \tag{115}$$

Filling in these expressions with the second solution from Eq. 111 ($\psi_2 = 0$) we obtain

$$\begin{aligned} k_2 &= \sqrt{\frac{m_2 r_2 (L_2 - r_2) + I_1}{m_2}} \\ k_3 &= \sqrt{\frac{-m_3 r_3 (\mu_2 L_2 + r_3) - I_1}{m_3}} \end{aligned} \tag{116}$$

In order to have a physical value for k_3, I_1 should be negative, which could only be the case if $\psi_1 = 0$. Filling in this finding into R_{P3} leads to

$$r_2 = L_2 + \frac{m_1 r_1}{m_2} \tag{117}$$

Which would result in an inconsistency because I_3 should be negative in the equation for k_3, but positive in the equation for k_2.

From R_{P1} and R_{P3} and the third solution from Eq. 111 ($\psi_2 = \pi$) we find:

$$\begin{aligned} \psi_1 &= \pi \\ r_2 &= \frac{m_1 r_1}{m_2} - L_2 \end{aligned} \tag{118}$$

Which are also consistent with the other equations. This leads to the total solution set for M4-F-CP2b-II:

$$\begin{aligned} \epsilon &= \pm 1 \\ L_2 &= L_1 \\ L_3 &= d \\ \psi_1 &= \pi \\ \psi_2 &= \pi \\ \psi_3 &= 0 \\ r_2 &= \frac{m_1 r_1}{m_2} - L_2 \\ r_3 &= \frac{\mu_2 m_2 r_2}{m_3} \\ k_2 &= \sqrt{\frac{-m_2 r_2 (L_2 + r_2) + I_1}{m_2}} \\ k_3 &= \sqrt{\frac{m_3 r_3 (\mu_2 L_2 - r_3) - I_1}{m_3}} \end{aligned} \tag{119}$$

Which is equal to case III in [3].

5 Dynamic decoupling

A dynamically balanced mechanism does not induce any reaction forces on its base during motion. For a dynamically decoupled mechanism, this also holds, but also the opposite. When forces are applied to the base of a dynamically decoupled mechanism, it does not change its configuration. This property could be used to generate additional degrees of freedom by adding dynamically decoupled mechanism. This is for example done in [3].

5.1 Moment of inertia of a single link

For the inertia tensors of the individual links, it is assumed that the links are symmetric around their length axis, and thereby have zero products of inertia. The inertia tensor of the first link thereby is:

$$\mathbf{I}_{c,1} = \begin{bmatrix} I_{xx,1} & 0 & 0 \\ 0 & I_{yy,1} & 0 \\ 0 & 0 & I_{zz,1} \end{bmatrix} \tag{120}$$

The other inertia tensors have the same form, but with their own inertias around their principal axes.

In order to find conditions for the reactionless property of a mechanism, we have to express the total inertia of all links together around 1 point. In this point, the inertia tensor should not be dependent on the configuration in the mechanism in order for the mechanism to be reactionless. Therefore, we need to express the moment of inertia of each link around the origin (point P_1 in Fig. 1). This could be done using the parallel axis theorem.

5.1.1 Parallel axis theorem

With the parallel axis theorem, the inertia of a body could be calculated around another point than its centre of mass. Firstly, we define a vector $\mathbf{R}_i$, which is a vector from the centre of mass of the link to the point P_1. The moment of inertia of a link around P_1 could then be calculated using:

$$\mathbf{I}_{P_1,i} = \mathbf{I}_{c,i} + m_i[(\mathbf{R}_i \cdot \mathbf{R}_i)\mathbf{E}_3 - \mathbf{R}_i \otimes \mathbf{R}_i] \tag{121}$$

In which $\mathbf{E}_3$ is a 3×3 identity matrix.

All inertia tensors should also be expressed in the same coordinate system before they can be added. On has the choice to either do the parallel axis theorem calculations in the body-fixed frame and afterwards apply a rotation matrix, or to immediately express the vector $\mathbf{R}_i$ in the inertial coordinate frame. It differs per link what the easiest choice is. In the following calculations, a prefix ${}^{\mathcal{B}}$ refers to the body-fixed frame of the respective link, and ${}^{\mathcal{N}}$ to the inertia frame.

Link 1

$${}^{\mathcal{B}}\mathbf{R}_1 = \begin{pmatrix} -r_1 \\ 0 \\ 0 \end{pmatrix} \qquad \mathbf{Q}_1 = \begin{pmatrix} \cos(\psi_1 + \theta_1) & -\sin(\psi_1 + \theta_1) & 0 \\ \sin(\psi_1 + \theta_1) & \cos(\psi_1 + \theta_1) & 0 \\ 0 & 0 & 1 \end{pmatrix} \tag{122}$$

$${}^{\mathcal{N}}\mathbf{I}_{P_1,1} = \mathbf{Q}_1[\mathbf{I}_{c,1} + m_1[(\mathbf{R}_1 \cdot \mathbf{R}_1)\mathbf{E}_1 - \mathbf{R}_1 \otimes \mathbf{R}_1]]\mathbf{Q}_1^T \tag{123}$$

Link 2

$${}^{\mathcal{N}}\mathbf{R}_2 = \begin{pmatrix} -r_2\,\cos(\psi_2 + \theta_2) - L_2\,\mu_1\,\cos(\theta_1) \\ -r_2\,\sin(\psi_2 + \theta_2) - L_2\,\mu_1\,\sin(\theta_1) \\ 0 \end{pmatrix} \qquad \mathbf{Q}_2 = \begin{pmatrix} \cos(\psi_2 + \theta_2) & -\sin(\psi_2 + \theta_2) & 0 \\ \sin(\psi_2 + \theta_2) & \cos(\psi_2 + \theta_2) & 0 \\ 0 & 0 & 1 \end{pmatrix} \tag{124}$$

$${}^{\mathcal{N}}\mathbf{I}_{P_1,2} = \mathbf{Q}_2\mathbf{I}_{c,2}\mathbf{Q}_2^T + m_2[({}^{\mathcal{N}}\mathbf{R}_2 \cdot {}^{\mathcal{N}}\mathbf{R}_2)\mathbf{E}_3 - {}^{\mathcal{N}}\mathbf{R}_2 \otimes {}^{\mathcal{N}}\mathbf{R}_2] \tag{125}$$

Link 3

$$ {}^{\mathcal{N}}\mathbf{R}_3 = \begin{pmatrix} -L_2\,\mu_3 - r_3\,\cos(\psi_3+\theta_3) \\ -r_3\,\sin(\psi_3+\theta_3) \\ 0 \end{pmatrix} \qquad \mathbf{Q}_3 = \begin{pmatrix} \cos(\psi_3+\theta_3) & -\sin(\psi_3+\theta_3) & 0 \\ \sin(\psi_3+\theta_3) & \cos(\psi_3+\theta_3) & 0 \\ 0 & 0 & 1 \end{pmatrix} \tag{126} $$

$$ {}^{\mathcal{N}}\mathbf{I}_{P_1,3} = \mathbf{Q}_3\mathbf{I}_{c,3}\mathbf{Q}_3^T + m_2[({}^{\mathcal{N}}\mathbf{R}_3 \cdot^{\mathcal{N}} \mathbf{R}_3)\mathbf{E}_3 - {}^{\mathcal{N}}\mathbf{R}_3 \otimes^{\mathcal{N}} \mathbf{R}_3] \tag{127} $$

5.2 Moment of inertia of the total mechanism around P_1

With the calculations above, the total inertia of the mechanism around P_1 could be expressed as:

$$ {}^{\mathcal{N}}\mathbf{I}_{tot} = {}^{\mathcal{N}}\mathbf{I}_{P_1,1} + {}^{\mathcal{N}}\mathbf{I}_{P_1,2} + {}^{\mathcal{N}}\mathbf{I}_{P_1,3} \tag{128} $$

This inertia tensor should be independent of the configuration in order to have a dynamically decoupled mechanism.

5.3 Dynamic decoupling conditions

5.3.1 Dynamic decoupling around the Z-axis

We will start by looking at the conditions for the mechanism to be decoupled in-plane. This means that the inertia around the Z-axis should be independent of the configuration, and thereby should not contain values of θ_i.

From Eq. 128 we find:

$$ {}^{\mathcal{N}}I_{zz} = I_c + 2\,L_2\,m_2\,\mu_1\,r_2\,\cos(\psi_2 - \theta_1 + \theta_2) + 2\,L_2\,m_3\,\mu_3\,r_3\,\cos(\psi_3+\theta_3) \tag{129} $$

In which

$$ I_c = m_2\,{L_2}^2\,{\mu_1}^2 + m_3\,{L_2}^2\,{\mu_3}^2 + m_1\,{r_1}^2 + m_2\,{r_2}^2 + m_3\,{r_3}^2 + I_{zz,1} + I_{zz,2} + I_{zz,3} \tag{130} $$

This equation could be rewritten in the form:

$$ {}^{\mathcal{N}}I_{zz} = I_c + A\,cos(\psi_2) + B\,sin(\psi_2) + C\,cos(\psi_3) + D\,sin(\psi_3) \tag{131} $$

In this equation, θ_2 and θ_3 are substituted using the geometric relations. Therefore this equation is only dependent on θ_1. The expressions for A, B, C, D can be found in [7] but are left out in this document due to their complexity.

Due to the existence of both $sin(\theta_1)$ and $\cos(\theta_1)$ in the numerator and denominator of B and D, these terms could not be set to zero. Therefore we obtain that $sin(\psi_2) = 0$ and $sin(\psi_3) = 0$. With the leftover part of the expression, we can rewrite to:

$$ {}^{\mathcal{N}}I_{zz} = I_c + A\,cos(\psi_2) + C\,cos(\psi_3) \tag{132} $$

This leads to an expression in the form:

$$ {}^{\mathcal{N}}I_{zz} = I_c + \frac{B_2\,cos^2(\theta_1) + B_1\,cos(\theta_1) + B_0}{\mu_2\,(\mu_1^2\mu_3^2 - 2\mu_1\mu_3 cos(\theta_1))} \tag{133} $$

We want to rewrite this into the form below in which $A_2 = A_0 = 0$ for a dynamically decoupled mechanism:

$$ {}^{\mathcal{N}}I_{zz} = I_c + (A_2 cos(\theta_1) + A_1) + \frac{A_0}{\mu_1^2 + \mu_3^2 - \mu_1\mu_3 cos(\theta_1)} \tag{134} $$

These could be rewritten into each other using the following expression:

$$ \begin{pmatrix} 1 & \mu_1^2+\mu_3^2 & 0 \\ 0 & -2\mu_1\mu_3 & \mu_1^2+\mu_3^2 \\ 0 & 0 & -2\mu_1\mu_3 \end{pmatrix} \begin{pmatrix} A_0 \\ A_1 \\ A_2 \end{pmatrix} = \mu_2 \begin{pmatrix} B_0 \\ B_1 \\ B_2 \end{pmatrix} \tag{135} $$

Variable A_2 consists of some constant values multiplied with $m_3 r_3 cos(\psi_3) + m_2\mu_2 r_2 cos(\psi_2)$, which is equal to R_P4 from Eq. 45. So, if the mechanism is force balanced, the mechanism will (in combination with the other conditions obtained in this section) have a constant inertia around the z-axis and will therefore be decoupled around the Z-axis.

We will use the following conditions (valid for M4-F-II and M4-F-CP1-II):

$$\psi_2 = 0 \tag{136}$$
$$\psi_3 = \pi \tag{137}$$
$$r_3 = \frac{\mu_2 m_2 r_2}{m_3} \tag{138}$$

5.3.2 Dynamic decoupling around the X-axis

After obtaining the conditions for dynamic decoupling around the Z-axis, we will now look into the dynamic decoupling conditions around the X-axis. The inertia around the X-axis is in the form:

$${}^{\mathcal{N}}I_{xx} = \frac{B_4\, cos^4(\theta_1) + B_3\, cos^3(\theta_1) + B_2\, cos^2(\theta_1) + B_1\, cos(\theta_1) + B_0}{4m_3\mu_2^2\,(\mu_1^2 + \mu_3^2 - 2\mu_1\mu_3 cos(\theta_1))^2} \tag{139}$$

In the same way as we did for the inertia around the Z-axis, we want to rewrite this expression in a simpler form. For this case:

$${}^{\mathcal{N}}I_{xx} = A_4\, cos^2(\theta_1) + A_3\, cos(\theta_1) + A_2 + \frac{A_1}{V - 2U cos(\theta_1)} + \frac{A_0}{(V - 2U cos(\theta_1))^2} \tag{140}$$

In which

$$U = \mu_1\mu_3 \qquad\qquad V = \mu_1^2 + \mu_3^2 \tag{141}$$

The coefficients of both equations are related to each other with the following equation:

$$\begin{pmatrix} 1 & V & V^2 & 0 & 0 \\ 0 & -2\,U & -4\,U\,V & V^2 & 0 \\ 0 & 0 & 4\,U^2 & -4\,U\,V & V^2 \\ 0 & 0 & 0 & 4\,U^2 & -4\,U\,V \\ 0 & 0 & 0 & 0 & 4\,U^2 \end{pmatrix} \begin{pmatrix} A_0 \\ A_1 \\ A_2 \\ A_3 \\ A_4 \end{pmatrix} = 4m_3\mu_2^2 \begin{pmatrix} B_0 \\ B_1 \\ B_2 \\ B_3 \\ B_4 \end{pmatrix} \tag{142}$$

The mechanism is dynamically decoupled around the x-axis if $A_4 = A_3 = A_1 = A_0 = 0$. Solving using *MATLAB* results in:

$$\begin{aligned} I_{xx,1} &= m_2\, {L_2}^2\, {\mu_1}^2 - m_2\, r_2\, L_2\, {\mu_1}^2 + m_1\, {r_1}^2 + I_{yy,1} \\ I_{xx,2} &= m_2 r_2^2 - L_2 m_2 r_2 + I_{yy,2} \\ I_{xx,3} &= I_{yy,3} + \frac{{m_2}^2\, {\mu_2}^2\, {r_2}^2 + L_2\, m_3\, m_2\, {\mu_2}^2\, r_2}{m_3} \end{aligned} \tag{143}$$

With these solutions, the total Inertia tensor from Eq. 128 becomes a principal inertia tensor that is independent of the configuration of the mechanism.

Given these results, it may seem possible for a single planar four-bar linkage to have a constant spatial inertia tensor while in motion. However, from the balancing conditions for M4-F-CP1-II (where $r_2 < L_2$), one can write

$$|I_{xx,2} - I_{yy,2}| - I_{zz,2} = I_{zz,1} + m_1 r_1 (r_1 + L_1) > 0 \tag{144}$$

i.e.,

$$|I_{xx,2} - I_{yy,2}| > I_{zz,2} \tag{145}$$

Clearly, this is impossible since the difference between any two components must be smaller than or equal to the third one for the three principal moments of inertia of a rigid body.

5.3.3 Planar dynamic decoupling

From the material stated in this appendix, it could be concluded that a dynamically balanced mechanism is also dynamically decoupled for planar motion in the x-y plane. However, this is only true for motion within this plane.

6 Conclusion

With the calculations presented in this appendix, the following dynamically balanced mechanisms were found. These are also dynamically decoupled for planar motion in the xy-plane, but not for motion outside of this plane.

6.1 M4-F-II

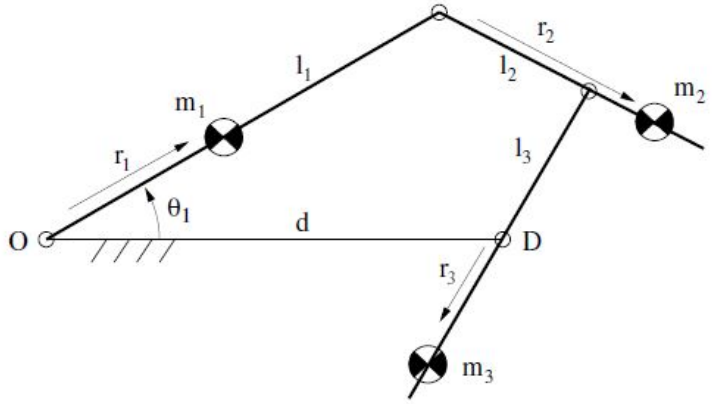

Figure 4: Balanced solution M4-F-II

$$
\begin{aligned}
\epsilon &= \pm 1 \\
L_1 &= d \\
L_2 &= L_3 \\
\psi_1 &= 0 \\
\psi_2 &= 0 \\
\psi_3 &= \pi \\
r_2 &= L_2 + \frac{m_1 r_1}{m_2} \\
r_3 &= \frac{m_2 r_2}{m_3} \\
k_2 &= \sqrt{\frac{-m_2 r_2^2 - I_1}{m_2}} \\
k_3 &= \sqrt{\frac{-m_2^2 r_2^2 - m_3 I_1}{m_3^2}}
\end{aligned}
\tag{146}
$$

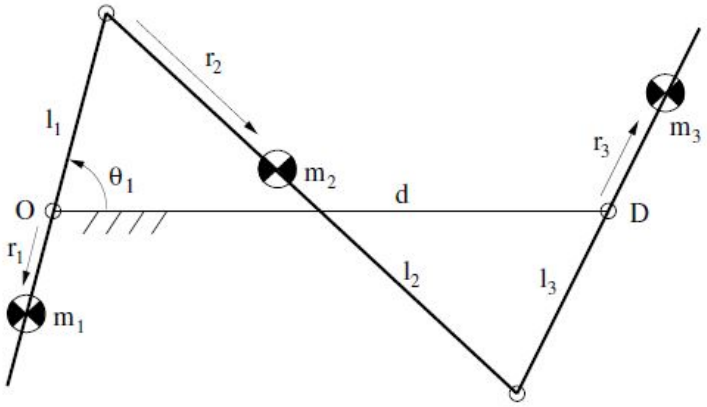

Figure 5: Balanced solution M4-F-CP1-II

6.2 M4-F-CP1-II

$$
\begin{aligned}
\epsilon &= 1 \\
L_1 &= L_3 \\
L_2 &= d \\
\psi_1 &= \pi \\
\psi_2 &= 0 \\
\psi_3 &= \pi \\
r_2 &= L_2 - \frac{m_1 r_1}{\mu_1 r_2} \\
r_3 &= \frac{\mu_2 m_2 r_2}{m_3} \\
k_2 &= \sqrt{\frac{m_2 r_2 (L_2 - r_2) - I_1}{m_2}} \\
k_3 &= \sqrt{\frac{-m_3 r_3 (\mu_2 L_2 + r_3) + I_1}{m_3}}
\end{aligned}
\tag{147}
$$

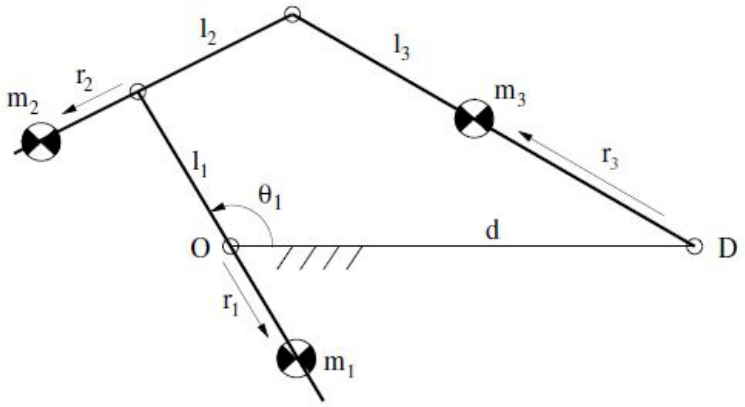

Figure 6: Balanced solution M4-F-CP2b-II [3]

6.3 M4-F-CP2b-II

$$
\begin{aligned}
\epsilon &= \pm 1 \\
L_2 &= L_1 \\
L_3 &= d \\
\psi_1 &= \pi \\
\psi_2 &= \pi \\
\psi_3 &= 0 \\
r_2 &= \frac{m_1 r_1}{m_2} - L_2 \\
r_3 &= \frac{\mu_2 m_2 r_2}{m_3} \\
k_2 &= \sqrt{\frac{-m_2 r_2 (L_2 + r_2) + I_1}{m_2}} \\
k_3 &= \sqrt{\frac{m_3 r_3 (\mu_2 L_2 - r_3) - I_1}{m_3}}
\end{aligned}
\tag{148}
$$

7 Towards spatially balanced mechanisms

With the knowledge described in this document, it is possible to build multi-DoF mechanisms that only exhibit planar movements.

In [3], the author found that although no physically possible conditions exist that make ${}^{\mathcal{N}}I_{xx}$ and ${}^{\mathcal{N}}I_{yy}$ independent of the configuration, the sum of these inertias could be independent of the configuration. So, if two four-bar mechanisms are added orthogonally, a dynamically decoupled mechanism for spatial motion could be obtained. An example of the M4-F-CP1-II four-bar can be seen in Fig. 7.

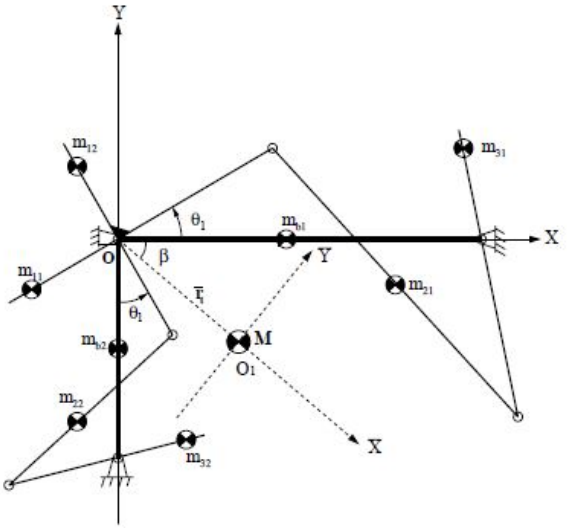

Figure 7: Spatially dynamically decoupled mechanism that consist of two four-bar mechanisms [3]

When using the structure from Fig. 7 as a building block, spatially dynamically balanced mechanisms could be synthesized. In the example from Fig. 8 two M4-F-CP1-II four-bar mechanisms are stacked after each other to obtain a 2 DoF planar mechanism. At the end of this planar mechanism, a spatially decoupled mechanism is added (Fig. 7) to obtain a leg with 3 DoF. Finally, three such legs are added to a platform to obtain a 6 DoF spatially dynamically balanced mechanism.

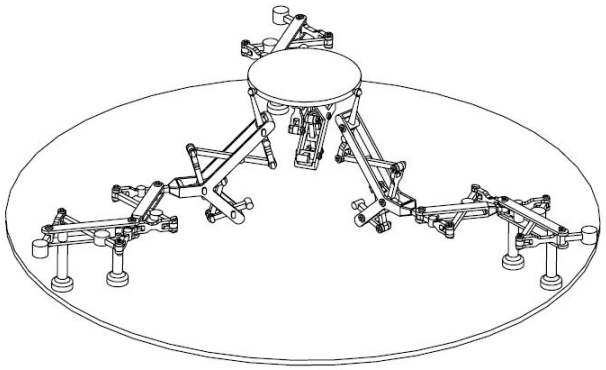

Figure 8: 6 DoF dynamically balanced mechanism

References

[1] R. S. Berkof and G. G. Lowen, "A new method for complete force balancing simple linkages," *journal of Engineering for Industry*, vol. 91, no. 1, pp. 21–26, Feb. 1969.

[2] ——, "Theory of Shaking Moment Optimization of Force-Balanced Four-Bar Linkages," *Journal of Engineering for Industry*, vol. 93, no. 1, pp. 53–60, Feb. 1971.

[3] Y. Wu, "SYNTHESIS AND ANALYSIS OF REACTIONLESS SPATIAL PARALLEL MECHANISMS," PhD, Université Laval, Québec, 2003.

[4] R. Ricard and C. M. Gosselin, "On the Development of Reactionless Parallel Manipulators," in *Volume 7A: 26th Biennial Mechanisms and Robotics Conference*. Baltimore, Maryland, USA: American Society of Mechanical Engineers, Sep. 2000, pp. 493–502.

[5] F. Freudenstein, "Approximate Synthesis of Four-Bar Linkages," *Reson*, vol. 15, pp. 740–767, 2010.

[6] M. Jean and C. Gosselin, "Static balancing of planar parallel manipulators," in *Proceedings of IEEE International Conference on Robotics and Automation*, vol. 4, Apr. 1996, pp. 3732–3737 vol.4, iSSN: 1050-4729.

[7] Y. Wu and C. M. Gosselin, "Synthesis of Reactionless Spatial 3-DoF and 6-DoF Mechanisms without Separate Counter-Rotations," *The International Journal of Robotics Research*, vol. 23, no. 6, pp. 625–642, Jun. 2004.